UNIVERSITÀ DEGLI STUDI DI TRIESTE

XXXII CICLO DEL DOTTORATO DI RICERCA IN

Scienze della terra e meccanica dei fluidi

TITOLO DELLA TESI

Crust-Uppermost Mantle Shear-wave Velocity Structure and Buoyancy Flow Model beneath the Tyrrhenian Basin and Surrounding Margins.

Settore scientifico-disciplinare:

GEO/10 GEOFISICA DELLA TERRA SOLIDA

DOTTORANDO: **Daniel Manu-Marfo**

COORDINATORE: **Prof. Pierpaolo Omari**

SUPERVISORE DI TESI **Prof. Abdelkrim Aoudia**

ANNO ACCADEMICO 2018/2019

Crust-Uppermost Mantle Shear-wave Velocity Structure and Buoyancy Flow Model beneath the Tyrrhenian Basin and Surrounding Margins

Manu-Marfo Daniel

University of Trieste

A thesis submitted for the degree of

Doctor of Philosophy

March 2020

Abstract

The Tyrrhenian basin serves as a natural laboratory for back-arc basin studies in the Mediterranean region. Yet, little is known about the crust-uppermost mantle structure beneath the basin and surrounding margins. Here, we present a new 3D shear-wave velocity model and Moho topography map for the Tyrrhenian basin and its margins using ambient noise cross-correlations. We apply a self-parameterized Bayesian inversion of Rayleigh-wave group and phase velocity dispersions to estimate the lateral variation of shear velocity and its uncertainty as a function of depth down to 100 km. We also derived a contemporary 3D density model of the lithosphere beneath the Tyrrhenian region by combining seismic velocity, surface heat flow, gravity and topography. Further, we investigated the contribution of buoyancy forces to the regional dynamics by modelling the lithospheric flow field below the Tyrrhenian basin and margins using as input the 3D lithospheric density structure beneath the study area. In general, our models support present-day geodynamics with a predominant Africa-Eurasia convergence and can explain the heat flux, regional geology and magmatism in the Tyrrhenian basin and surrounding margins.

Keywords: Tyrrhenian basin, ambient noise tomography, Bayesian inversion, shear-wave velocity structure, lithospheric density structure, buoyancy flow model

Table of Contents

1 Introduction

It is generally acknowledged that the Mediterranean geodynamics has been shaped by the collision of two large, slowly moving plates (African and Eurasian plates), and perhaps, also by smaller intervening microplates (Adria, Aegea, and Anatolia) (Dewey et al., 1989; Faccenna et al., 2014; Jolivet & Faccenna, 2000; McKenzie, 1970). Before the Mesozoic, the Mediterranean was predominantly affected by rifting. During the Mesozoic, the oceanic Tethys areas and passive continental margins developed, leading to the formation of widespread carbonate platforms. In the late Mesozoic, subduction zones (from west to east, the Alps-Betics, Dinarides, and the Hellenides) dominated the Mediterranean region, inverting the extensional regime and leading to the consumption of the previously formed Tethyan oceanic lithosphere and the adjacent continental margins (Carminati & Doglioni, 2005). The main Cenozoic subduction zones in the Mediterranean are the Alps–Betics, the Apennines–Maghrebides, and the Dinarides–Hellenides–Taurides (Figure 1.1). Presently, the only remaining Mesozoic oceanic lithosphere is found in the Ionian abyssal plain and is being subducted northwestward beneath the Calabrian Arc and northeastward below the Hellenic Arc (Jolivet & Faccenna, 2000; Speranza et al., 2012).

In spite of compression dominating the Mediterranean tectonics, several areas exhibit extensional tectonic regime. Extensional basins in the Mediterranean formed during the Cenozoic are from west to east, the Alboran Sea, the Valencia basin, the Liguro-Provençal basin, the Tyrrhenian basin, the Aegean basin, and the Pannonian basin (Figure 1.1). Paleotectonic reconstructions show that extension in the Mediterranean is the result of back-arc extension and/or collapse of the inner part of the thickened Alpine crust (Dercourt et al., 1986; Dewey, 1988; Dewey et al., 1989; Jolivet & Faccenna, 2000).

The Meso-Cenozoic geodynamic evolution of the Central Mediterranean especially, has undoubtedly been controlled by the paleogeographic inheritance of the African and European plates which have led to the present-day continental collision that is particularly evident in the Alps (Channell et al., 1979; Dercourt et al., 1986; Dewey et al., 1989; Handy et al., 2010; Malinverno & Ryan, 1986; Schettino & Turco, 2011). The overall plate tectonic evolution of the Central Mediterranean in the Tertiary was driven by the Adriatic promontory, a large piece of continental crust of African affinity (Channell et al., 1979), which colliding with the Eurasian plate formed the orogenic belts that now surround the Adriatic Sea. The most relevant tectonic regime from Neogene to Recent has been the evolution of the Calabrian Arc, a narrow and arcuate subduction-rollback system related to the convergence of the African and European plates and the southeastward retreat of the Tethyan slab (Faccenna et al., 2001; Jolivet & Faccenna, 2000; Malinverno & Ryan, 1986; Rehault et al., 1985). Seismic tomography in the Calabrian Arc shows a down-going continuous slab that penetrate into the mantle (Faccenna et al., 2007; Neri et al., 2009; Scarfì et al., 2018; Wortel & Spakman, 2000) and a 70°-dipping Wadati-Benioff zone marked by earthquakes down to nearly 500 km depth (Selvaggi & Chiarabba, 1995; Wortel & Spakman, 2000).

The Central Mediterranean region offers a unique opportunity to study the problem of the development of extensional basins in a complex collisional environment. This is evident in the number of studies that focuses on the evolution of the Tyrrhenian Sea, a back-arc basin that lies at the back of the westward directed Apennine-Maghrebian compression front, and its overall contribution to the present-day Mediterranean geodynamics.

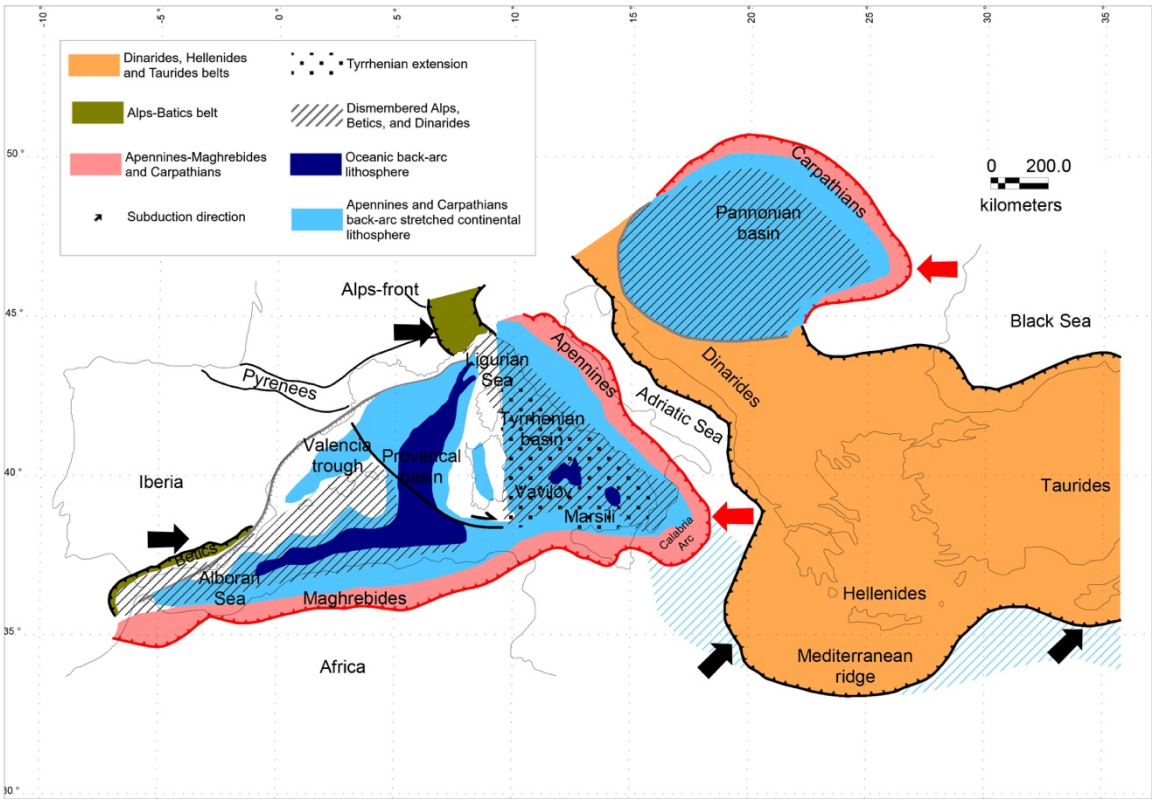

Figure 1.1 Present-day geodynamic framework of the Mediterranean (modified after Carminati & Doglioni, 2005). The red subduction zones corresponds to westwards directed subductions and black, eastward directed. The Apennines-Maghrebides subduction system is related to back-arc basins of the Central-Western Mediterranean region. Closely related to the Mediterranean geodynamics are the Carpathian subduction and the Pyrenees.

The Tyrrhenian basin developed during the Tortonian to Quaternary, its formation commenced after Sardinia-Corsica block rotated counter-clockwise about 25°–30° away from the European plate leading to the rifting of the Liguro-Provençal basin from about ~ 30 to 15 Ma (Channell et al., 1979; Gailler et al., 2009; Gattacceca et al., 2007; Jolivet et al., 1994; Rehault et al., 1985). The Tyrrhenian basin itself then opened from ~ 15 Ma to present, with different styles of rifting occurring at different stages of the evolution (Faccenna et al., 2007). In the early stage (~ 10 to 5 Ma), extension in the Tyrrhenian basin was driven by the eastward migration of the Adriatic subduction system, causing a roughly east-west rifting and the opening of the northern Tyrrhenian basin (Faccenna et al., 2001). Here, extension after commencement progressively migrated eastward with time and was accompanied by the emplacement of magmatic bodies

(Bartole, 1995; Jolivet et al., 1994). Later, the rollback of the subducting Ionian lithosphere triggered the opening of the southern Tyrrhenian basin, approximately from 7 to 5 Ma (Faccenna et al., 2001, 2007; Malinverno & Ryan, 1986; Marani & Trua, 2002; Pondrelli, 2004).

Stronger extension in the southern Tyrrhenian basin (up to ~5 cm/yr (Peccerillo, 2017b)) resulted in the opening of the Vavilov basin (formed 4-3 Ma) and Marsili basins (formed 2-1 Ma) (Cocchi et al., 2009; Dewey et al., 1989; Faccenna et al., 2001, 2007; Kim Kastens et al., 1988; Malinverno & Ryan, 1986; Sartori, 2003). Conventionally, the 41° parallel line is an important tectonic structure that separates the north and the south Tyrrhenian basins (Boccaletti et al., 1990; Peccerillo, 2017b).

Volcanism in the Tyrrhenian area shows remarkably large variations in time and space owing to the complex geodynamic history of the region. The petrological and geochemical signatures of magmas show arc-type (orogenic), intraplate (anorogenic) and mid-ocean-ridge compositional features. The affinity of the orogenic magmas range from calc-alkaline, shoshonitic and ultrapotassic, and are spread over the entire Tyrrhenian region becoming younger eastward from Sardinia to the Italian peninsula and the southeastern Tyrrhenian Sea. Anorogenic magmas include tholeiites to Na-alkaline compositions and occur in Sardinia, in the Tyrrhenian basin and Sicily. The variable magmatism in the Tyrrhenian region point to large differences in mantle source compositions and degrees of melting (Lustrino et al., 2011; Peccerillo, 2017b; Savelli, 2002).

Although the Tyrrhenian basin is an extensively studied area, much of the crust and uppermost mantle structure is still poorly resolved. The geodynamics of the Central Mediterranean region, in particular, the evolution of the Adriatic-Ionian subduction system has contributed to shaping the structure of the lithosphere beneath the Tyrrhenian area, being that the Tyrrhenian lies at

the foot of this complex plate boundary. This makes knowledge of the structure of the lithosphere, for example, the seismic velocity structure, paramountly important for the understanding of the geodynamics and associated magmatism in the Tyrrhenian area, as it provides constraints to the geodynamic models (e.g., Lucente et al., 1999) and corroborates other geophysical and geological studies.

Traditionally, the structure of the lithosphere is studied applying the inversion of converted phases of teleseismic body waves and/or surface wave dispersions (Bodin et al., 2012; Burdick & Langston, 1977; Langston, 1979; Piana Agostinetti & Amato, 2009) and tomographic inversion of body-wave travel-time residuals (Di Stefano et al., 1999, 2009; Lippitsch, 2003). Each of these seismic imaging techniques has its limitations, which commonly include earthquake location errors, dependence on an irregular distribution of earthquake sources, ad hoc model parameterization and a lack of near-surface resolution. Nevertheless, seismic imaging of the crust and uppermost mantle structure beneath the Tyrrhenian basin using these traditional seismic imaging techniques is further challenging due to the lack of seismic stations on the basin.

In this regard, this thesis aims to first, provide a high-resolution shear-wave velocity structure of the crust and uppermost mantle beneath the Tyrrhenian region from ambient noise tomography. The benefits of using ambient noise tomography technique compared to traditional earthquake based surface wave studies are that; we can take full advantage of the dense distribution of seismic stations around the basin, allowing for dense path coverage across the basin. Again, the short interstation distances mean that we can retrieve short periods data sensitive to the shallow part of the lithosphere compared to teleseismic studies, where such short periods are attenuated due to large source to station distance.

Next, we combine the shear-wave velocity model, surface heat flow, gravity, and topographic data to develop a 3D density model of the crust and uppermost mantle beneath the Tyrrhenian basin and its surroundings. In turn, we discuss the rheological variations suggested by this density structure and explore their implications for the geodynamic evolution of the Tyrrhenian basin and associated magmatism.

Finally, we investigate the dynamics of the active deformation in the Tyrrhenian area. Here, we investigate the contribution of buoyancy forces concerning the ongoing complex lithospheric deformations in the Tyrrhenian area, as revealed by the recent seismicity and geodetic observations (e.g., Chiarabba et al., 2015; D'Agostino et al., 2008).

Thus, this manuscript contains a comprehensive summary of three projects dedicated to the understanding of the geodynamic evolution and current state of the Tyrrhenian lithosphere. It consists of five chapters. The second chapter focuses on ambient noise Rayleigh wave tomography and shear-wave velocity structure of the crust and uppermost mantle beneath the Tyrrhenian basin and margins. In the third chapter, we estimate the 3D density distribution below the Tyrrhenian basin and surroundings. The fourth chapter focuses on modelling the contemporary lithospheric flow field in the Tyrrhenian region. In the final chapter, we summarise our results about the lithosphere structure beneath the Tyrrhenian basin and surrounding margins.

2 Three-dimensional shear-wave velocity structure of the crust and uppermost mantle beneath the Tyrrhenian basin and margins

The Tyrrhenian basin serves as a natural laboratory for back-arc basin studies in the Mediterranean region. Yet, little is known about the crust-uppermost mantle structure beneath the basin and its margins. Here, we present a new 3D shear-wave velocity model and Moho topography map for the Tyrrhenian basin and adjacent margins using ambient noise cross-correlations. We apply a self-parameterized Bayesian inversion of Rayleigh group and phase velocity dispersions to estimate the lateral variation of shear velocity and its uncertainty as a function of depth down to 100 km. At crustal depths, our results support an exhumed mantle basement rather than an oceanic basement below the Vavilov basin. Our velocity model also reveals the presence of a broad low-velocity zone between 40 and 80 km depth affecting much of the Tyrrhenian basin's uppermost mantle structure and its extension mimics the paleogeographic reconstruction of the Calabrian arc in time. We interpret the low-velocity structure as the possible source of Mid-Ocean Ridge Basalts- and Ocean Island Basalts- type magmatic rocks found in the southern Tyrrhenian basin. The 3D crust-uppermost mantle structure supports present-day geodynamics with a predominant Africa-Eurasia convergence.

2.1 Introduction

The Tyrrhenian basin is a back-arc basin in the Mediterranean region which opened in relation to the retreating Adriatic-Ionian slab in the geodynamic context of the African and Eurasian plates convergence (Channell et al., 1979; Faccenna et al., 2001; Malinverno & Ryan, 1986). Being the youngest basin in the Mediterranean region, the Tyrrhenian is considered a perfect natural laboratory for investigating the geodynamics of back-arc basins (Conti et al., 2017; Milia et al., 2017; Moeller et al., 2013; Prada et al., 2015; Trua et al., 2018). However, the crust and upper mantle velocity structure is poorly understood beneath the basin and adjacent margins. The distribution of seismic stations on land makes it seismically challenging to image the shallow lithosphere below the Tyrrhenian basin, as it inhibits proper illumination of the

shallow structures by teleseismic compressional (P) and shear (S) waves (Piromallo & Morelli, 2003). Additionally, teleseismic surface waves mostly lack short period data sensitive to the crust and uppermost mantle structure beneath the basin. Consequently, previous tomographic studies have limited resolution of the shallow lithospheric structure beneath the basin (e.g., Giacomuzzi et al., 2012; Greve et al., 2014; Panza et al., 2007).

An alternative method to study the lithosphere, particularly the crust, is active seismological observations. Most of our knowledge about the crust beneath the Tyrrhenian basin stems from such studies. For instance, Moeller et al., (2013) have shown that the north Tyrrhenian basin is underlain by a continental crust of about 17 km thick but Vp values of the lower crust are higher than those found for the average continental crust. Again, Prada et al., (2014) have found evidence for exhumed mantle rocks beneath the Vavilov basin, contrary to the previous suggestion of an oceanic crust (Duschenes et al., 1986; K. Kastens & Mascle, 1990). However, the problem with active seismological studies is that it provides very little information about the lithospheric structure beneath the Moho and also yields relatively limited information on the lateral variation of the velocity structure.

In over a decade now, ambient noise tomography has proven to be a valuable tool for imaging crust and lithospheric mantle velocity structure (Shapiro et al., 2005; Yang & Ritzwoller, 2008). The method has become particularly essential in areas where there exist difficulties in achieving high-resolution images of the lithosphere using data from 'traditional' seismic imaging techniques (e.g., Guidarelli & Aoudia, 2016; Zulfakriza et al., 2014). This method has already been applied in the Tyrrhenian area (H. Li et al., 2010; Stehly et al., 2009; Verbeke et al., 2012; Yang et al., 2007), but in the framework of regional studies covering the whole Europe (Stehly et al., 2009; Verbeke et al., 2012; Yang et al., 2007) or the Italian peninsula (H.

Li et al., 2010) and therefore does not provide much detailed structure beneath the Tyrrhenian basin.

In this study, we extract interstation Empirical Green's functions (EGFs) from the cross-correlation of ambient noise data using a dense network of 73 broadband stations surrounding the Tyrrhenian basin (Figure 2.1). This allows for the retrieval of high-quality Rayleigh wave group and phase dispersions, which are inverted to obtain group and phase tomography maps, respectively. Local dispersion curves are then extracted from the tomographic maps. These dispersion curves are traditionally inverted for S-wave velocity applying linearized inversion, which iteratively minimizes the objective function until certain misfit value is achieved (Herrmann, 2013). However, such inversion can often lead to a misleading solution if the starting model is not close to the true one and can encounter challenges on the estimation of proper uncertainties, particularly for highly non-linear problems. Here, we implement a highly efficient trans-dimensional Bayesian approach (Dettmer & Dosso, 2012; Pachhai et al., 2015) and provide a new 3D shear wave velocity structure along with the related uncertainties beneath the Tyrrhenian basin and its margins down to 100 km depth. In this approach, layer properties including the number of layers remain unknown in the inversion and fully constrained by data.

To provide efficient sampling and achieve faster convergence, we adapt an interacting Markov chain Monte Carlo Sampling approach in which parameters are allowed to exchange between different chains. Our result highlights new structural features in the Tyrrhenian basin and at the transition with the surrounding Apennines, Calabrian arc, and Sardinia block. We discuss our results in light of the published recent findings in terms of structure, magmatism, and geodynamics.

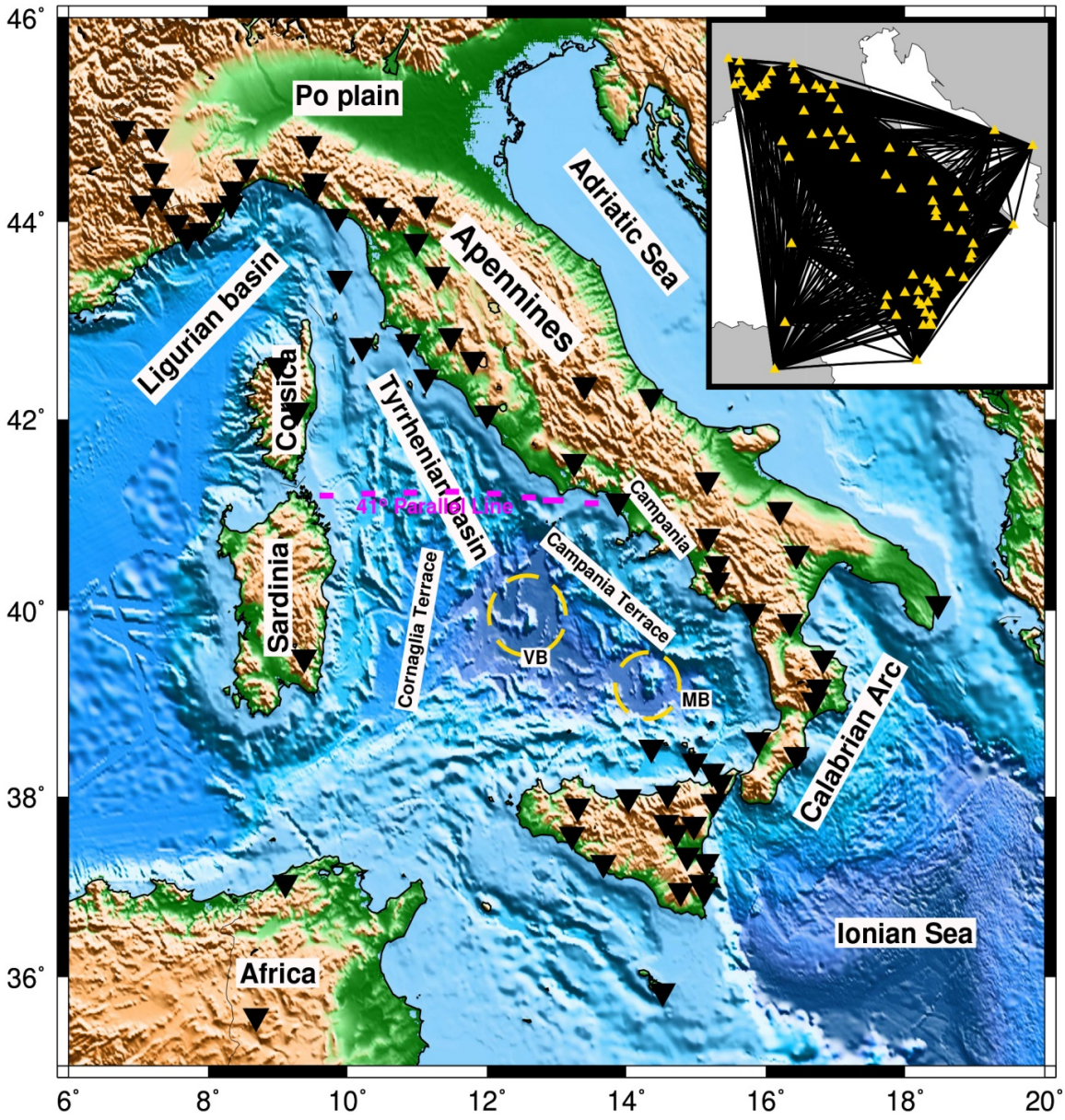

Figure 2.1 Bathymetry and topography map of the Tyrrhenian basin and surroundings. Black triangles represent the location of broadband stations used in this study. VB = Vavilov basin; MB = Marsili basin. Inset map shows the ray density with all inter-station paths used in this study.

2.2 Data and Methods

In recent years, high quality, continuous broadband recordings from Italy, France, Tunisia, Croatia, and Malta seismic networks managed by the Observatories and Research Facilities for European Seismology network (ORFEUS) have become available (Figure 2.1). These networks provide unprecedented dense station coverage to make the ambient noise method a

robust technique for investigating the Tyrrhenian basin seismic velocity structure. Here, we analysed four years continuous broadband vertical-component seismic data recorded by 73 stations from the period of January 2010 to December 2013. Using only the vertical component of the recorded noise data implies that the final waveform we obtain after cross-correlations are mainly dominated by Rayleigh wave signals.

2.2.1 Data processing

Ambient noise data processing involves the cross-correlation of long time series of ambient seismic noise to extract Empirical Green's functions between two seismic stations. Previous studies have shown that the cross-correlation of ambient noise time series recorded at two seismic stations mainly results in the emergence of surface waves signal that propagates between the two stations (Bensen et al., 2007, 2008; Shapiro et al., 2005; Shapiro & Campillo, 2004). Hence, the dispersion characteristics of the estimated surface waves Green's functions provide information about the interstation wave propagation and hence about seismic velocities in the crust and uppermost mantle.

The technique applied in this study to obtain the interstation Empirical Green's Functions from the ambient seismic noise recordings follows the processing method described by Bensen et al., (2007). In the first step, the continuous time-series data recorded at individual broadband stations are cut into day-length signals. The daily waveforms at the individual stations are then demeaned, detrended, corrected for the instrumental response, bandpass filtered between periods of 5 and 150 s, and then decimated to 1 sample per second. To minimize the effect of earthquake-generated signals and other instrumental irregularities on the cross-correlations, we apply a running absolute mean temporal normalization (Bensen et al., 2007). Finally, spectral whitening is applied to reduce the effect of low-frequency microseisms and broaden the available frequency band.

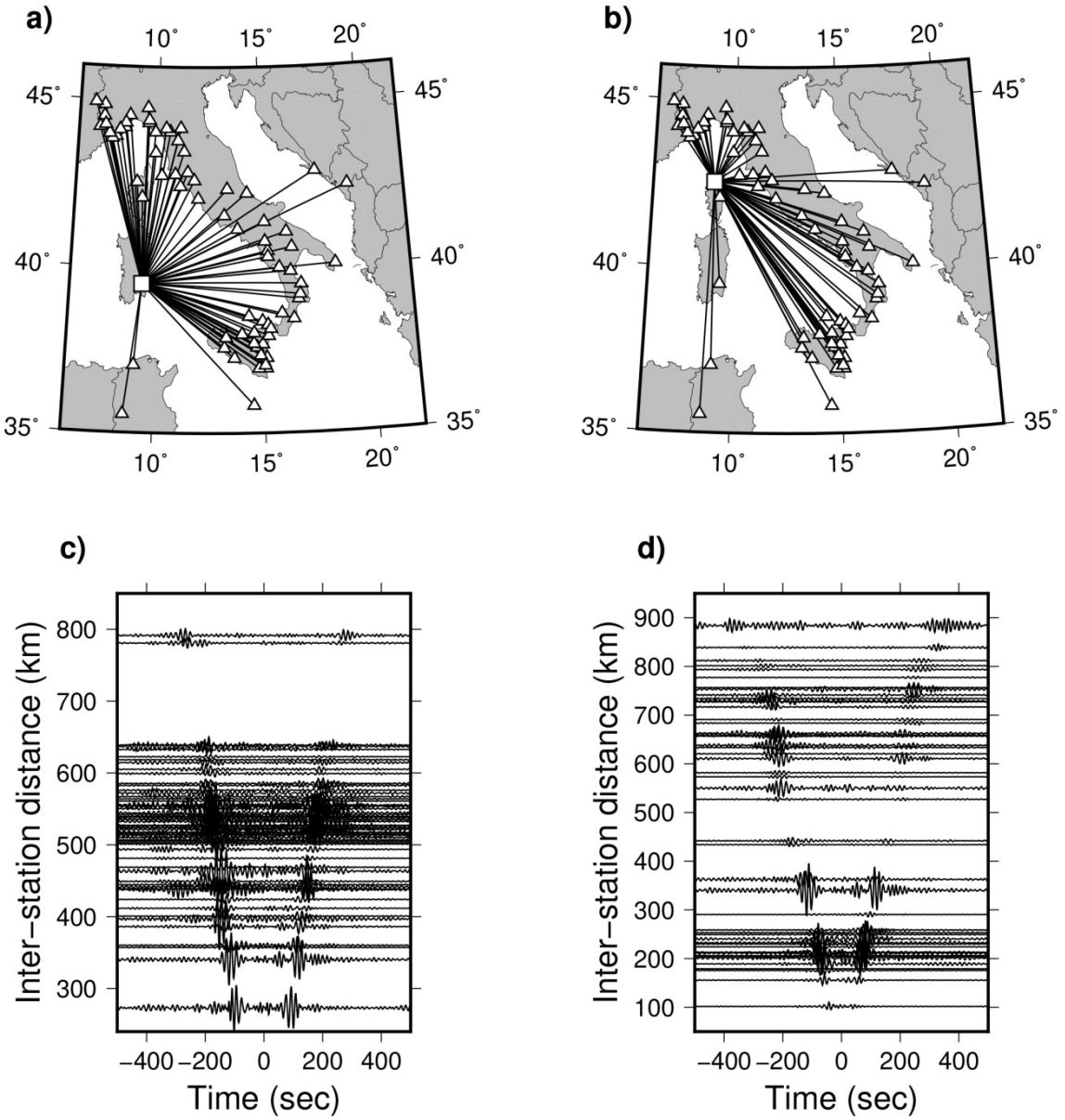

Figure 2.2 Examples of Empirical Greens Functions. Inter-station ray-path between (a) centre station VSL and all other stations, (b) centre station PGT2 and the rest of the stations. (c-d) Examples of record section of cross-correlation calculated for the ray-paths in a and b, respectively. The cross-correlation functions have been bandpass filtered between 5 – 15 s.

The daily waveforms are cross-correlated for all available station pairs and then stacked to form the EGFs (e.g., Figure 2.2). The quality of the Rayleigh wave signal that emerges after cross-correlation and stacking is evaluated based on their signal-to-noise ratio (SNR). The SNR is computed as the ratio of the peak amplitude in the signal time window to the root-mean-square of noise in the time window trailing the signal window. Here, the SNR value serves as

a proxy for uncertainties estimation (Bensen et al., 2007; Yang et al., 2008) and a criterion for the assessment of acceptable Green's functions (Yang & Ritzwoller, 2008). Only cross-correlations with SNR value greater than 7 and having interstation distance of at least 100 km are considered for further analysis. The choice of rejecting cross-correlations with SNR < 7 is a compromise between optimizing measurement quality and quantity. Again, we rejected cross-correlations with interstation distance < 100 km since we are interested in regional distances.

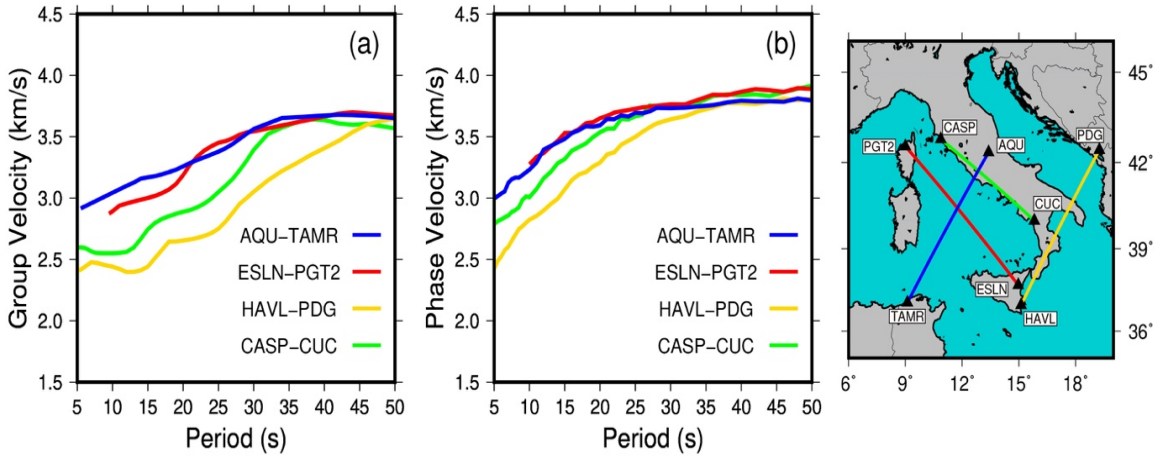

Figure 2.3 Examples of estimated dispersion curves across the study area. (a) group and (b) phase velocity dispersions for selected paths of station pairs indicated by respective colour lines on the map on the right panel.

We analyse the EGFs using the multiple filter technique (Herrmann, 2013) to measure Rayleigh wave fundamental mode group and phase velocity dispersions from 5 to 50 s period.

If we let the dispersed surface wave be represented by the equation

$$f(t,r) = \frac{1}{2\pi}\int_{-\infty}^{\infty} F(\omega,r)\exp(i\omega t)\, d\omega \qquad (2.1)$$

where $F(\omega,r) = A(\omega,r)\exp(-ikr + \phi$ and ϕ is the source phase and k is the wavenumber related to the phase velocity by $\omega=kc$. Then when a narrow bandpass Gaussian filter is applied about a centre frequency ω_0 by the filter $H(\omega - \omega_0)$, the filtered signal is given by

$$g(t,r) = \frac{1}{2\pi} A(\omega_0)\omega_0 \sqrt{\frac{\pi}{\alpha}} \exp[i(\omega_0 t - k_0 r + \phi)] \exp\left[-\frac{\omega_0^2}{4\alpha}\left(t - \frac{r}{U_0}\right)^2\right] \quad (2.2)$$

The last term defines the envelope, which is a maximum at a time corresponding to a group velocity arrival. The group velocity, *U*, is defined as $U = d\omega/dk$. This expression indicates that the narrow band-pass filtered signal can be used to estimate the group velocity by using the time of envelope maximum and the spectral amplitude A at $\omega = \omega_0$, through the envelope amplitude, e.g.,

$$A = (2\pi/\omega_0)\sqrt{(\alpha/\pi)}\,|g(r/U_0, r)\,| \quad (2.3)$$

The phase term can be used to estimate the phase velocity if the source term is known. The phase at the group velocity arrival, e.g., $t = r/U_0$, is

$$\Phi = \tan^{-1}\left[\frac{Im\ g(r/U_0, r)}{Re\ g(r/U_0, r)}\right] = r\omega_0/U - r\omega_0/c + \phi + N2\pi \quad (2.4)$$

where the $N2\pi$ term arises because of the periodicity of the $\tan^{-1}$ function. The source phase term can be eliminated if a two-station technique is used like in ambient noise cross-correlations.

Figure 2.3 shows an example of group and phase velocity curves, traversing along different paths in the study area. The paths through the Tyrrhenian basin (AQU-TAMR and ESLN-PGT2) show higher group and phase velocities at shorter periods compared to the paths along Calabria and Adria (HAVL-PDG) and the Tyrrhenian coast of Italy (CASP-CUC). Generally, high group and/or phase velocity at shorter periods indicates the occurrence of a high-velocity structure at shallow depth. At intermediate periods (~ > 30 s), Figure 2.3b shows that the phase velocities become nearly flat and comparable irrespective of the path, suggesting that waves maybe sampling a relatively uniform uppermost mantle structure.

2.2.2 Rayleigh wave tomography inversion

The estimation of the shear-wave velocity structure from the ambient noise data involves a two-step inversion scheme. In the first step, we invert the Rayleigh wave group and phase dispersion for their respective group and phase tomography maps at different periods (sensitive for different depths). The Rayleigh wave tomography maps are then inverted to retrieve the 3D S-wave velocity structure in the second step.

In this study, we apply the surface wave tomographic method of Yanovskaya & Ditmar, (1990) to obtain the group and phase velocity maps from the Rayleigh wave dispersions extracted from the ambient noise cross-correlation. We estimate the 2D tomography maps at different periods from 5 to 50 s on a 0.5° × 0.5° grid across the study area. This tomographic method is a 2D generalization of the classical 1D method developed by Backus & Gilbert, (1968) and is based on the geometric ray approximation which assumes that the travel time of a surface wave is only sensitive to the media along the great circle path of surface wave propagation.

One of the main advantages of this approach is that it does not require any apriori parameterization of the basis functions. This is because it considers the smoothness of the velocity function based on a regularization parameter such that the output velocities are within the range defined by the observed dispersion curves. It further assumes that the final travel times residuals are distributed randomly (Yanovskaya et al., 1998).

2.2.3 Shear wave velocity inversion

To compute the 3D S-wave velocity model, we extract local group and phase dispersion curves at each node of 0.5° × 0.5° grids from the tomography maps. The local dispersion curves are then jointly inverted for the 1D shear velocity-depth profile at each node.

The estimation of S-wave velocity from the local dispersion data is a non-linear geophysical inverse problem. Traditionally, the inversion is linearized and is solved for velocity with a fixed number of layers. Additionally, a damping parameter is used to stabilize the inversion (Herrmann, 2013). Therefore, proper quantification of uncertainties becomes challenging. Here, we apply a fully non-linear Bayesian approach (Dettmer & Dosso, 2012; Pachhai et al., 2014, 2015), which does not require any damping, to compute the 1D shear velocity profiles and their uncertainties. The parameter uncertainties can either come from measurement errors (i.e. errors in seismic recordings) or theoretical errors (i.e. errors resulting from approximation in model including seismic wave propagation, model parameterization simplifications, assumptions in the data processing etc.).

In Bayesian inversion, the answer to the inverse problem is expressed in terms of posterior probability density (PPD), which combines the prior information (what we know beforehand about the model and is independent of data) and the likelihood (incorporates the data information), i.e., $p(\boldsymbol{m}|\boldsymbol{d}) \propto p(\boldsymbol{d}|\boldsymbol{m})p(\boldsymbol{m})$. Here, $p(\boldsymbol{m}|\boldsymbol{d})$ is the probability of the model parameter vector ($\boldsymbol{m}$) given the data vector ($\boldsymbol{d}$) (i.e. posterior probability density), $p(\boldsymbol{d}|\boldsymbol{m})$ is the probability of the data given the model (i.e., likelihood) and $p(\boldsymbol{m})$ is the prior probability of the model parameters (i.e., number of layers, layer thickness and S velocity). The data errors are typically not known and are approximated as a difference between the measured and predicted data. Note that the P-wave velocity is derived from the fixed Vp/Vs ratio and density is derived from S-wave velocity. In this paper, we consider a uniform prior within a range of reasonable S-wave velocity (based on the past studies e.g., Greve et al., 2014) as a function of depth while the likelihood function is derived based on a Gaussian distribution of data errors.

It is challenging to compute the posterior analytically, particularly for non-linear inversion. Additionally, the model complexity (i.e., the number of layers in the case of observed data) is

not known in advance and estimated parameter uncertainties can highly depend on the model complexity. For example, if we increase the model complexity (i.e., increase the number of layers), the fit between the model prediction and observed data can be improved, but not necessarily required by data and can result in unrealistically large uncertainties. In contrast, a simple model can fit only part of the data resulting in unreasonably small uncertainties. Therefore, a parameter sampling approach known as reversible jump Markov chain Monte Carlo (rjMcMC) sampling is applied to compute the PPD (Dettmer et al., 2012; Pachhai et al., 2015).

In rjMcMC approach, the number of layers is allowed to change (between 1 and 35 from the surface to 100 km depth, below which we define the half-space) and parameters in each iteration are updated through three different moves: birth, death, and perturbation. In the case of a birth move, a new interface at random depth is introduced and proposed with the perturbation of velocity and thickness from a randomly chosen layer. The proposed model is accepted or rejected based on the likelihood ratio of the current model to the previous model. If the proposal is accepted, the model is updated with an additional layer and proceeds for the next iteration. If the proposal is rejected then the current model is retained and a new model is proposed again. In the case of death move, a random layer is picked and proposed to delete (death) with the perturbation of layer thickness and velocity from a randomly chosen layer. Then the same procedure as in the case of the birth stage is followed. In the case of perturbation move, the number of layers remains the same and only layer properties (layer thickness and velocity) are allowed to change.

The sampling approach, particularly rjMcMC can be highly inefficient when significantly low probability regions separate multiple high probability regions. As a result, the sampling takes

a long time to converge to the true model. Therefore, interacting Markov chains are applied here to achieve faster convergence.

2.2.3.1 Depth Resolution Tests

We test the resolution capabilities of the trans-dimensional Bayesian inversion by creating a Rayleigh wave group and phase synthetic dispersion curves for different models with different Moho depth and variable crustal complexities. Figure 2.4 shows the true models used to compute the synthetics and the inversion results. All the true models have crustal velocity structure sandwiched between a sedimentary basin and underlying mantle structure which follows the AK135 model apart from one smooth velocity anomaly. Correlated noise is added to the synthetic dispersion curves.

The experiments show that the trans-dimensional Bayesian inversion is sensitive to the shallow structure given the narrow distribution of the velocities from the ensemble models and uncertainty increases as a function of depth (see the distribution of the darkorange color around the true and predicted models). The inversion is unable to constrain the velocity of the shallow sedimentary layers. This is expected given that our surface wave dispersion curves do not include periods shorter than 5 s. Interestingly, for most of the tests shown in Figure 2.4, the interface probability shows the presence of a shallow layer with a thickness less or equal to 1 km likely corresponding to the sedimentary layer. The presence of this shallow interface may be the result of the large impedance contrast between the sedimentary layer and the crust. When the sedimentary layer is 5 km thick (Figure 2.4f), inversion constrains both the absolute velocity and the location of the discontinuity very well, suggesting that very thick sedimentary basin can be resolved very well.

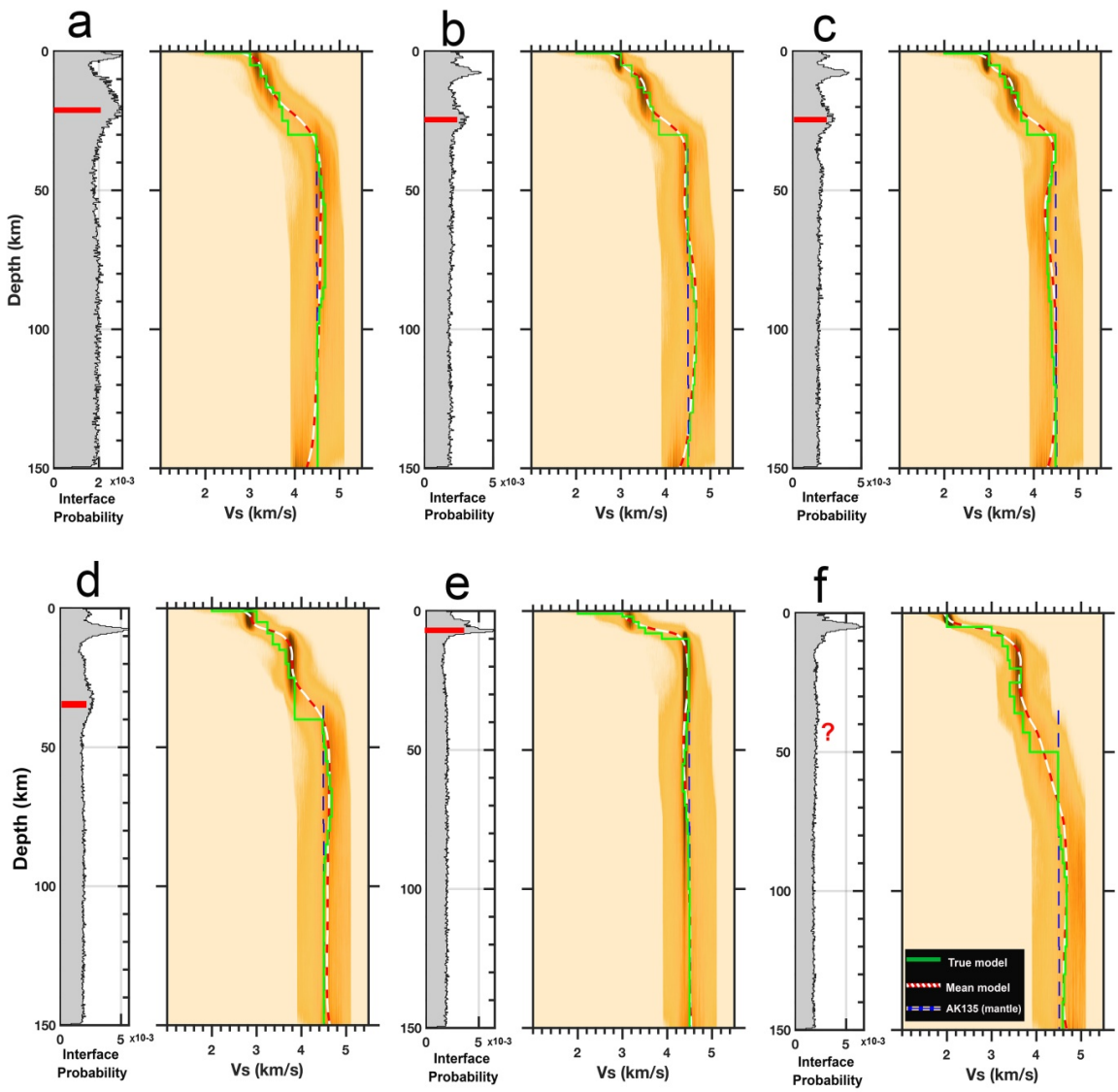

Figure 2.4 Tests showing the depth resolution of the applied inversion method. Here we compare six different true models (green line) to the recovered models (red and white line). Dashed blue lines show the AK135 mantle velocity. The Moho depth is estimated from the interface probability along each velocity depth profile.

We estimate the depth of the Moho from the interface probability (see section 2.2.3.2 below for detail explanations). There are some discrepancies between the recovered and true Moho locations when we use the interface probability approach. In all cases, we observe that the Moho depth is underestimated, possibly due to the smoothing of surface waves across interfaces which makes it difficult to accurately predict the interface location. The differences are ~2 km for the shallow Moho (Figure 2.4e) and ~5 km for deeper Moho (Figure 2.4b-d). For

very complex crustal structure shown in Figure 2.4f, the interface probability is unable to uniquely resolve the Moho. In such a case, we estimate the Moho as the depth where the strongest velocity gradient occurs at a pertinent velocity. When we strongly perturb the input dispersion curves (Figure 2.4a), the Moho depth shows an error of ~10 km. The consistency of the interface probability to provide an estimate of the Moho depth even for models with slightly weak impendence contrast suggest that it is a viable way to estimate the Moho depth from the 1D profiles. However, we have to be cautious about the inherent problem of using surface waves to locate discontinuities which can cause wider uncertainties on the Moho depth location.

The inversion is also able to retrieve all the mantle anomalies down to 150 km in their tendency (positive/negative velocity anomaly with respect to AK135) although the peak amplitude is sometimes underestimated or overestimated. Deeper (Figure 2.4b and f) as well as narrower (Figure 2.4d and e) anomalies are well estimated by the inversion to within 0.3 standard deviation. The inversion underestimates the anomaly in Figure 2.4a but recovers the velocity above the anomaly very well.

2.2.3.2 Moho depth estimation

We estimate the Moho depth topography for the study area by analysing the probabilistic 1D shear velocity-depth profile at each grid node for the depth where there is a probability for a discontinuity at a pertinent shear-wave velocity. The pertinent shear-wave velocity corresponds to velocities > 3.6 km/s, considering that the average shear velocity of the crust is ~3.5 km/s. Surface wave dispersion measurements are generally sensitive to absolute shear wave velocities but are poor in constraining discontinuities. Here, we test the feasibility and accuracy of using the joint inversion of group and phase dispersion measurements applying the trans-dimensional Bayesian inversion method to constrain the Moho discontinuity from the interface

probability. For this experiment, we first compute the group and phase velocity dispersions for 1D velocity model with a Moho at 30 km. Then a correlated noise is added to the synthetic data to make representative observed data (Figure 2.5a and b). These data are then inverted for the shear velocity profile using the trans-dimensional Bayesian inversion method. The first one-third of samples are discarded and the average of the remaining samples are considered to visualize probabilities of discontinuity and S velocity as a function of depths. The inversion results (Figure 2.5c and d) show that the absolute velocities from the true model are well constrained to within 0.2 standard deviation by the average shear velocity structure (red and white dash line in Figure 2.5d), and two strong discontinuities (out of the five from the true model) are recovered at ~2.5 km and ~27 km (Figure 2.5c). We consider the second discontinuity at ~27 km to correspond to the Moho interface, which is set at 30 km in the true model (Figure 2.5d).

For all the test we carried out, we observe that the recovered Moho interface is underestimated. This is to be expected since surface waves smooth across interfaces and are known to have poor sensitivity to the location of discontinuities. As a result, the velocity discontinuity smears out giving maximum probability near the average velocity between layers (e.g., Figure 2.4 and Figure 2.5). Again, we notice that the mean shear velocity at the Moho depth (blue line, Figure 2.5d) does not correspond to the velocity of the underlying mantle but rather an average of the crust and mantle velocities. This sometimes causes the Moho depth when plotted on the velocity sections as shown in Figure 2.13, to cross low-velocity structures which is unrealistic. We estimate the uncertainty associated with the Moho depth by obtaining the difference in depth between the recovered Moho (blue line, Figure 2.5d) and the depth at the start of the mantle velocity (black line, Figure 2.5d) which is where the mean velocity becomes greater than 4.0 km/s. When applied to real data as shown in **Error! Reference source not found.**,

the Moho depth from the interface probability is in good agreement with inferred Moho depths from previous studies in those areas.

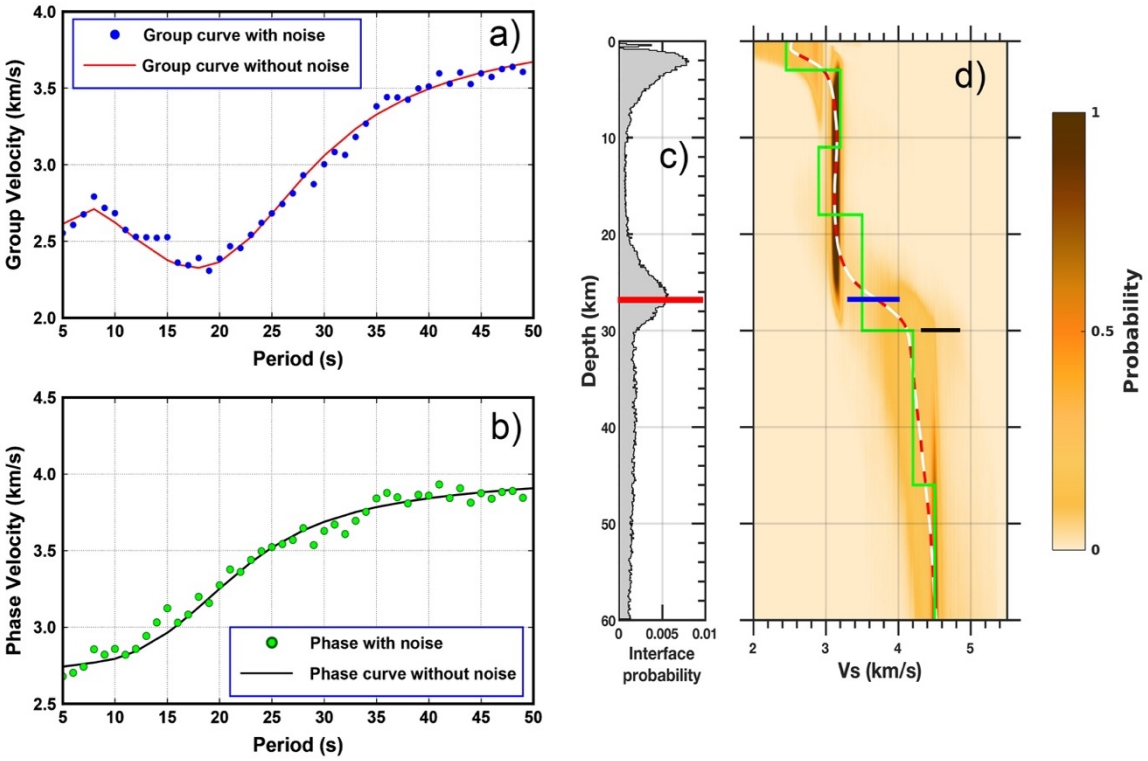

Figure 2.5 Trans-dimensional Bayesian inversion results for synthetic dispersion curves. Synthetic dispersion curves for (a) group velocity and (b) phase velocity with and without noise. (c) The posterior probability for the position of discontinuities. The horizontal red line marks the location of the retrieved Moho discontinuity. (d) Posterior Probability Density (PPD) for shear velocity as a function of depth. The green solid line indicates the true 1D velocity model used to prepare data in a and b. Similarly, the dashed white and red line represent the smooth mean model retrieved from the inversion. We use the depth difference between the blue and the black lines on (d) to estimate the uncertainty of the Moho depth.

2.2.3.4 Inversion of observed measurements

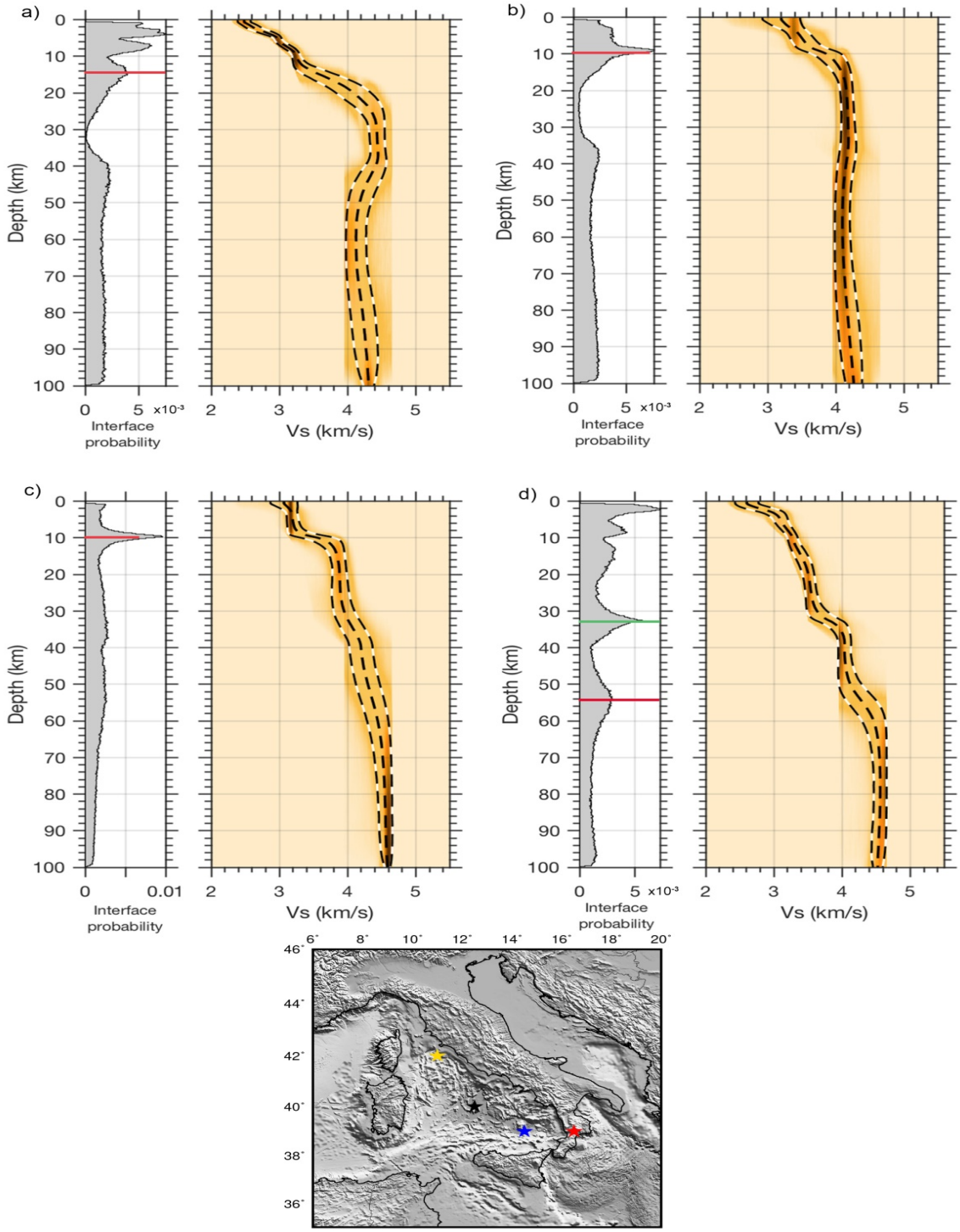

Figure 2.6 Examples of 1D shear velocity-depth profiles. Shear-velocity structure for grid nodes in (a) the northern Tyrrhenian basin (yellow star on map), (b) the Vavilov basin (black star on map), (c) Marsili basin (blue star on map) and (d) Calabria (red star on map). The horizontal red line depicts the depth of the Moho discontinuity estimated in this study. The horizontal green line on (d) indicates a possible double Moho in agreement with previous studies from receiver functions.

Error! Reference source not found. shows how the inversion fared on real data. We show four velocity profiles from the trans-dimensional Bayesian inversion using local dispersion curves extracted from group and phase tomography maps. **Error! Reference source not found.**a is the inversion results for a grid point in the northern Tyrrhenian basin, where the Moho depth is ~16 km (e.g., Moeller et al., 2013). In the Vavilov and Marsili basin, we observe a possible Moho depth at ~10 km (**Error! Reference source not found.**b and c, respectively). The velocity-depth profile beneath Calabria (**Error! Reference source not found.**d) indicates two probably interfaces at ~33 and 54 km, given hints about the possibility of a double Moho in agreement with recent Receiver function results (e.g., Piana Agostinetti & Amato, 2009).

2.3 Results

Surface waves at different periods are sensitive to the earth structure at different depths and for the same period, phase velocity measurements sample deeper structures than group velocity measurements. In general, Rayleigh waves are sensitive to a depth about one-third of their wavelengths. This means for short periods, in this study 5–10 s, group and phase velocities are primarily sensitive to the shear-wave velocity structure of the upper crust. At such short periods, lateral velocity anomalies are mainly attributed to velocity differences between sedimentary basins and the surrounding crystalline rocks. Usually, low-velocity anomalies delineate sedimentary basins, since sediments have low seismic velocities. Rayleigh waves between 15 to 30 s periods, on the other hand, are predominantly sensitive to crustal thickness and lower crust and uppermost mantle shear velocity structure. At these periods, the large seismic impedance contrast across the Moho means that group and phase speeds vary approximately inversely with crustal thickness, with high velocities in regions with a thin crust and low velocities in regions with a thicker than average crust.

2.3.1 Model resolution

There is a variable lateral resolution of our model, due to the variation in path density and azimuthal coverage from the cross-correlation (Figure 2.7). Lateral resolvable structures are on the order of ~30 km in the short-period part of the model and degrade to ~150 km at longer periods (Figure 2.7). In general, the structures beneath the portion of the basin parallel to the Italian Peninsula are highly resolved due to a large number of stations used from this area and consequent good path coverage.

The estimation of the model resolution depends on the path density, azimuthal coverage and average path length (Yanovskaya, 1997). According to Yanovskaya, (1997) and (Yanovskaya et al., 1998), the lateral resolution is estimated by the mean size of an averaging area, which is given by $[S_{min}(x,y) + S_{max}(x,y)]/2$. Here, $S_{max}(x,y)$ and $S_{min}(x,y)$ are semi-major and -minor axes of an ellipse of surface defined by S(x,y) in 2D cartesian coordinates.

Based on depth sensitivities of group and phase dispersion to shear wave velocity (Figure 2.8), the presented short-period velocity maps (5-10 s) have maximum sensitivity in the middle and lower crustal depths in the basin. The intermediate periods sample the uppermost mantle depths beneath the basin, while mainly lower crust is imaged in other regions. The long-period velocities (40-50 s) are predominantly sensitive to the uppermost mantle beneath the study area.

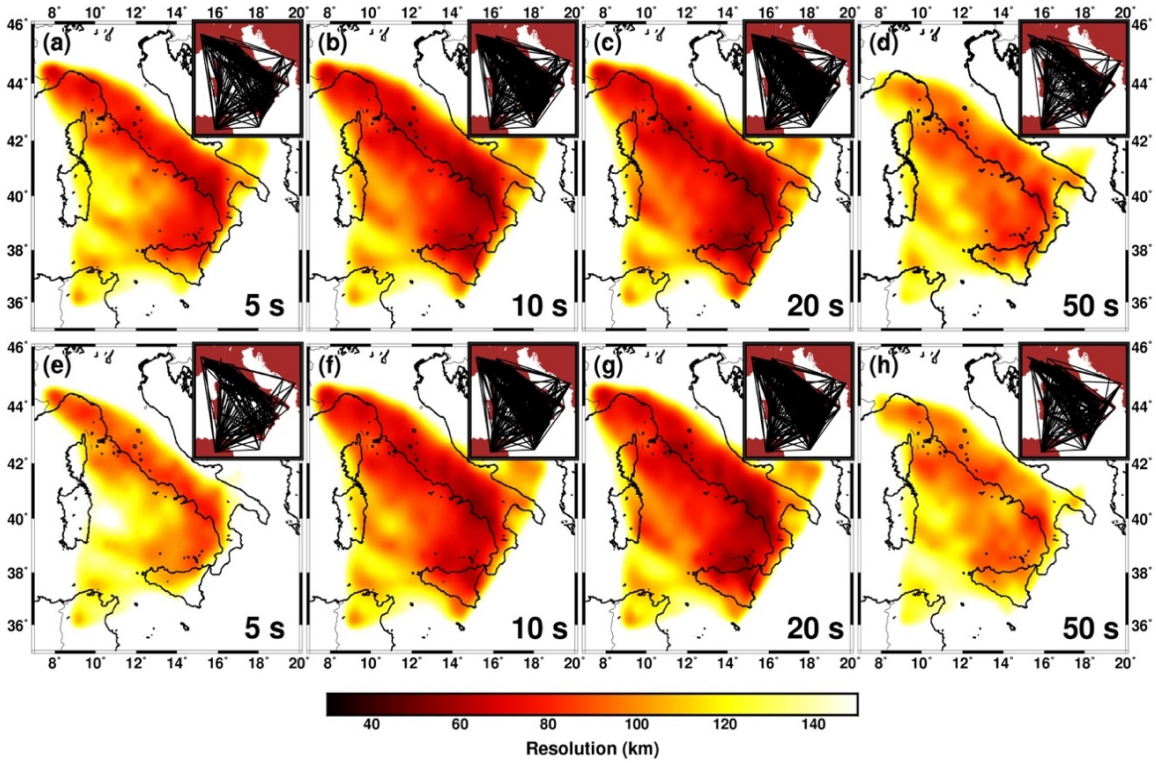

Figure 2.7 The estimated resolution map obtained from the surface wave tomography method. Resolution estimates for (a-d) group velocity and (e-h) phase velocity at 5, 10, 20 and 50 s, respectively. The path density and azimuthal coverage used for tomography inversion at each period is shown on the inset map.

2.3.2 Group and phase tomography maps

Figure 2.9 shows the ambient noise tomography maps for group and phase velocities at different periods (between 5 and 50 s). The tomography maps at short periods (5-10 s, Figure 2.9a-b and Figure 2.9i-j) show pronounced high-velocity anomalies in the southern Tyrrhenian basin, which likely indicates the presence of a high-velocity material at shallow depth. In contrast, the northern Tyrrhenian basin is characterized by low-velocity anomalies which distinguish it from the south, and suggest a different crustal structure compared to the southern Tyrrhenian. A noteworthy observation is that the boundary between the north and south anomalies approximately coincides with the 41° Parallel Line which is generally considered as the divide between the northern and southern Tyrrhenian basin. Observed low-velocity anomalies below the Apennines, Sicily, and the Corsica sedimentary basin are consistent with

previous studies (Di Stefano et al., 2009; H. Li et al., 2010; Moeller et al., 2013) and are likely related to sedimentary basins.

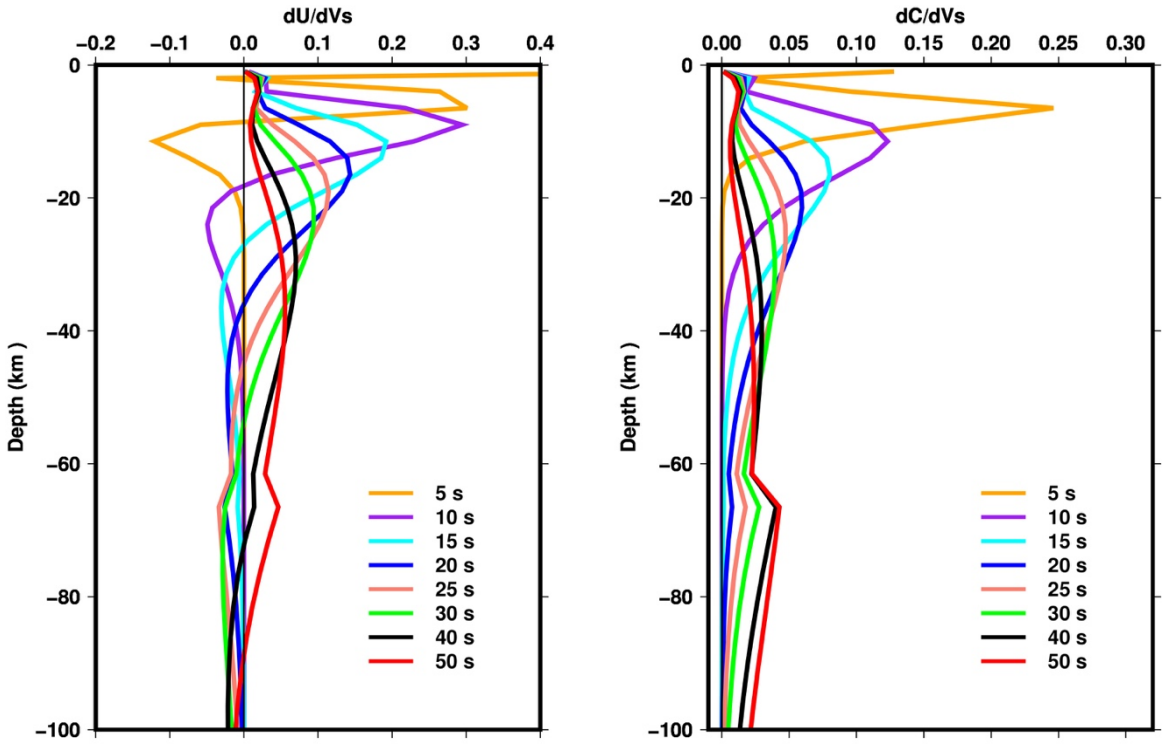

Figure 2.8 Sensitivity kernels for Rayleigh-wave (left) group and (right) phase velocity for different periods.

Velocity maps at 15-30 s periods (Figure 2.9c-f and Figure 2.9k-n) are substantially sensitive to the crustal thickness and the transition between the crust and uppermost mantle. Consequently, high-velocity anomalies in the Tyrrhenian basin likely correspond to the shoaling of mantle material beneath the basin. The low-velocity anomalies coincide with regions having thicker than average crust such as below the Apennines where we observe a continuous low velocity belt mimicking the Apenninic mountain ranges. The long-period group and phase tomography maps (40 and 50 s, Figure 2.9g-h, and Figure 2.9o-p) do not preserve the anomaly contrast at the basin-margin transition as reported in shorter period maps likely due to Rayleigh wave velocities sampling upper mantle materials beneath both regions. Note that the group velocity anomalies are stronger than phase velocity as sensitivity amplitudes are higher for group velocity in comparison to phase velocity (Figure 2.8).

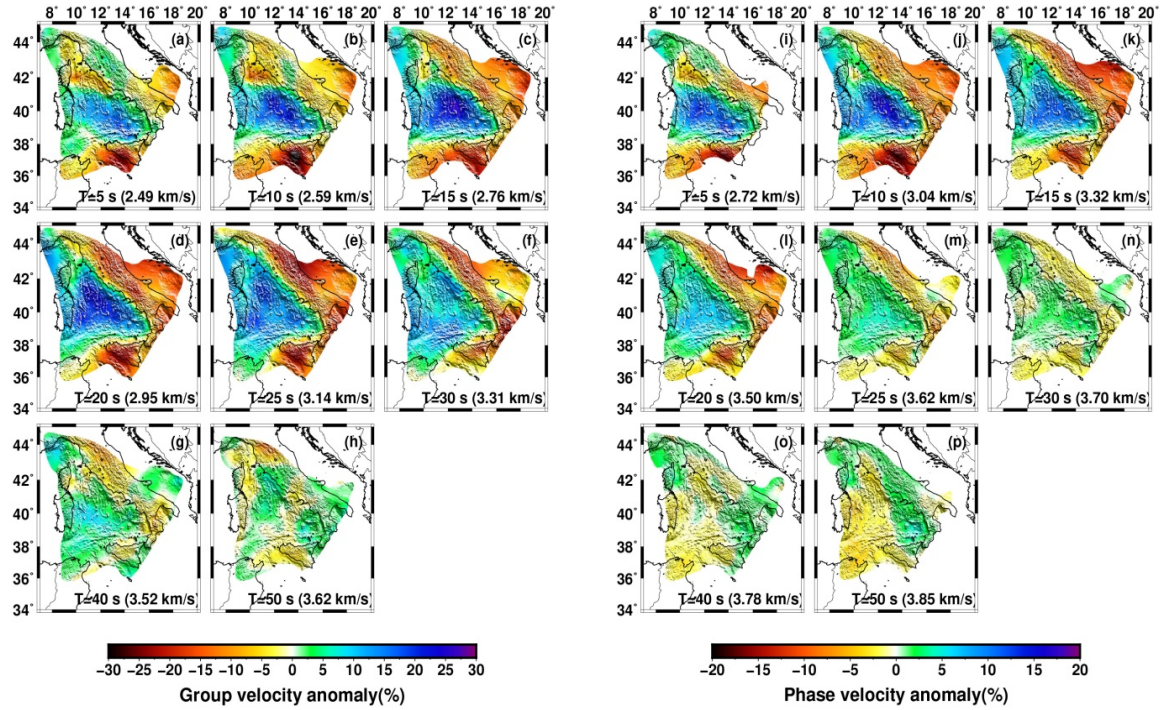

Figure 2.9 Rayleigh wave tomographic maps. (a-h) Group velocity and (i-p) phase velocity maps at periods of 5, 10, 15, 20, 25, 30, 40 and 50 s. Colours represent the percentile deviation from the average velocity at each period shown at the bottom of each plot. Results are shown only for the resolution length shorter than 150 km (Figure 2.7).

2.3.3 Shear velocity structure

We construct a 3D shear-wave velocity model with errors by combining 1D velocity-depth profiles at each node of a 0.5° by 0.5° grid across the Tyrrhenian Sea and its margins. Figure 2.10 and Figure 2.11 show the one standard deviation from the estimated mean S-wave velocity. The uncertainties are higher near the location of interfaces due to the smearing of the velocity structure. Overall, the uncertainties are approximately 0.35 of the mean velocity which suggests that the velocity is reasonably well constrained and well resolved from the surface down to about 100 km.

In Figure 2.12, we plot the mean S-wave velocities on horizontal sections at different depths. In general, the shear velocity model shows similar characteristics as the Rayleigh wave tomography results, yet highlights tectonic and geological features associated with the Tyrrhenian lithosphere. At shallow crustal depths (5-10 km map, Figure 2.12), low shear

velocities are confined to the northern Tyrrhenian basin, Sicily, Calabria, and below the Italian peninsula. The highest velocities occur below the Vavilov basin and are somewhat surrounded by moderate high velocities in the Cornaglia and Campania terraces which extend southeast to reach the Marsili basin.

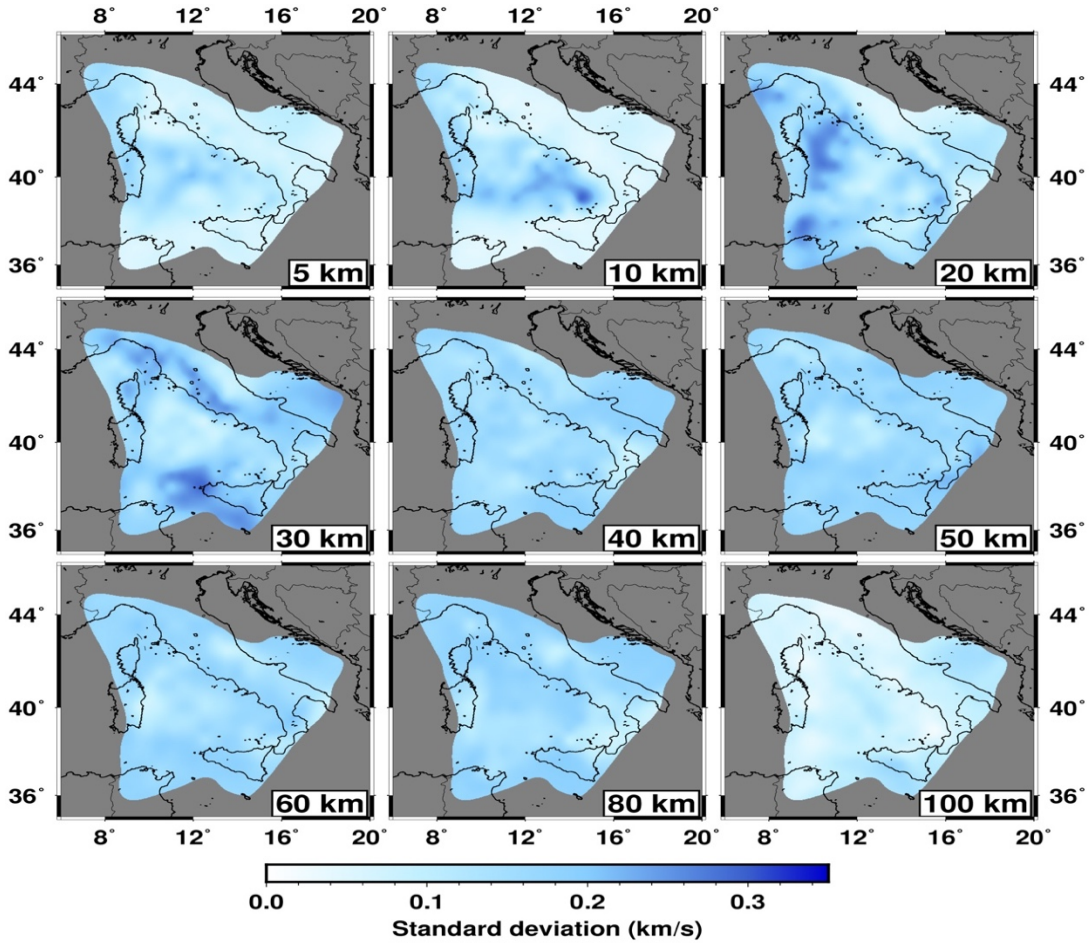

Figure 2.10 Horizontal slices of standard deviations of the 3D shear velocity model.

At 20 km depth (Figure 2.12), we see a clear distinction between the Tyrrhenian basin and its margins, with high velocities delineating the triangular shape of the Tyrrhenian basin. At this depth, we do lose the velocity contrast between the northern and southern Tyrrhenian basin which suggest a likely uniform uppermost mantle structure beneath the basin. Low velocities observed below continental regions can be explained by the presence of crustal material that extends beyond 20 km depth (Piana Agostinetti & Amato, 2009).

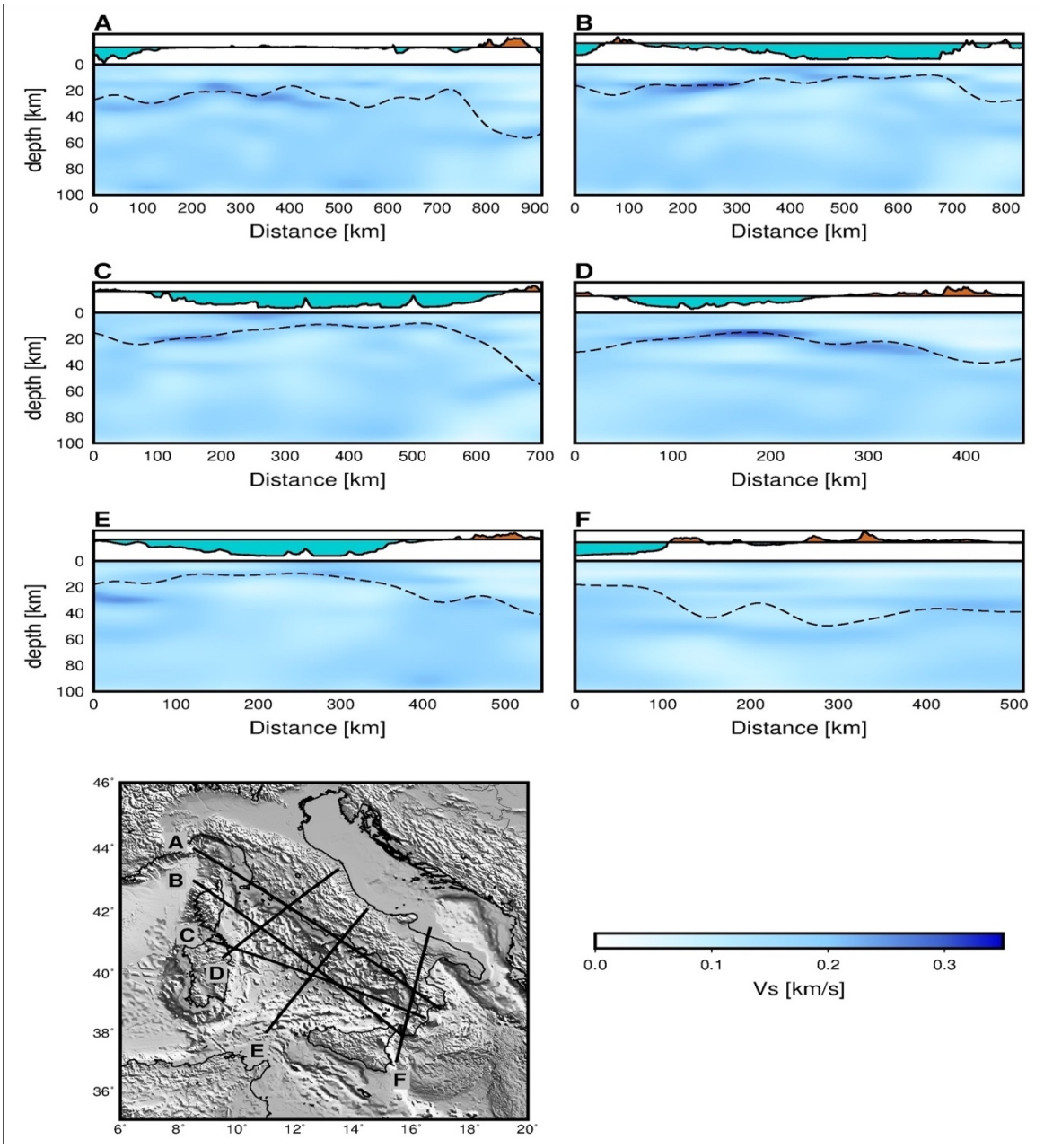

Figure 2.11 Vertical sections of the standard deviations of the 3D shear velocity model along profiles shown in Figure 2.13.The dashed line shows the Moho undulation along the profile.

The 60 km depth map (Figure 2.12) shows a reversal in the velocity pattern, having high velocities beneath the continental regions (Sicily, Calabria, and Italian peninsula) and low velocities below the basin. At depth range from 80 to 100 km, Figure 2.12, low velocities are seen to occupy the southwestern part of the study area, from the Sardinia block to the northwest of Sicily. Interestingly, high velocities are observed in the central part of the basin, beneath the

Vavilov basin. This feature is in agreement with the work by Greve et al., (2014), where the authors found that a nearly-ring shaped low-velocity anomaly surrounds the higher velocities below the Vavilov basin. A noticeable feature at these depths is the high S-velocities beneath Calabria and the southern Tyrrhenian Sea, which is recognized as the subducting Ionian slab (Chiarabba et al., 2008; Chiarabba & Palano, 2017; Neri et al., 2009).

Figure 2.13 shows the velocity-depth vertical cross-sections along six profiles. On these cross-sections, the black continuous line depicts the Moho topography along the profiles based on the maximum interface probability and the dash-dotted line indicates the depth where the velocity becomes mantle velocity and gradient of velocity is approximately infinite. This can also represent approximate uncertainties for the determination of Moho (see Section 2.2.3.2 for details).

The vertical profiles in Figure 2.13 suggest a variable crustal thickness both within the basin and across the margin between the basin and the continental regions. We see that the geometry of the crust is one that thins gradually from about 20 km below the margins to ~10 km beneath the Vavilov and Marsili basins (Profile C and E, Figure 2.13). In the northern Tyrrhenian basin, a crust of ~16 km thick is found (Profile D, Figure 2.13). The greatest crustal thickness is observed beneath Calabria, extending down to the top of the downgoing high-velocity Ionian slab at ~55 km depth (Profiles A and C, Figure 2.13). The crustal thicknesses observed in our model are consistent with previously reported results (Di Stefano et al., 2011; Piana Agostinetti & Amato, 2009; Spada et al., 2013).

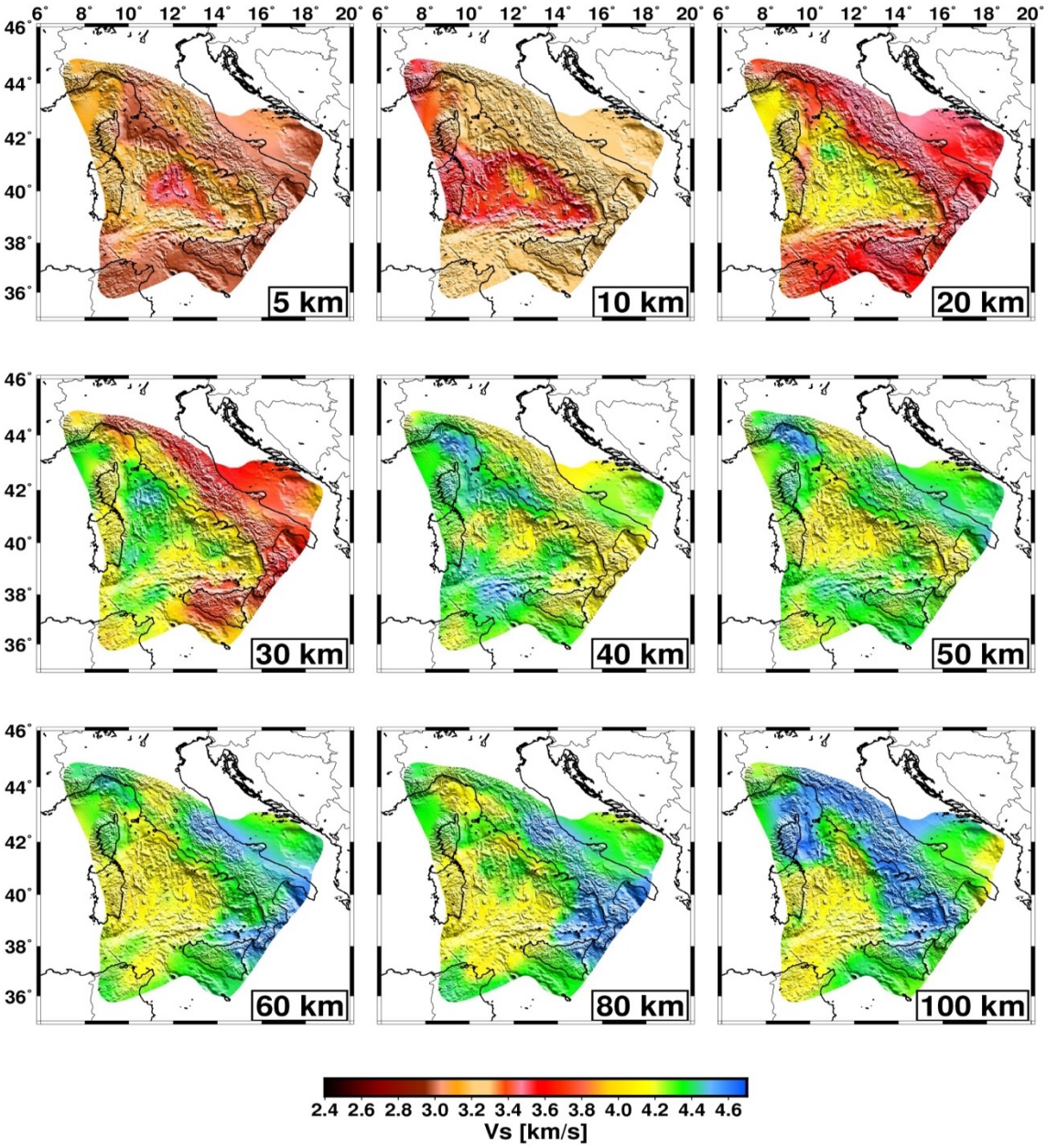

Figure 2.12 Shear velocity model at different depths beneath the Tyrrhenian basin.

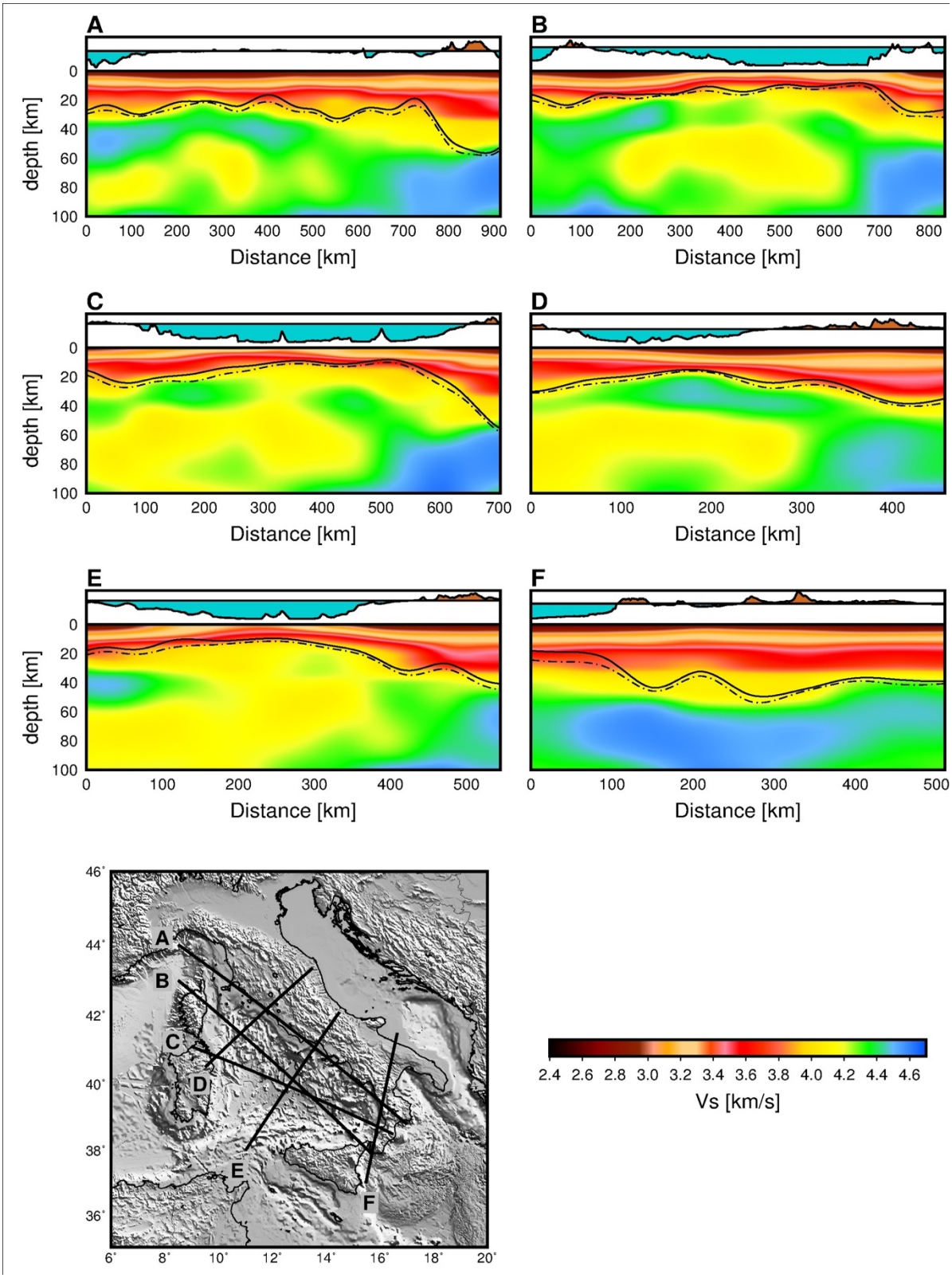

Figure 2.13 Shear velocity structure along six different cross-sections. The black lines on the cross-sections depict the undulation of the Moho along the profile and the dash-dotted line shows the uncertainties of the Moho depth. The depth scale in the cross sections is exaggerated by a factor of 2 or 3 depending on the length of the profile.

We see a low velocity zone emerging at about 40 km and extending to ~80 km depth or the base of the model depending on the area crossed by the profile (Profiles B-E, Figure 2.13). In profile D crossing the Northern Tyrrhenian, Figure 2.13, a high velocity body, likely a remnant of the European lithosphere, sits on top of the low velocity layer. We interpret the high velocity body seen at the start of Profile E (Figure 2.13), as the northernmost part of the African lithosphere. The distribution of velocities in the lithospheric mantle beneath the Vavilov basin in Profile C and E (Figure 2.13), suggests that strong extension that caused the opening of the southern Tyrrhenian may have involved the uppermost mantle, indicated by some form of break-up within the overriding plate. High velocities observed between 35 and 55 km at the start of Profile E is likely related to the African lithosphere and suggests an ongoing compression between the African block and the already extended mantle lithosphere beneath the Tyrrhenian basin. High upper mantle velocities observed below Calabria are associated with the Ionian slab (Profile A-C and F, Figure 2.13).

2.3.4 Moho topography

In general, surface wave dispersion measurements are sensitive to absolute shear wave velocities but are poor in constraining discontinuities. Hence, for most surface wave studies, the Moho interface is taken as the depth of the 4.2 km/s velocity contour (e.g., Lynner & Porritt, 2017). In the Tyrrhenian basin, the complex tectonic history has undoubtedly affected the lithospheric structure and using the 4.2 km/s velocity contour to define the Moho interface in our model produce results that are inconsistent with previous studies. Here, we determine the Moho depth by picking where strong interface probability for a discontinuity occurs at a pertinent shear velocity on the 1D velocity depth profile (See Section 2.2.3.2).

In Figure 2.14, we present a new Moho topography map for the Tyrrhenian basin and margins. The map shows strong lateral variation in crustal thickness but very consistent result within the

different tectonic provinces of the study area. The Moho is very shallow (about 10–12 km thick) below the southern Tyrrhenian basin. We observe similar shallow Moho depths (~11 km) in the northern Tyrrhenian right above the Vavilov basin (Figure 2.14), in agreement with the results from recent wide-angle seismic reflection studies (Moeller et al., 2014). The deepest Moho is found below the northern Apennines and Calabria, where the Moho depths exceeds ~50 km. The general characteristics of the Moho thicknesses found here are very consistent with previously reported depths (Di Stefano et al., 2011; Piana Agostinetti & Amato, 2009; Spada et al., 2013). The significant improvement achieved in our model lies in the resolution of the Tyrrhenian basin's Moho topography which is not well resolved in previous models (e.g., Spada et al., 2013).

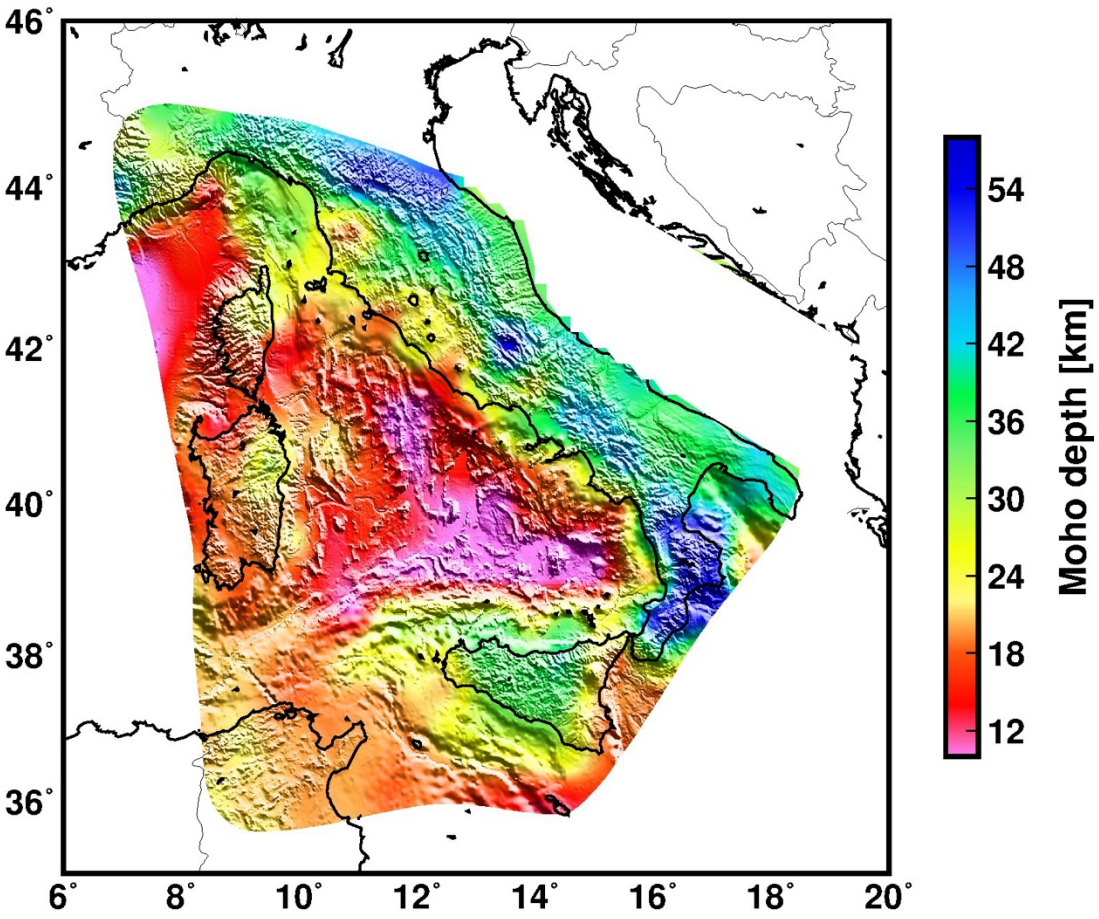

Figure 2.14 Moho topography map for the Tyrrhenian area.

2.4 Discussion

It can readily be seen from Figure 2.9 and Figure 2.12 that two rheologically different domains underlain the northern and southern Tyrrhenian basin. The continental crust under the northern Tyrrhenian basin (Bartole, 1995; Contrucci et al., 2005; Moeller et al., 2013) is characterized by low shear velocities in our model (5 and 10 km maps, Figure 2.12). The nature of the crust in the southern Tyrrhenian basin is rather complex. At shallow depths (< 10 km), we observe the highest velocities in the central part of the basin, below the Vavilov-Magnaghi basin (5 and 10 km maps, Figure 2.12 and Figure 2.15). Here, recent active seismological results suggest that strong extension in the southern Tyrrhenian resulted in mantle exhumation beneath the Vavilov basin (Prada et al., 2014, 2015, 2016) contrary to previous studies suggesting the emplacement of an oceanic crust (Duschenes et al., 1986; K. Kastens & Mascle, 1990). Our highest velocities at crustal depths (profiles A and B, Figure 2.15) occur below the Vavilov basin, which corroborates an exhumed mantle basement below the Vavilov basin (Prada et al., 2014, 2015, 2016). Integrating our crustal model for the Tyrrhenian basin and margins with recent publications (e.g., Prada et al., 2014; Sartori et al., 2004), we see delineation of three basement domains in the southern Tyrrhenian suggested by Prada et al., (2014): stretch continental crust (beneath Sardinia and Campania margins), oceanic crust (beneath Cornaglia and Campania terraces) and exhumed mantle basement (below the Vavilov basin). We interpret the structure of the crust under the Marsili basin as oceanic as supported by recent magnetic studies (Cocchi et al., 2009; Nicolosi et al., 2006).

Remarkably, the contrast in shear velocity structure between the northern Tyrrhenian and the southern Tyrrhenian in our model coincides approximately with the location of the 41° Parallel Line (5 and 10 km maps, Figure 2.12, see also the tomography maps at short periods, Figure 2.9, Section 2.3.2). The 41° Parallel Line is defined as a regional magnetic and free-air gravity

anomaly that is conventionally regarded as separating the northern Tyrrhenian continental structure from the heterogeneous structure in the southern Tyrrhenian (Boccaletti et al., 1990; Bruno et al., 2000; Cocchi et al., 2016; Rota & Fichera, 1987). The structural significance of 41° Parallel Line in the geodynamic evolution of the basin is still debated (Bruno et al., 2000; Cocchi et al., 2016; Malinverno & Ryan, 1986; Spadini & Wezel, 1994), nevertheless, our results provide the first comprehensive seismological evidence for the presence of this lithospheric feature.

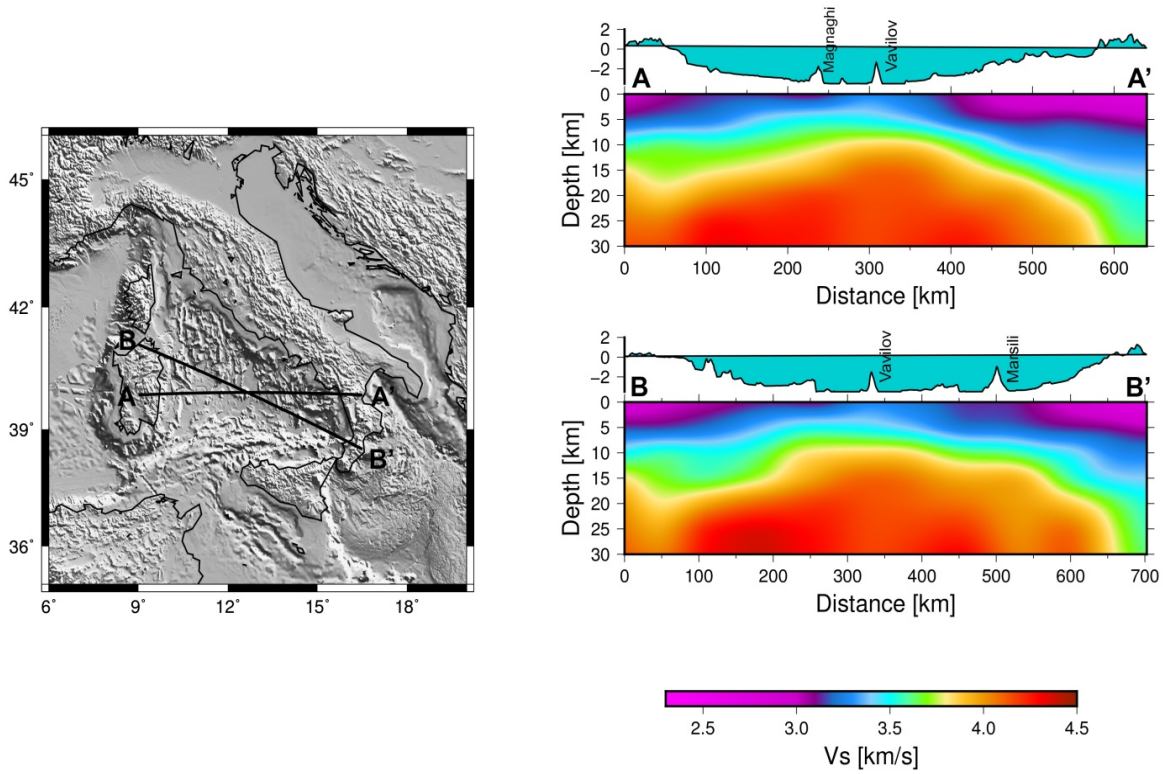

Figure 2.15 Zoom-in of the crustal velocity model in the Southern Tyrrhenian basin. Section A-A' is along the active seismic profile by Prada et al., (2014).

In Figure 2.14, we see two expressions of very shallow Moho (~10-12 km) which we infer to be related to the different style of rifting that opened the north and south Tyrrhenian basin (Faccenna et al., 1997). In the north, we interpret the feature of the shallow Moho oriented approximately N-S as the likely expression of the initial eastward retreat of the Adriatic slab that caused the opening of the northern Tyrrhenian basin (Faccenna et al., 1997; Malinverno &

Ryan, 1986). The second observed shallow Moho feature in Figure 2.14 is oriented approximately NW-SE in the south. This feature is clearly the effect of the ESE retreat of the Ionian slab which resulted in the opening of the south Tyrrhenian basin (Faccenna et al., 2001; Malinverno & Ryan, 1986).

The most pronounced feature in the upper mantle is the presence of a low velocity zone (LVZ) extending from 40 to 80 km and affecting much of the Tyrrhenian basin upper mantle structure (Figure 2.13). Similar velocity decrease has been reported in previous models by Greve et al., (2014) and Marone et al., (2004). Low velocities in the Tyrrhenian upper mantle likely originate from a number of contributing factors. First, asthenospheric upwelling due to lithospheric extension in the basin may cause decompressional melts which can explain the observed low velocities beneath the basin. Second, the likely presence of a hydrous upper mantle structure below the basin due to past subduction and rollback. Last, the effect of mantle potential temperature on velocity.

Generally, variation in seismic velocity simultaneously depends on temperature, pressure, and composition and the uncertainty in the estimation of these controlling factors makes it difficult to separate their effects on velocity (Deschamps & Trampert, 2003). Nevertheless, seismic velocity anomalies in the upper mantle are generally interpreted in terms of temperature, being that the effect of temperature on seismic velocity is thought to be greater than other controlling factors (Giacomuzzi et al., 2012). Wiens et al., (2006) attributed a significant low velocity zone extending from 40 to 100 km depth observed in the shear-velocity structure of four back-arc basins to variations in mantle potential temperature, as the observed velocity decrease shows no apparent correlation with variation in water content.

In the Tyrrhenian basin, Greve et al., (2014) explained the velocity decrease from 70 to 110 km depth range in terms of variations in water content, alluding that temperature plays a smaller

role compared to other back-arc basins (Wiens et al., 2006). However, considering that the strongest lithospheric extension occurred in the central part, beneath the Vavilov basin (Faccenna et al., 2001; Malinverno & Ryan, 1986), we expect the mantle to upwell and decompressional melt to occur similar to a mid-ocean ridge system. The low seismic velocities observed at shallow depth beneath the Tyrrhenian basin is consistent with such a shallow melt zone. We argue that the top of the LVZ at 40 km depth seen in our images (Figure 2.13) suggests that in addition to water content variation and temperature, decompressional melts contribute to the observed LVZ under the Tyrrhenian basin.

Volcanism of the Tyrrhenian basin and its margins shows large variations in time and space reflecting the complex tectonic history of the region. Igneous activities in the southern Tyrrhenian basin emplaced a wide variety of magmatic rocks spanning Mid-Ocean Ridge Basalts (MORB)-, Ocean Island Basalts (OIB)-, and Arc- type geochemical signatures (Peccerillo, 2017b). This wide range of magmatism point to a variety of mantle sources and melting processes (Lustrino et al., 2011; Peccerillo, 2017b; Savelli, 2002). Below the Vavilov basin, our images (Figure 2.13) show low velocities extend from 40 to 80 km depth, well within the estimated range for primary MORB production based on geochemical considerations (Shen & Forsyth, 1995). We infer that the LVZ below the Vavilov basin feeds the Vavilov–Magnaghi shallow structures and may perhaps be the source of MORB- and OIB- type magmatic rocks found here (K. Kastens & Mascle, 1990; Peccerillo, 2017b). Although the LVZ is a broad feature beneath the Tyrrhenian basin (see Profile E, Figure 2.13), it is still interesting that we see a conduit-like feature below the Vavilov volcanic complex which appears to connect the shallow lithospheric structures to the top of the LVZ at 40 km (Profile C, Figure 2.13). Differently from Vavilov, the structure beneath the Marsili seamount is dominated by the high velocity Ionian slab (profile C, Figure 2.13), so volcanism here may require a different dynamics which may not be related to the observed velocity decrease in the upper mantle.

The high velocities observed in our images beneath Calabria and extending under the southeast Tyrrhenian basin, point to the Ionian slab subducting below the Calabrian Arc (Profile A-C and D, Figure 2.13). Tomography results and intermediate to deep earthquakes define the NW subducting slab down to nearly 400 km depth (Chiarabba et al., 2008; Piromallo & Morelli, 2003). A Subduction-Transform Edge Propagator (STEP, Govers & Wortel, (2005)) laterally bounds the distinct edges of the Ionian slab in both the northeast and southwest (Polonia et al., 2016). In profile F (Figure 2.13), we are likely sampling the southwest edge of the Ionian slab, indicated by the clear transition from fast to slower velocities which occur in the proximity of the Ionian Fault (Polonia et al., 2016). This is consistent with multichannel seismic experiment that shows that the Ionian Fault forms part of a complex deformation zone that bounds the southwestern edge of the Calabrian subduction system (Polonia et al., 2016). In the northeast, we do not see a clear boundary of the Ionian slab beneath the southern Apennines but rather we see a flexing of the fast velocity towards shallow depths (profile F, Figure 2.13). The Sicily-Tyrrhenian offshore thrust front (Nijholt et al., 2018) which accommodate the Africa-Europe plate convergence through thrusting type seismicity and structural data (Billi et al., 2006) and connects to the Ionian fault system (Palano et al., 2015) is seen here as a crustal feature affecting the Moho topography (Figure 2.14).

Overall, the geometry of the crust-upper mantle structure beneath our study area is more in favour of a dominant present-day Africa-Eurasia convergence rather than a slab retreat mechanism that was dominant in the last 30 Myr (Nijholt et al., 2018). The nowadays expression of the slab-retreat mechanism is localised at both lateral edges of the Ionian slab, on its transition to the Sicilian domain in the southwest and southern Apennines domain in the northeast. These two edges delineate the thickest crust in our study area and very well localised beneath Calabria known for its low geodetic strain rates (Carafa et al., 2018).

2.5 Conclusion

We determined a 3D shear velocity model for the Tyrrhenian basin from the inversion of Rayleigh wave group and phase velocities derived from ambient noise cross-correlations. The inversion results indicate a pronounced low shear velocity layer in the uppermost mantle, between 40 and ~80 km depth, affecting much of the Tyrrhenian basin. We suggest that this low velocity zone is possibly the source of the MORB- and OIB- type magmatic rocks found in the Vavilov basin. The lateral extent of our Moho topography model likely reflects the initial E-W extension in the northern Tyrrhenian and the successive NW-SE extension in the southern Tyrrhenian which resulted in the formation of the basin. The Moho topography mimics the extent of the Sardinia, Campania and Sicily margins as well as the Cornaglia and Campania terraces and Magnaghi-Vavilov basin which is characterized by high velocity and a very shallow Moho likely reflecting mantle unroofing/exhumation. In the Calabrian subduction zone, we find evidence for the Ionian slab edges within the crust and uppermost mantle structure. This is likely to be associated with tearing to the southwest and flexing (or immature tearing) to the northeast, as well as slab narrowing as reported in recent literature. The 3D crust and upper mantle model favours a geodynamic setting where the dominant process is the Africa-Eurasia convergence while slab retreating seems to be less important but localised nowadays beneath Calabria where the thickest crust and highest seismogenesis is reported.

3 Lithospheric density structure shows no evidence of plume-related rifting beneath the southern Tyrrhenian basin

We jointly analyse shear-wave velocity, surface heat flow, gravity and topography to derive a 3D lithospheric density model for the Tyrrhenian basin and surrounding region. Here, we employ empirical scaling relationships between seismic velocity and density to generate a starting 3D density model, which is then iteratively adjusted through a random walk Monte Carlo algorithm until it reproduces observe gravity and topography. Our density model, extending from the surface to 100 km depth, shows a pronounced ring-shaped low-density upper mantle from 50 to 100 km depth. This buoyant upper mantle feature surrounds the entire southern Tyrrhenian basin which is delineated by a high-density upper mantle. The observed low-velocity but high-density beneath the southern Tyrrhenian basin is likely due to compositional variation and suggest that the southern Tyrrhenian basin is unlikely affected by hydrous fluids from the subduction system. The absence of a buoyant upper mantle at least to the base of our model, suggest that the opening of the southern Tyrrhenian basin may not be related to the ascending of low-density asthenospheric material. We image anomalously dense upper mantle material from 50 to 100 km below the northern Apennines which likely relates to the subduction of the Adriatic lithosphere.

3.1 Introduction

The Tyrrhenian basin is a back-arc basin in the central Mediterranean region which opened within the general framework of convergence between Africa and the European plates (Dewey et al., 1989; Faccenna et al., 2014; Jolivet & Faccenna, 2000; Malinverno & Ryan, 1986). The general understanding is that rifting that resulted in the opening of the Tyrrhenian basin occurred in two stages (Faccenna et al., 2007). Initially, the northern Tyrrhenian basin opened by east-west extension driven by the Adriatic subduction system (Faccenna et al., 2001). The southern Tyrrhenian basin opened in the later stage, being triggered by the roll-back of the subducting Ionian lithosphere (Faccenna et al., 2001, 2007; Malinverno & Ryan, 1986; Marani & Trua, 2002; Pondrelli, 2004). Stronger extension rate in the southern Tyrrhenian basin (up to ~5 cm/yr (Peccerillo, 2017b)), further opened two sub-basins (Vavilov and Marsili basins) during two phases of rapid trench retreat (Cocchi et al., 2009; Dewey et al., 1989; Faccenna et al., 2001, 2007; Kim Kastens et al., 1988; Malinverno & Ryan, 1986; Sartori, 2003; Ventura et al., 2013).

The intriguing geodynamic history of the Tyrrhenian Sea region has been the focus of many studies. It has been well-documented that the northern Tyrrhenian basin is underlain by thinned continental crust (e.g., Moeller et al., 2013, 2014). Contrary, the southern Tyrrhenian basin is underlain by a complex structure comprising of stretch continental crust, oceanic crust and exhumed mantle basement (Kim Kastens et al., 1988; Manu-Marfo et al., 2019; Prada et al., 2014; Sartori et al., 2004). Recent S-wave velocity models (e.g., Greve et al., 2014; Manu-Marfo et al., 2019) reveal several interesting features about the Tyrrhenian uppermost mantle. In particular, Manu-Marfo et al., (2019) found the presence of a broad low-velocity zone (LVZ) whose extent mimics the paleogeographic evolution of the Calabrian Arc. This LVZ affected most of the Tyrrhenian basin uppermost mantle between and is interpreted as the possible source of magmatism in the Tyrrhenian basin. Greve et al., (2014) found that a nearly ring-shaped low-velocity zone surrounds the Vavilov basin at depths between 70 and 110 km.

The Tyrrhenian area is characterized by widespread Cenozoic volcanic activity that shows extreme compositional variations in time and space, highlighting the complex geodynamic evolution of the region (e.g., Peccerillo, 2017). The southern Tyrrhenian basin host several volcanic centres (e.g., Magnaghi, Vavilov, and Marsili) and the Aeolian island arc off the northern coast of Sicily. Several hypotheses have been proposed in the literature to explain the Cenozoic geodynamic evolution and its relationship with magmatism in the Tyrrhenian area.

Figure 3.1 shows that a clear correlation exists between the extensional basins in the central Mediterranean region (Ligurian-provençal basin and Tyrrhenian basin) and strong positive Bouguer regional anomalies. In contrast, long-wavelength negative Bouguer anomalies are correlated with the continental margins or small continental fragments (Italian peninsula and Sardinia-Corsica microplate). It is well established that many geodynamic processes are either directly or indirectly driven by gravity anomalies that arise from spatial variation of rock

density inside the Earth. Thus, the density of the crust and lithospheric mantle supports topography, reflects variation in temperature and lithology, and generates stress within the lithosphere. This makes knowledge of the 3D lithospheric density structure of a region essential, as it provides understanding into not only its temperature and composition but also into its tectonic evolution and modern stress state.

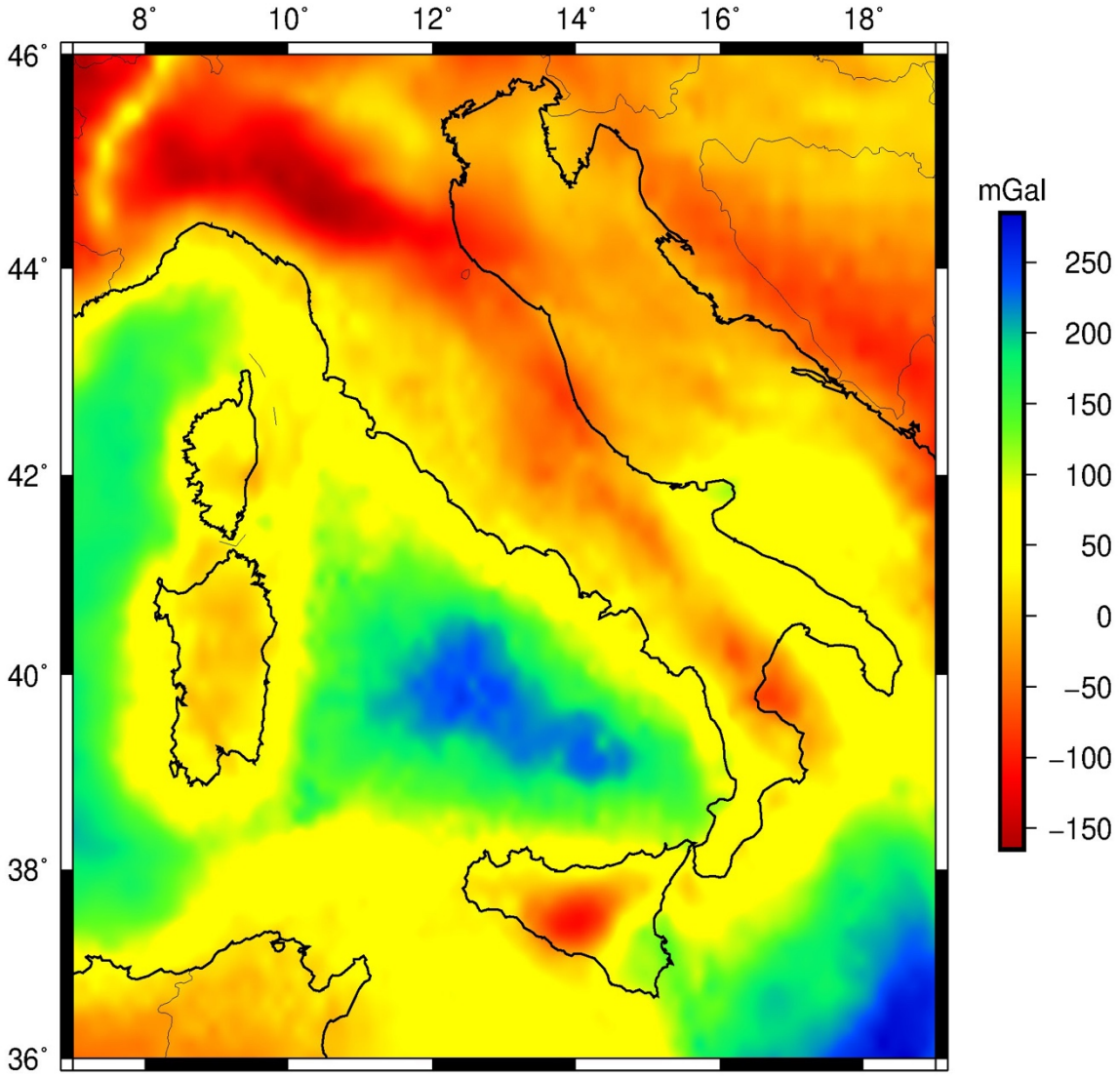

Figure 3.1 Bouguer gravity anomaly map (after Barzaghi et al., 2002) of the central Mediterranean region shows increasing values towards the central Tyrrhenian basin.

Since there is a well-known relationship between seismic velocity and density, many studies have long used seismic velocities to estimate the density structure of the lithosphere (e.g.,

Afonso et al., 2013; Hasterok & Chapman, 2007; Mooney & Kaban, 2010; Sheehan & Solomon, 1991). Here, we combine seismic velocity, surface heat flow, gravity, and topography to develop a 3D lithospheric density structure beneath the Tyrrhenian basin and its surrounding margins. Consecutively, we discuss the rheological variations suggested by this density structure and explore their implications for the geodynamic evolution of the Tyrrhenian basin and associated magmatism.

3.2 Density modelling

Lithospheric density structure is usually modelled from gravity and geoid anomalies. Nevertheless, inference of density from gravity or geoid anomalies poses a non-linear inverse problem with inherent non-unique solutions. In this regard, a more robust answer to the problem is joint inversion with seismic tomography, and other geodynamic data (e.g., topography, crustal motion, earth rotation, laboratory experiments, and heat flow). Here, we use a well-known empirical scaling relation between seismic velocity and density to provide a starting 3D density model. We then employ a Monte Carlo algorithm (Levandowski et al., 2015) to iteratively adjust the initial density model through a series of random-walks until it simultaneously reproduces gravity and topography.

3.2.1 Initial Crustal Density

The initial density model of the crust is derived from shear-wave velocities reported by Manu-Marfo et al., (2019) using well-known regression relation between seismic velocity and density (Brocher, 2005; Christensen, 1996):

$$\rho = -15.84v_s^5 + 209.13v_s^4 + -961.94v_s^3 + 1863.36v_s^2 + -1163.00v_s + 2153.06 \qquad (3.1)$$

This velocity-density scaling relation is sensitive to composition but independent of pressure and temperature; and is well suited to intermediate composition but overestimate the density of felsic rocks and underestimate the density of mafic rocks.

Since density and velocity are both sensitive to temperature and composition, and the relationship between crustal density and velocity due to temperature variations is different from the relation presented in equation 3.1 (Behn & Kelemen, 2003; Levandowski et al., 2013), we apply a temperature correction factor to the density estimates from equation 3.1.

To illustrate the effect of temperature variation on density, consider a crustal material with a density of 2800 kg/m^3, v_s of 3.6 km/s, v_p/v_s of 1.78, coefficient of thermal expansion of 2.5×10^{-5}/°C, and $\partial vp/\partial T$ of 0.5 m/s per °C (Christensen & Mooney, 1995). A 100 °C temperature increase will decrease density by ~7.25 kg/m^3 and shear-wave velocity by ~0.03 km/s. However, if a similar velocity decrease is observed due to composition, then from equation 3.1, this will translate into a density decrease of about 17.6 kg/m^3. Thus, a temperature increase of 100 °C results in a density underestimate of ~10 kg/m^3 (~0.1 kg/m^3 per °C). Consequently, hot material is denser than estimated from equation 3.1 and cold material is less dense than predicted.

Hence, after scaling crustal velocities to density using equation 3.1, we apply a correction factor to account for the departure of the estimated density from an arbitrary reference crustal geotherm (here we use a geotherm of 15 °C/km following Levandowski et al., (2015)) using observed surface heat flow data for the Tyrrhenian region (e.g., Della Vedova et al., 1984; Zito et al., 2003).

Following Levandowski et al., (2015), we compute the temperature correction factor as

$$\Delta T(z) = \frac{zq}{k} - T_{ref}(z) \tag{3.2}$$

where z is the depth, k is conductivity, assumed here to be uniform 3 W/m°C. Then the initial crustal density model corrected for the effect of temperature variation is given by:

$$\rho = \rho_0 + 0.1 \cdot \Delta T(z) \tag{3.3}$$

where ρ_0 is the density estimated from equation 3.1.

High crustal temperatures observed in the Tyrrhenian region (Della Vedova et al., 1984; Zito et al., 2003) suggest melts may be present. The presences of melt have a strong effect on shear-wave velocity but not so much on density. For instance, the presence of 1% partial melt lowers shear-wave velocity by 7.9% (Hammond & Humphreys, 2000) but lowers bulk density by 0.12% (Humphreys & Dueker, 1994). Consequently, the density of melt-bearing crust is much greater than estimated from seismic velocity and surface heat flow data (using equations 3.1-3.3). If we consider a region with an initial shear-wave velocity of 3.7 km/s that undergoes 1% melting such that velocity decreases to 3.4 km/s. In this case, equation 3.1 estimates densities of 2842 kg/m^3 and 2680 kg/m^3 from these velocities, even though there is no significant change in density due to partial melting. Thus from equation 3.1, a shear-wave velocity change due to the presence of 1% melting will cause us to underestimate density by some 162 kg/m^3.

3.2.2 Initial Mantle Density

Mantle densities and velocities also vary laterally as functions of temperature and composition. But because these factors are not fully independent, the uncertainty in their estimation makes it difficult to separate their effects from seismic tomography alone (Deschamps & Trampert, 2003; Mooney & Kaban, 2010). Here, we assume that the starting density model accounts for temperature variation but insensitive to compositional variation, by assuming that lateral velocity changes come about due to variation in temperature and that the mantle is isochemical (e.g., Deng et al., 2017; Levandowski et al., 2015). We use published estimates of bulk and shear moduli and their pressure- and temperature-derivatives along with temperature-dependent thermal expansivities for olivine, garnet, spinel, orthopyroxene, and clinopyroxene to estimate elastic S-velocity as a function of temperature. Then, we account for anelastic

reductions of velocity by calculating the Laplace transform of the temperature-, pressure-, and seismic-period-dependent creep function (Levandowski et al., 2015).

Accounting for a wide range of mantle minerals, a velocity perturbation in the mantle scales to density perturbation as:

$$\Delta\rho = \Delta v_s \times \left(7.3 - \frac{z}{100\ km} + \frac{\Delta v_s}{4}\right);\ \Delta v_s \leq 6\% \tag{3.4a}$$

$$\Delta\rho = \Delta v_s \times \left(8.8 - \frac{z}{100\ km} + \frac{7(\Delta v_s - 6)}{40}\right);\ \Delta v_s \geq 6\% \tag{3.3.4ab}$$

Where v_o= 4.4 km/s; ρ_o= 3200 kg/m^3 are assumed to be the reference velocity and density at the solidus respectively and the velocity perturbation (Δv_s) relative to the solidus velocity (v_o) is given by:

$$\Delta v_s = \frac{(v_s - v_0)}{v_0} \times 100 \tag{3.3.4ac}$$

Since the reference is meant to be the solidus (i.e., assuming that the adiabatic temperature in the asthenosphere is quite near the solidus), velocities below v_o may reflect increasing melt content, which does not affect density. Therefore, there is a final implicit segment of the piecewise-continuous velocity-density relationship:

$$\Delta\rho = 0; \qquad \Delta v_s \leq 0\% \tag{3.3.4ad}$$

This velocity-density scaling relation is relatively insensitive to compositional variation, even though compositional variation is the most important likely difference between fertile and melt-depleted upper mantle (e.g., Godey et al., 2004). Melt extraction preferentially removes iron, volatiles, aluminous phases such as garnet and spinel, leaving behind a dry residue mantle enriched in olive and magnesium. Empirical correlations among Mg# (Mg# =[Mg]/[Mg + Fe]), seismic velocity, and density (Schutt & Lesher, 2010) suggest that a unit increase in Mg#

correlates with a 0.4-0.5% (13 kg/m^3) decrease in density and a 0.25-0.45% (~0.015 km/s) increase in velocity. Since the latter would translate as a 2 kg/m density increase, a unit increase in Mg# results in a density overestimate of 15 kg/m^3 assuming that all velocity variations are thermal in origin, equation 3.4a.

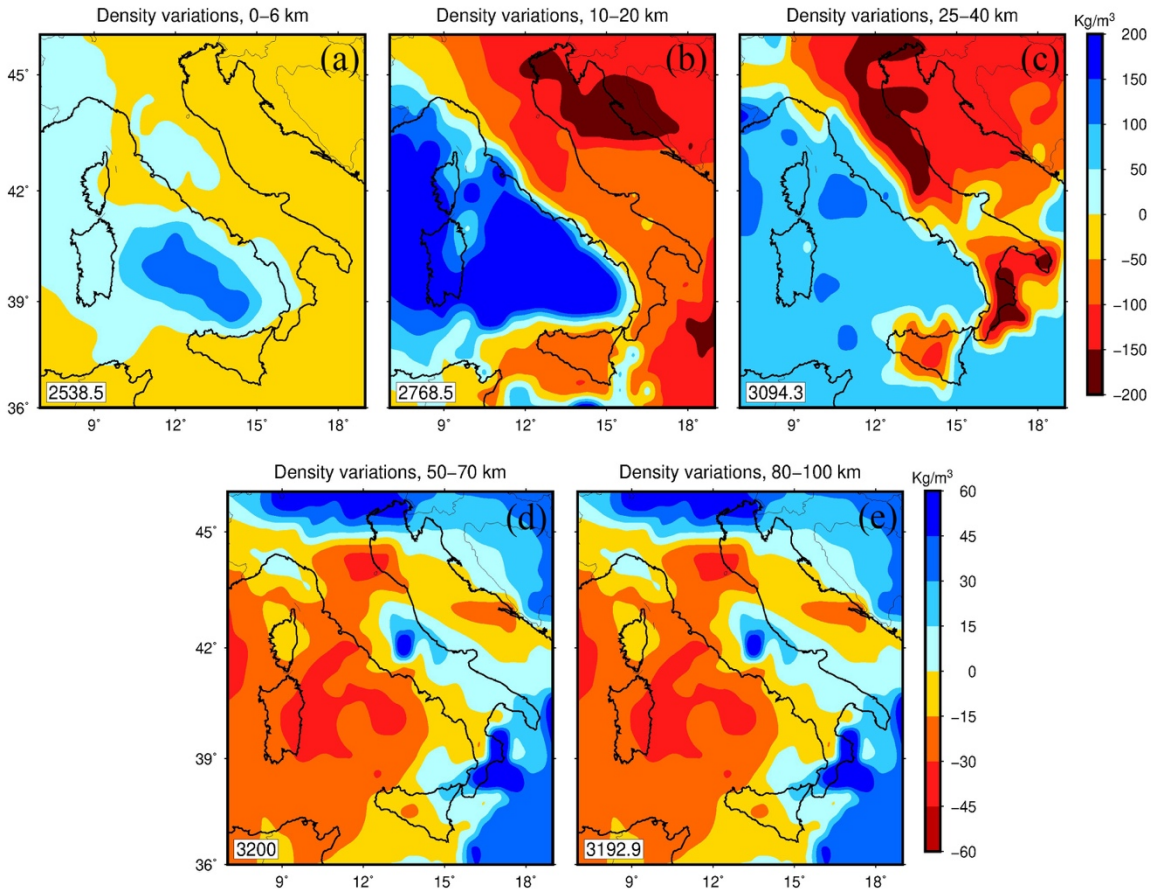

Figure 3.2 Initial density variations estimated from seismic velocity and temperature.. The mean (located at the bottom left corner) is removed from each layer for ease of comparison.

Similarly, hydration of mantle peridotite results in decreasing seismic velocity but also drastically lowers density (Christensen, 2004). A 0.5% (~16 kg/m^3) decrease in density is associated with each 1% decrease in velocity. The density decrease associated with 1% hydration-induced slowing is twice as great as the decrease in density associated with 1% temperature-induced slowing (Christensen, 2004). As a result, scaling seismic velocity to density assuming that observed mantle seismic velocity variation reflects solely lateral

temperature heterogeneities should lead to underestimated values of density in areas of hydrous mantle lithosphere.

3.2.3 Refining the density model

The initial density model derived from equations 3.1 - 3.4a is interpolated on a 50 × 50 km grid that extends well beyond the study area to minimize edge effects. The lithosphere is divided into 24 laterally varying layers: surface to sea level (defined at the depth at 0 km), 5 layers of 2 km thickness from sea level to 10 km, and 5 km thick layers from 10 km to 100 km depth, with each cell, have a uniform density.

The initial density model predicts local isostatic topography, E as (Lachenbruch & Morgan, 1990):

$$E = H - H_0; \qquad H = \int_0^{z_a} \frac{\rho_a - \rho(z)}{\rho_a} dz \tag{3.5}$$

H_0 is a correction term of 2.4 km to achieve isostatic equilibrium with an asthenospheric column. Local buoyancy is controlled by lithospheric flexural strength. Convolution of E with the flexural filter of the lithosphere, F, accounts for flexural smoothing and produce the smoothed surface elevation field $\varepsilon_{predicted}$ that is predicted by the 3D lithospheric density model:

$$\varepsilon_{predicted} = E \cdot F \tag{3.6}$$

Here, F is a system of zero-order Kelvin–Bessel functions (Watts, 2001) based on the elastic thickness across the study region (e.g., Kaban et al., 2018). Similarly, the convolution of observed surface elevations with F produces a smoothed elevation field, $\varepsilon_{observed}$. For the estimated lithospheric density structure to be plausible, $\varepsilon_{predicted}$ must match $\varepsilon_{observed}$ within some tolerance.

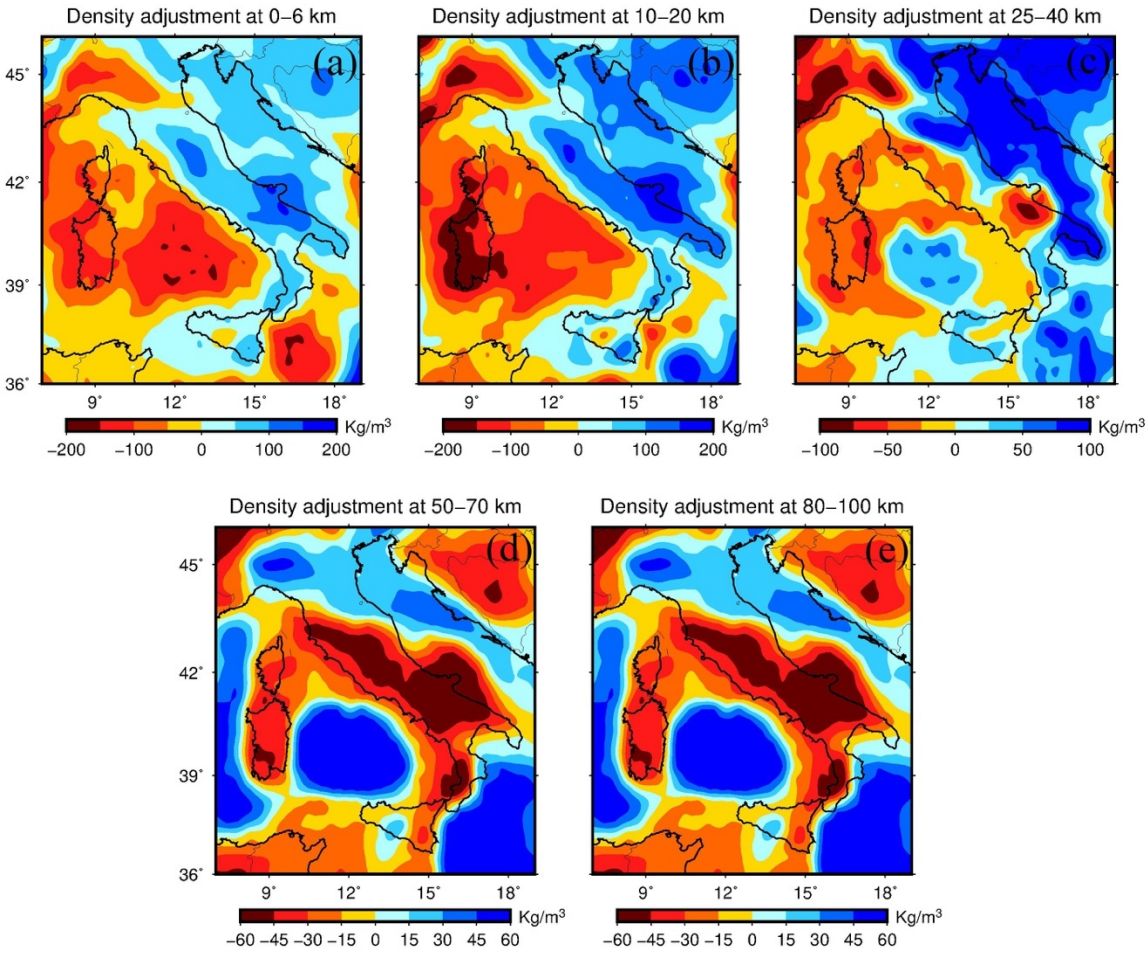

Figure 3.3 Density adjustments made to the seismically estimated densities shown in Figure 3.2 in order to reproduce gravity and topography.

Usually, the gravity and topography variations predicted by the initial density model differ from observations. The residual gravity (Gr) and topography (Hr) which highlight these inconsistencies between the observations and predicted values is computed as:

$$G_r = G_{observed} - G_{predicted}; \qquad H_r = \varepsilon_{predicted} - \varepsilon_{observed} \tag{3.7}$$

That given the failure of the initial density model to recover observed gravity and topography, we employ a random-walk Monte Carlo algorithm by Levandowski et al., (2015), which iteratively refines the initial 3D density model until gravity and topography are simultaneously reproduced to within 10 mGal and 100 m at all points in the study area.

Because gravity and topography are inherently non-unique functions of the 3D density structure, we conduct more than 2000 Monte Carlo simulations and present the mean model across all the plausible density models in Figure 3.4. Figure 3.3 shows the mean adjustment made to the initial starting model. At short wavelengths, these adjustments may represent features below the resolution of the shear-wave velocity model. However, broad adjustments possibly reflect compositional variation in the mantle lithosphere and anomalous v_p/v_s ratios in the crust (since the starting model systematically underestimate and overestimate the density of mafic and felsic rocks respectively).

3.3 Results

3.3.1 Tyrrhenian basin

The crust beneath the southern Tyrrhenian basin is complex (comprising of stretched continental crust, oceanic crusts, and exhumed mantle basement (e.g., Manu-Marfo et al., 2019; Prada et al., 2014)) and both Vs and density at 0-6 km reflect these characteristics. Figure 3.2a and Figure 3.4a shows a high-density material oriented NW-SE below the southern Tyrrhenian basin, although the density model (Figure 3.4) predicts a much less dense material than Vs (Figure 3.2). Extension in the southern Tyrrhenian basin has been accompanied by thinning to complete break-up of the crust, volcanic activity and high heat flow. The observed high heat flow values in the southern Tyrrhenian basin, > 150 mW/m^2 (Della Vedova et al., 1984; Zito et al., 2003), suggest that the high-velocity, high-density feature observe here is more related to composition.

The northern Tyrrhenian basin which lies between Corsica and the northern Apennines has a moderately thinned continental crust and its evolution is not related to the Ionian subduction. Here, both Vs (Figure 3.2a) and density (Figure 3.4a) show a less dense material that extends from the eastern coast of Corsica to the coast of Tuscany.

Between 10 and 20 km depth (Figure 3.4b), a much broader high-density body is observed here that extend from the north to south Tyrrhenian basin. Similar densities are observed in the Ligurian-Provençal basin which leads us to infer that this high-density feature corresponds to uppermost mantle below the extensional basin. The Moho depth is ~10 km in the southern Tyrrhenian basin and about 16 km below the northern Tyrrhenian basin (Di Stefano et al., 2011; Manu-Marfo et al., 2019; Moeller et al., 2013). The patch of high-density beneath the northern Tyrrhenian basin at depths between 25 and 40 km (Figure 3.2c and Figure 3.4c) may be related to the post-orogenic granitoids found in the northern Tyrrhenian basin (Savelli, 2015).

High-density mantle bounds the southern Tyrrhenian basin from 50 to 100 km depth. In contrast, a low-density mantle is imaged below the northern Tyrrhenian basin, Sardinia-Corsica, the Italian peninsula, and North Africa, thus forming sort of a ring-shape low-density anomaly around the high-density mantle beneath the southern Tyrrhenian basin. Similar ring-shape anomaly patterns have been observed in previous seismological studies (e.g., Greve et al., 2014; Manu-Marfo et al., 2019; Marone et al., 2004) but on a smaller spatial scale.

3.3.2 Apennines

We image a dense upper crust along the Apenninic orogenic belt from Calabria to Tuscany (Figure 3.4a). The Po plain basin located north of the northern Apennines and south of the Alps host sediments to depths of about 5-11 km, and although not seen on the Vs, the density at 0-6 km depth (Figure 3.4) reflect this material. Recent seismicity and geodetic studies about the lithospheric deformation in the central Mediterranean have shown that extension occurs along the Apennines from Calabria to Tuscany and shortening occur in Sicily and the eastern Alps (D'Agostino et al., 2008; Faccenna et al., 2014).

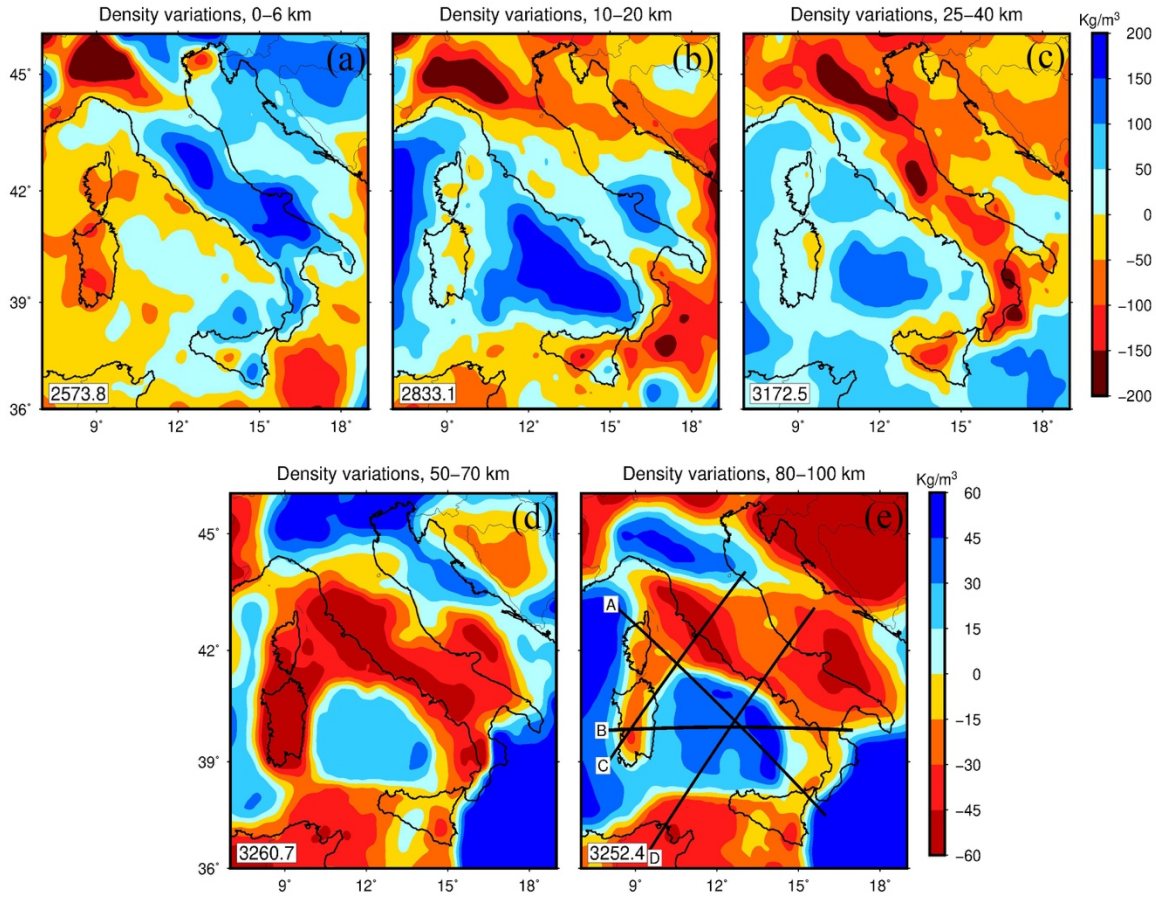

Figure 3.4 Average final density model at the depths shown. The mean (bottom left corner) has been removed from each layer. Cross sections A, B, C, and D are shown in Figure 3.6.

In the lower crust (Figure 3.4c) we see a continuous belt of low-density mirroring the Apenninic orogenic belt from the northern Apennines to Calabria. The crustal thickness below the Apennine orogeny ranges from 30 km to >50 km in some areas (Manu-Marfo et al., 2019; Piana Agostinetti & Amato, 2009; Spada et al., 2013). It is likely that the spot of buoyant material dotted along the Apennine mountain range (Figure 3.4c) reflects areas with deep crustal roots.

The mantle below the central and southern Apennines is less dense particularly beneath Tuscany and the along the western margin of the Italian peninsula down to Campania. Contrarily, the northern Apennines overlie a dense mantle (Figure 3.4d-f), and this feature may

be related to the subduction of the Adriatic slab beneath the northern Apennines (Di Stefano et al., 2009).

3.3.3 Adriatic and Dinarides

Because the Adriatic and Dinarides areas are not well resolved by the seismic velocity model (Manu-Marfo et al., 2019), our initial model (Figure 3.2) shows a relatively uniform structure from the Apennines to the Dinarides, inconsistent with known structural heterogeneities observed in high resolution seismic studies (e.g., Mele et al., 1998; Yang et al., 2007). Nevertheless, this uniform structure observed in the initial model is almost entirely replaced, owing to the density refinement that jointly utilises seismic, gravity and topography data to constrain the final density model (Figure 3.4).

The most prominent feature of the upper mantle below the Dinarides is the broad low-density characteristics of the mantle (Figure 3.4d-f). The crust below the Dinarides is thick (e.g., Stipčević et al., 2011) and this buoyancy is manifested in the low densities observed from 25 to 40 km depth (Figure 3.4c).

High-density mantle bounds the northern Adriatic Sea from 50 to 70 km depth (Figure 3.4d). This high-density anomaly appears to broaden beneath the Po basin and the northern Apennines (Figure 3.4d-e). At mid-lower crustal depth (Figure 3.4b-c), the Adriatic Sea shows low-density characteristics in the northern sector and relatively high-density characteristics in the south.

Recent seismicity and geodetic evidence (e.g., D'Agostino et al., 2008) suggest that the Adriatic promontory is fragmented into two submicroplates. The first is the Adria microplate which includes the northern Adriatic Sea region and the Po plain basin, and the second microplate includes the Apulian promontory, the Ionian Sea, and possibly the Hyblean region in southern Sicily and these two submicroplates rotate in such a way as to accommodate the Eurasia-African relative motion.

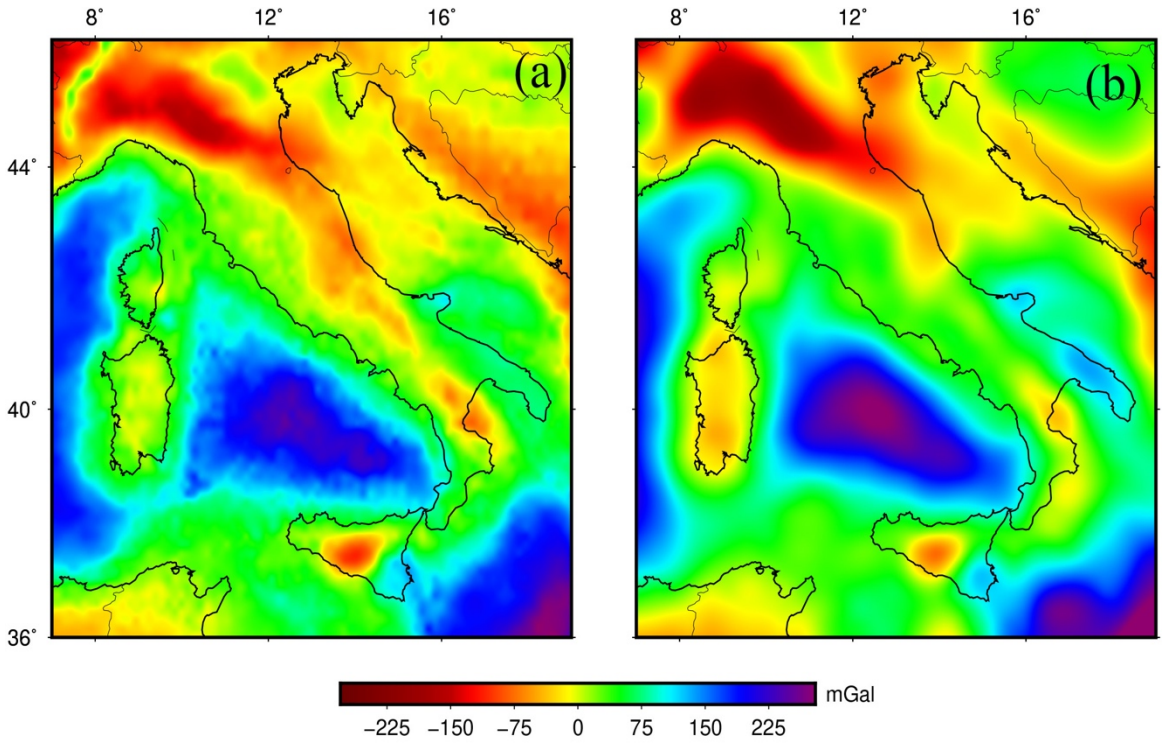

Figure 3.5 a) Observed Bouguer gravity anomaly vs b) Bouguer gravity anomaly computed from the final density model shown in Figure 3.4.

3.3.4 Sardinia-Corsica block

The upper mantle beneath the Sardinia-Corsica block show low-density characteristics, marking the western extent of the buoyant material that surrounds the southern Tyrrhenian basin (Figure 3.4d-e). Different from the upper mantle, the crust below the Sardinia-Corsica block is not anomalous compared with the rest of the region (Figure 3.4a-c).

3.3.5 Ligurian-Provençal basin and the Ionian Sea

The Ionian Sea has been described as the last remaining segment of the Mesozoic oceanic lithosphere subduction in the central Mediterranean (D'Agostino et al., 2008; Faccenna et al., 2001; Jolivet & Faccenna, 2000; Speranza et al., 2012). Figure 3.4 shows that the Ionian Sea and the Ligurian-Provençal basin are mapped as high-density areas from 25 to 100 km depth. Oceanic lithospheres such as the Philippine Sea and the Pacific Sea have been mapped by similar high-density mantles (e.g., Li et al., 2014).

3.4 Discussion

The 3D density model of the lithosphere below the Tyrrhenian region shows strong lateral variations in the crust and uppermost mantle that are related to the complex tectonic evolution of the study area. The density structure of the lithosphere generally mirrors seismic velocities, however, it is essential that this density structure reproduce observed gravity anomalies. Whiles we observe some inconsistencies between the velocity model (Figure 3.2) and density model (Figure 3.4) particularly in the mantle, the density model is able to recover most of the observed gravity anomalies in the study area (Figure 3.5). Thus, the concordance between the observed and predicted gravity anomalies provide a good confidence in the density model.

Two striking features highlighted by the model (Figure 3.4) are the dense mantle material that delineates the entire southern Tyrrhenian basin between 50 and 100 km depth and the ring-shaped low-density material that roughly surrounds it.

It is reasonable to think that the Tyrrhenian mantle contains water due to the evolution of the Adriatic-Ionian subduction system which may have caused hydrous fluids produced by the subducted slab to contaminate the mantle. Such a hydrated mantle could decrease velocity but drastically decrease density, by approximately 16 kg/m^3 for each corresponding 1% reduction in velocity (e.g., Christensen, 2004; Hacker & Abers, 2004). Below the northern Tyrrhenian basin, Sardinia-Corsica block and Tuscany, we find that density values are less than we initially estimated (Figure 3.2), and we suggest that the observed low-density anomaly most possibly reflect a hydrated mantle. We, however, do not discard the possibility that the low-density characteristics below Tuscany and possibly Sardinia may be due to upwelling of a low-density asthenosphere which may have connections with the volcanism in these areas (Peccerillo, 2017a).

Below the southern Tyrrhenian basin, we observe a low-velocity (Figure 3.2) but high-density (Figure 3.4) upper mantle. Seismic velocities in the upper mantle mainly reflect its temperature regime and hence the absence of a direct relationship between seismic velocity and density suggest that the observed high-density characterises is likely related to compositional variation.

Contrary to the northern Tyrrhenian basin, where extension was accompanied by crustal thinning, the opening of the southern Tyrrhenian basin was accompanied by oceanic basin formation resulting from the rapid roll-back of the retreating slab (Faccenna et al., 2001; Malinverno & Ryan, 1986; Sartori, 2003; Ventura et al., 2013). From paleogeographic evolution of the Calabrian subduction system, one could expect that the southern Tyrrhenian basin mantle is contaminated with water which will cause the density to decrease. However, it is likely that the concentration of fluids is low due to the fast roll-back of the slab during the opening of the southern Tyrrhenian basin, causing a large influx of mantle material not affected by subduction.

The geodynamics and magmatism of the Tyrrhenian region is complex and different hypotheses have been proposed to explain the Cenozoic geodynamic evolution and its relationship with magmatism in the Tyrrhenian region. One such hypothesis explains the evolution and magmatism in the Tyrrhenian area as due to upwelling of deep-rooted mantle plume impinging upon the lithosphere (e.g., K. Bell et al., 2013; Keith Bell et al., 2004; Vollmer, 1976). Locardi & Nicolich, (1988) proposed upwelling of soft, low-density mantle rocks as an active mechanism of formation of the Tyrrhenian basin and associated magmatism. Unless such a low-density mantle is only present below 100 km depth beneath the southern Tyrrhenian basin, this prediction is at odds with the density model as we image dense mantle below the southern Tyrrhenian basin (Figure 3.6).

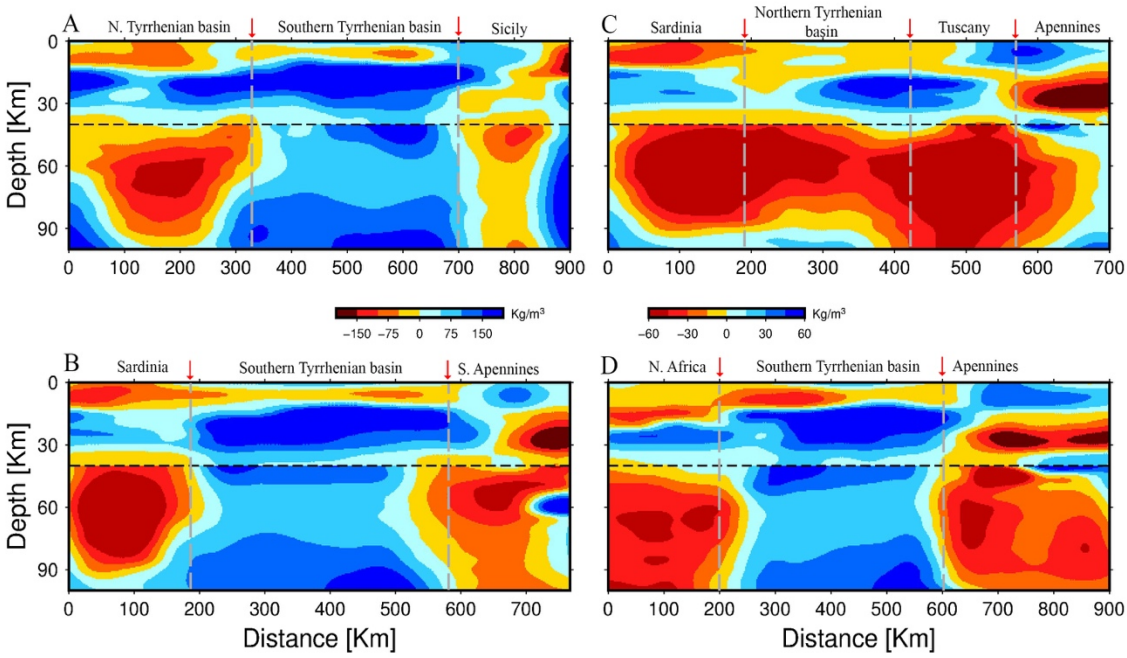

Figure 3.6 Cross-sections through the average final density model. Profile locations are shown on Figure 3.4e. The lines at 40 km are used to divide the density anomaly into two parts with different colour scales (±200 kg/m^3 for the upper part, ±60 kg/m^3 for the lower part).

3.5 Conclusion

We have derived a 3D image of lithospheric density below the Tyrrhenian region from seismic velocity, surface heat flow, gravity and topography models. Here, we employ a Monte Carlo algorithm to iteratively refine the initial density model obtain from seismic velocity until it reproduces gravity and topography. The final 3D lithospheric density model shows that the density of the lithosphere below the Tyrrhenian region is heterogenous plausibly due to the complex geodynamic evolution of the central Mediterranean region.

We find a nearly ring-shape low-density mantle that appears to surround the southern Tyrrhenian basin. We suggest that this buoyant material is the result of hydration of the mantle by subduction-derived fluids but we however do not rule out the possibility that this buoyant material may be due to asthenospheric upwelling.

Along the Apennines, we image a nearly continuous band of low-density material in the lower crust from Calabria to the northern Apennines, mirroring the deep roots of the Apenninic orogenic belt. We found different density anomalies bound the Adria microplate and the newly defined Apulia microplate in the Adriatic Sea.

We observed high-density characteristics beneath the southern Tyrrhenian basin similar to the density structure below the Ionian and Ligurian-Provençal oceanic lithospheres. The absence of a buoyant upper mantle at least to the base of our model, suggest that the opening of the southern Tyrrhenian basin may not be due to the ascending of low-density asthenospheric material.

4 Dynamics of the active deformation beneath the Tyrrhenian basin and surrounding margins

The Lithospheric deformation, mantle flow, and tectonic stress state in the Tyrrhenian region are influenced by the structure, density, and effective viscosity of the crust and uppermost mantle beneath the basin. Here, we estimate the contribution of buoyancy forces to the regional dynamics by developing a 3D Pylith finite-element model to compute the contemporary lithospheric flow field below the Tyrrhenian basin and surrounding margins. We use as input, viscosity and density models derived from S-wave seismic velocities. The modelled lithospheric flow pattern is consistent with the northeast-oriented motion of the lithosphere and is in agreement with geodetic measurements. The flow pattern can explain the heat flux, the regional geology and magmatism in the Tyrrhenian basin and provides new insights into the dynamic deformation beneath back-arc basins. However, the nearly null horizontal velocities we found suggest that deformation within the Tyrrhenian region may also require the African-Eurasian plate convergence in addition to buoyancy forces to complete the picture.

4.1 Introduction

The Tyrrhenian region lies at the foot of a complex plate boundary that has been shaped by the interplay between the African and Eurasian plates which converge at a velocity of a few mm/yr (e.g., Chiarabba et al., 2015; D'Agostino et al., 2008; Nocquet, 2012; Serpelloni et al., 2005). Deformation within this plate boundary is complex and cannot be easily related to the motion of the main plates. For instance, recent seismological, geological and geodetic data points to the fact that the Adriatic microplate moves perpendicular to the motion of the African and Eurasian plates (e.g., D'Agostino et al., 2008; Nocquet, 2012) and that the crust-upper mantle structure beneath central Italy supports delamination processes and sinking of the continental lithosphere beneath the Apennine mountain belt (e.g., Aoudia et al., 2007; Chiarabba et al., 2015). Distribution of seismicity and focal mechanisms shows that deformation is mainly

dominated by extension along the Apennines from Calabria to Tuscany and shortening in Sicily and beneath the southeastern Alps.

Although external forces have been crucial in the geodynamic evolution of the Tyrrhenian region, here, we investigate the contribution of buoyancy forces to the ongoing slow and complex lithospheric deformations in the Tyrrhenian area. To this end, we model the contemporary lithosphere flow field below the Tyrrhenian region making use of a recent highly-resolved seismic velocity model (Manu-Marfo et al., 2019). We use the finite-element Pylith code and include the effect of body forces on vertical direction to compute the buoyancy driven flow due to density variation within the lithosphere. The modelled flow field can explain the magmatism and geodynamic evolution of the Tyrrhenian basin, thus suggesting that buoyancy forces contribute to the deformation in the Tyrrhenian area.

4.2 Ambient noise tomography

Knowledge of the 3D lithosphere structure below the Tyrrhenian area is essential, as it provides insight into geophysical processes such as seismicity, the modern state of stress, and unravelling past tectonic history of the region. Geophysical investigations such as seismic tomography and gravimetric studies provides a means of gaining information about the properties of the crust and upper mantle that otherwise are inaccessible for direct measurement. In this regard, the Tyrrhenian basin and surrounding margins have been studied by means of ambient noise surface wave tomography (e.g., Manu-Marfo et al., 2019).

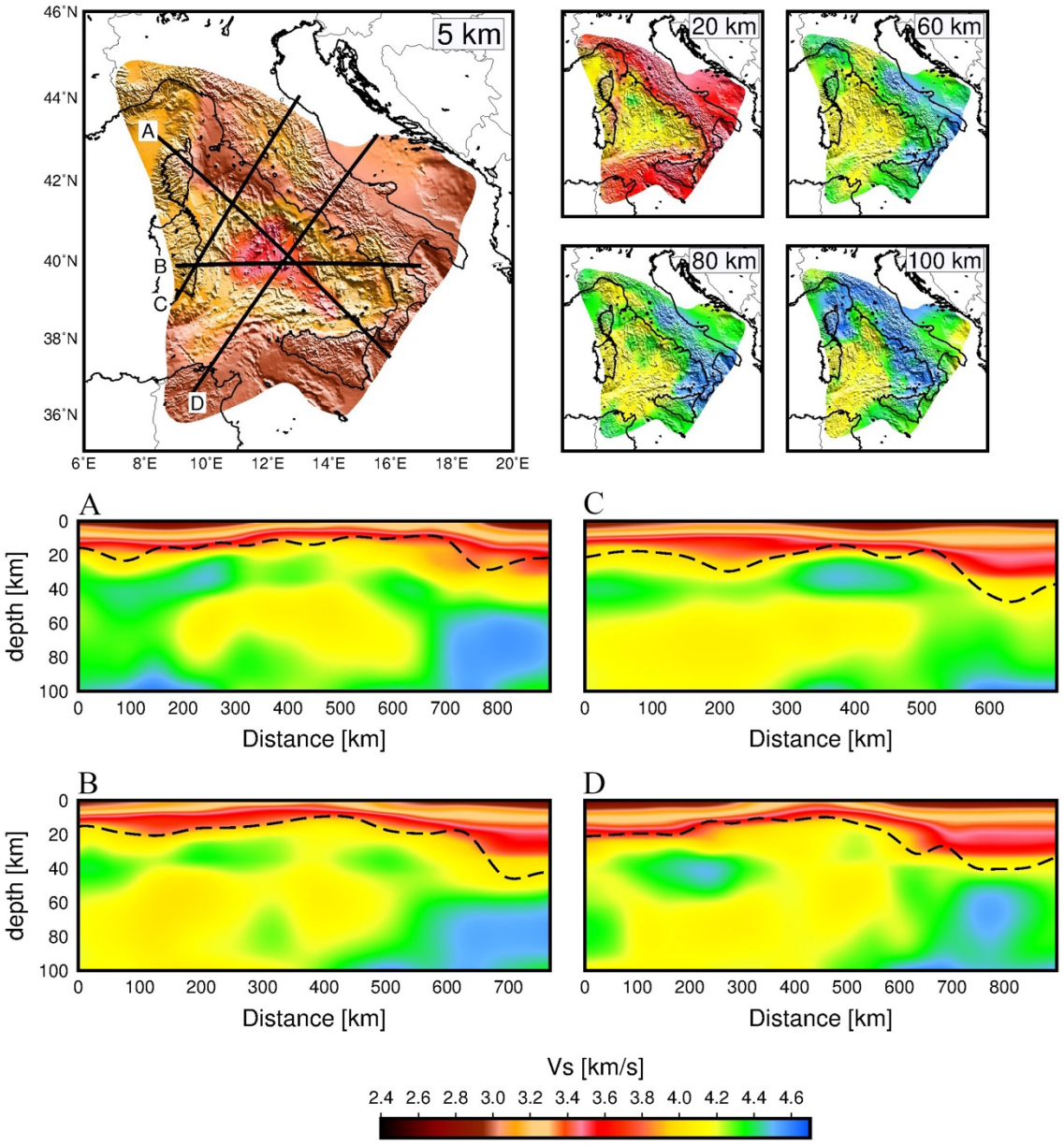

Figure 4.1 S-wave velocity model for the study area.

The Rayleigh wave dispersion curves determined from the ambient noise cross-correlation range from 5 to 50 s, sensitive to the S-wave velocity structure down to about 100 km (Manu-Marfo et al., 2019). The lateral resolution of the dispersion data is variable across the study area, with resolution deteriorating west of the study area due to few seismic stations located in that area. Estimating the S-wave velocity from the dispersion data involved a two-step inversion process. First, the dispersion data extracted from the ambient noise cross-correlation is used to produce 2D tomography maps employing the tomography technique of Yanovskaya

& Ditmar, (1990). In the second step, local dispersion curves extracted from the 2D tomography maps at each node of a 0.5° × 0.5° grid (comparable with the average resolution of the dispersion data) are inverted for the S-wave velocity-depth profiles employing a non-linear Bayesian inversion method (Dettmer & Dosso, 2012; Manu-Marfo et al., 2019; Pachhai et al., 2014, 2015). Examples of S-wave velocity models for the study area are shown in Figure 4.1.

To summarize the result (for detail see Chapter 2), the velocity model shows that the Vavilov basin is likely underlain by exhumed mantle basement rather than an oceanic basement (Figure 4.1). In the mantle, the presence of a broad low velocity zone is observed between 40 and 80 km depth affecting much of the Tyrrhenian basin uppermost mantle (Figure 4.1). The crustal thickness varies from ~10 km below the southern Tyrrhenian basin to about 55 km below Calabria and the northern Apennines (Figure 4.1).

4.3 Numerical model description and computational approach

We use lithospheric density distribution and viscosity as input for a 3D Pylith finite-element model (Aagaard et al., 2013). We use the Trelis software (www.csimsoft.com/trelis) to develop a 3D mesh with dimension 1888 × 1222 km and 200 km deep, divided into hexahedral elements with horizontal spacing of 25 km and 5 km along depth. A single Maxwell's viscoelastic material is define for both the crust and the mantle and we apply Dirichlet boundary conditions (that is, no motion across the boundary, but free boundary-parallel slip) on the sides and bottom of this domain.

In this model domain, we consider an inhomogeneous viscous flow in the presence of gravity. The flow is described by the momentum (stokes) equation

$$-\nabla P + \mathrm{div}\{\eta(\mathbf{x})e_{ij}\} + \rho(\mathbf{x})g = 0 \quad (4.1)$$

and the incompressibility condition

$$\mathrm{div}\, u = \frac{\partial u_1}{\partial x_1} + \frac{\partial u_2}{\partial x_2} + \frac{\partial u_3}{\partial x_3} = 0 \quad (4.2)$$

where P is pressure, η is viscosity, ρ is density, $\mathbf{x}$=(x_1,x_2,x_3) are the Cartesian coordinates, $\mathbf{u}$=(u_1,u_2,u_3) is the velocity, $e_{ij} = 0.5(\frac{\partial u_i}{\partial x_j} + \frac{\partial u_j}{\partial x_i})$ is the strain rate tensor, g is the acceleration due to gravity. The density $\rho(\mathbf{x})$ and viscosity $\eta(\mathbf{x})$ are prescribed according to the density and viscosity models discuss in section 4.4 below.

We compute the initial stresses from the following relation

$$\sigma_{zz} = \rho_i g h \quad (4.3)$$

where ρ_i represent the average density of each layer when the density model is parameterise into a set of layers, g is the gravitational acceleration and h is the depth of the layer. As mentioned in the Pylith 2.1.4 user manual (page 161), an initial hydrostatic stress equal to average lithostatic pressure as a function of depth is used to prevent the large initial displacement when gravity is "turned on". We specify $\rho \cdot g \cdot h$ as the initial stress state (i.e lithostatic) to all normal stress components, which is an appropriate condition for many tectonic problems in the absence of tectonic stresses. This initial condition mirrors the theoretical framework of McGarr, (1988).

We tested variations in the model geometry and rheology by defining different mesh sizes and including for example an elastic crustal material above a viscoelastic mantle. We found that these variations have negligible effects on the results.

The 2D models shown in Figure 4.2 and **Error! Reference source not found.** are identical except that the mesh size is 1200 by 200 km and the elements size is 5 × 5 km.

4.4 Results and Discussion

As mentioned in the previous section, the computation of the lithospheric flow field requires two fundamental inputs; lithospheric viscosity and density distribution. We explore the sensitivity of the lithospheric flow field by defining different inferences of lithospheric viscosity and density anomalies.

4.4.1 Effect of Viscosity

An important physical parameter in numerical modelling is viscosity, albeit it is the least well constrained property. Viscosity is responsible for strengthening or weakening Earth's rocks and also influences the stress state. Here, we considered three lithospheric viscosity profiles. We define a very simple viscosity profile for the first (V1) and second (V2) viscosity models. For model V1, we assign a viscosity of 10^{24} Pa s for the crust and a viscosity of 10^{22} Pa s for the mantle layer. Model V2 has a viscosity of 10^{23} Pa s for the crust and 10^{21} Pa s for the mantle. The viscosity model V3 is rather complex, as we prescribe the viscosity values according to the S-wave velocity model. Following Aoudia et al., (2007) and Ismail-Zadeh et al., (2010), we adopt the following values for V3: 10^{23} Pa s (upper crust), 10^{19} Pa s (lower crust), 10^{21} Pa s (lithosphere), 10^{22} Pa s (high-velocity lithosphere), and 10^{19} Pa s (low-velocity uppermost mantle).

To illustrate the influence of these differing inferences of lithospheric viscosity, we compute the lithospheric flow along a 2D profile (for computational ease) using density model D1 (discuss in section 4.4.2 below).

Figure 4.2 shows that a similar flow pattern is predicted irrespective of the viscosity profile used. For all three viscosity models considered, we observe upwelling of the mantle in the central Tyrrhenian basin and downwelling of the mantle below Calabria and Corsica. From

other test carried out (not shown here), we noticed that the flow field pattern is mostly controlled by the density heterogeneities and viscosity only affects the magnitude of the flow velocity.

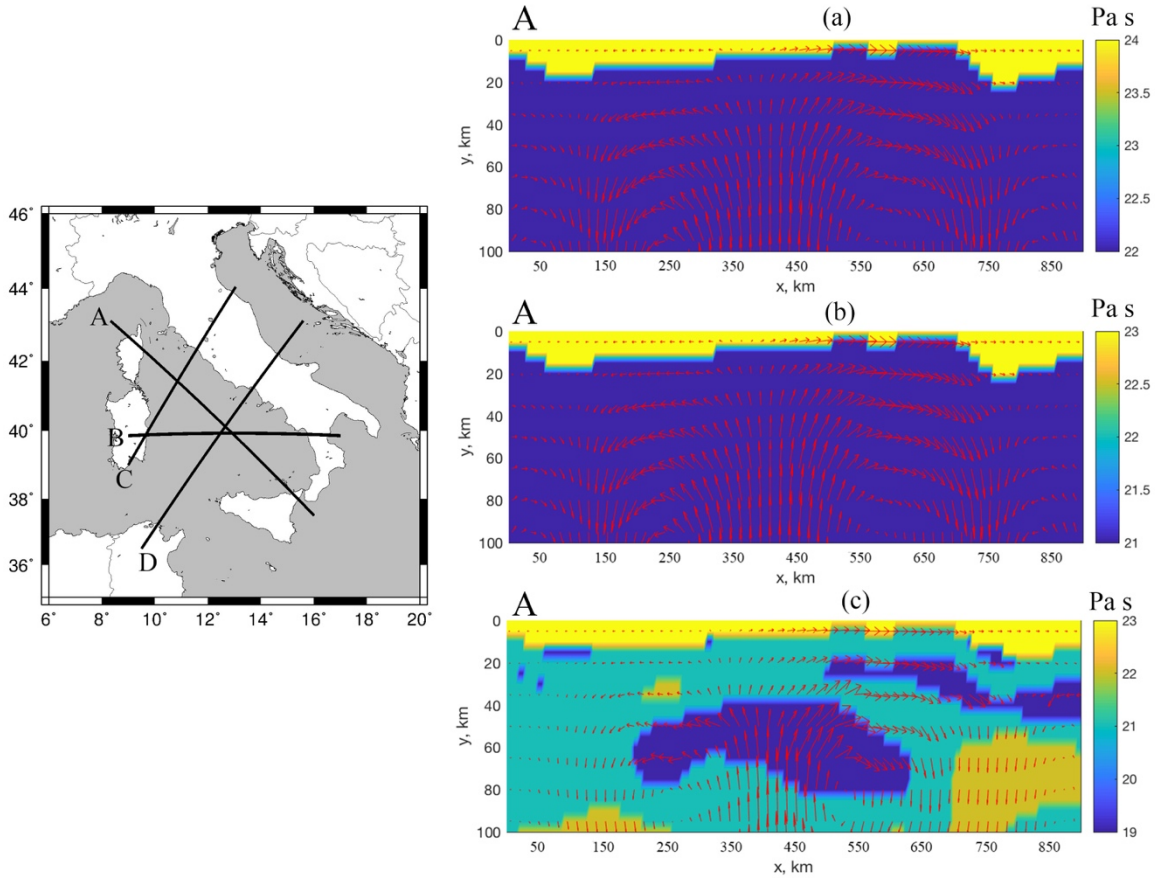

Figure 4.2 Predicted flow field along a 2D profile (cross-section A) considering different lithospheric viscosity models. Note that the magnitudes of the vectors have been scaled up for visualization.

Since, the flow orientation does not change much for the different viscosity models, we use the viscosity model V1 for all further computation of the flow field.

4.4.2 Effect of Density

Although in section 4.4.1 above, we explored the effect of using different viscosity models, we focus here on the crucially important issue of using a geodynamically consistent model of the 3D lithospheric density distribution. This is because the heterogeneity of the Earth's density structure is one of the main factors that controls geodynamics processes that shape the Earth.

However, obtaining the 3D lithospheric density distribution in a region is nontrivial, as density variation depends on many factors like temperature, pressure, and composition (both chemical and mineralogical). Here, we consider two different density models, both derived from seismic velocity models for the Tyrrhenian region (see section 4.2 above).

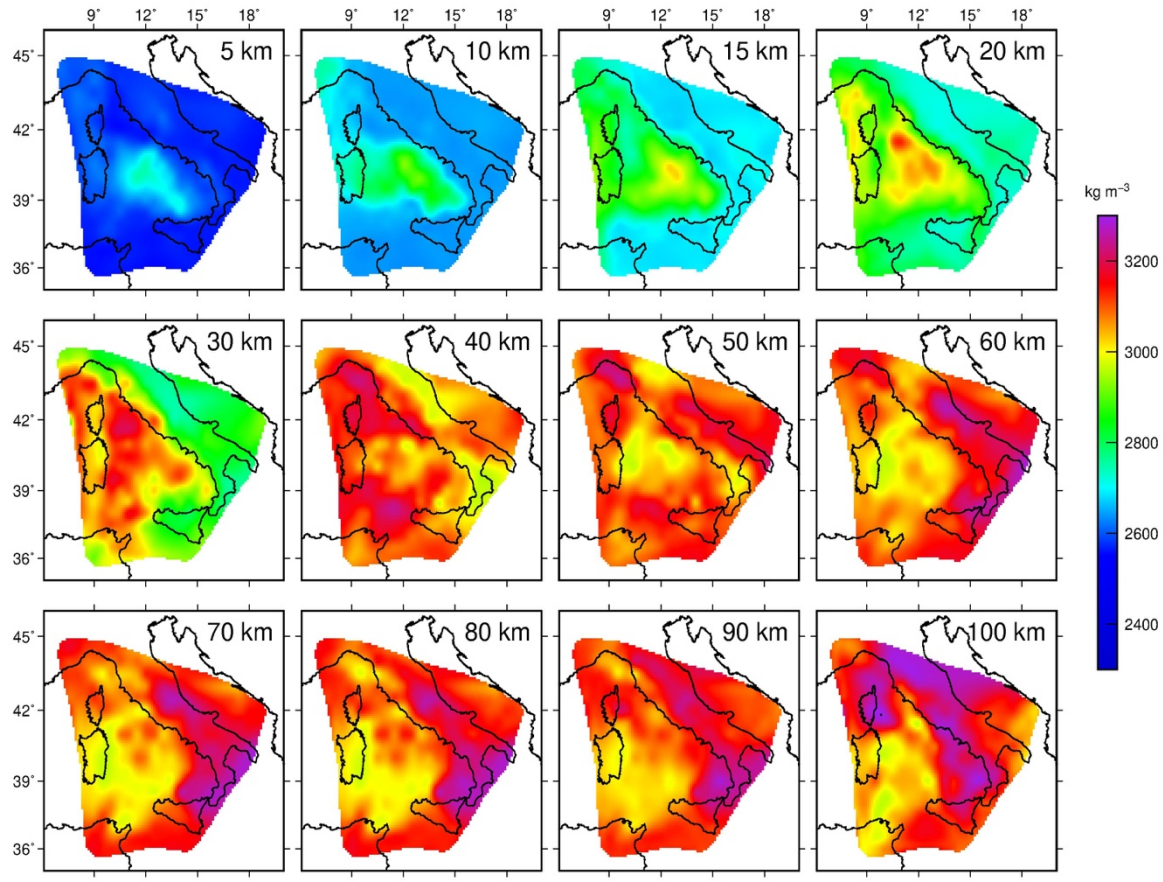

Figure 4.3 Horizontal slices of the 3D density model (D1) estimated from seismic velocity using the Nafe-Drake scaling relation (Ludwig et al., 1970).

The classical procedure for estimating the 3D lithospheric density structure from seismic velocity models is to use empirical relationship to rescale seismic velocity anomalies into equivalent density anomalies. To this end, we derive the first density model, D1 (Figure 4.3), by converting the seismic velocity model into density using the Nafe-Drake empirical relationship (Ludwig et al., 1970). The second density model, D2 (Figure 3.4) is derived by combining seismic velocity, heat flow, gravity and topography data (see chapter 3 of this thesis for details about this model).

While lithospheric density structure generally mirrors the seismic velocity anomalies, it is important that such density distribution reproduce observed gravity anomalies. To investigate how well we constrain these two lithospheric density models (D1 and D2), we compute the gravity anomalies that arise from these density models and compare them with observe Bouguer anomalies (Barzaghi et al., 2002). The result is shown in Figure 3.5 and Figure 4.4.

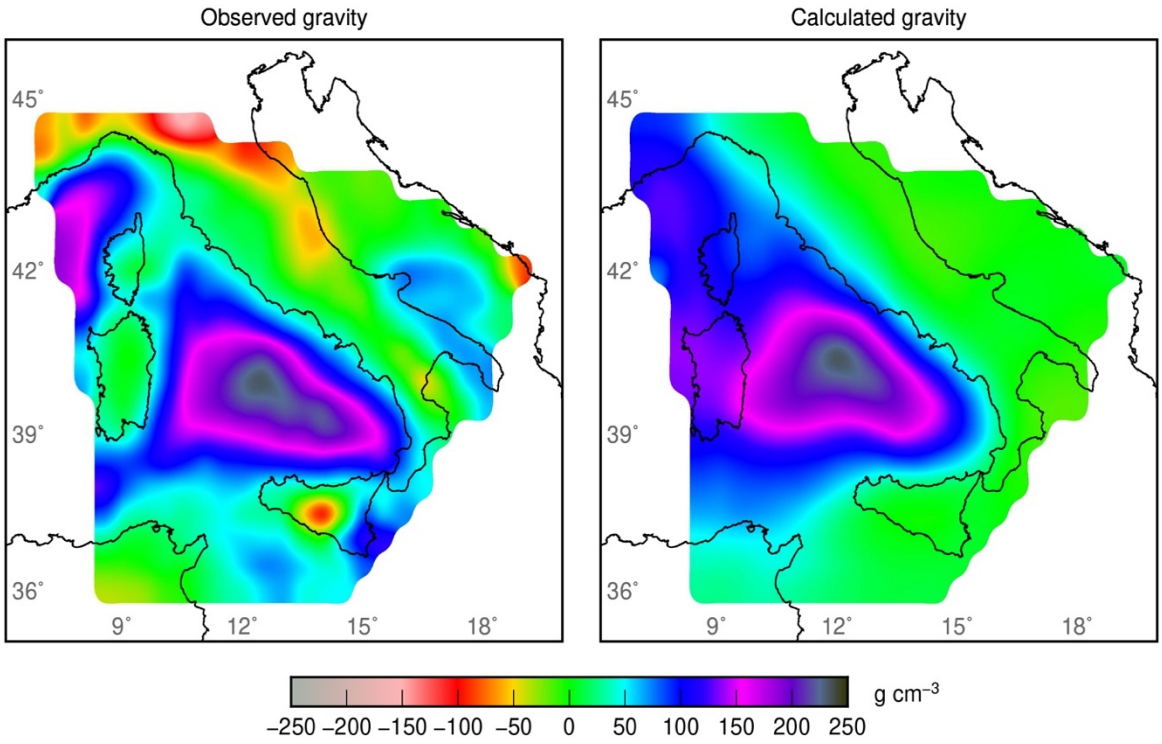

Figure 4.4 Observed Bouguer gravity anomaly vs Bouguer gravity anomaly computed from the density model D1 shown in Figure 4.3.

We show the modelled crust and mantle flow field as projections onto horizontal slices of the 3D domain (Figure 4.5 and Figure 4.6) and along 2D profiles (**Error! Reference source not found.**). Note that we only show the numerical results within the study region. In the following, we compare the predictions of the lithospheric flow based on the seismic-only derived density model D1 with those based on the joint seismic-gravity-topography derived density model D2 mentioned above.

The predicted horizontal flow field from both density models (Figure 4.5 and Figure 4.6) indicates that the lithosphere beneath the Tyrrhenian region moves predominantly towards the northeast with a maximum horizontal velocity <1.0 mm/yr. The overall direction of flow observed in both models agrees with previous studies although the maximum horizontal velocity is small in our model compared with the previous results (e.g., Ismail-Zadeh et al., 2010).

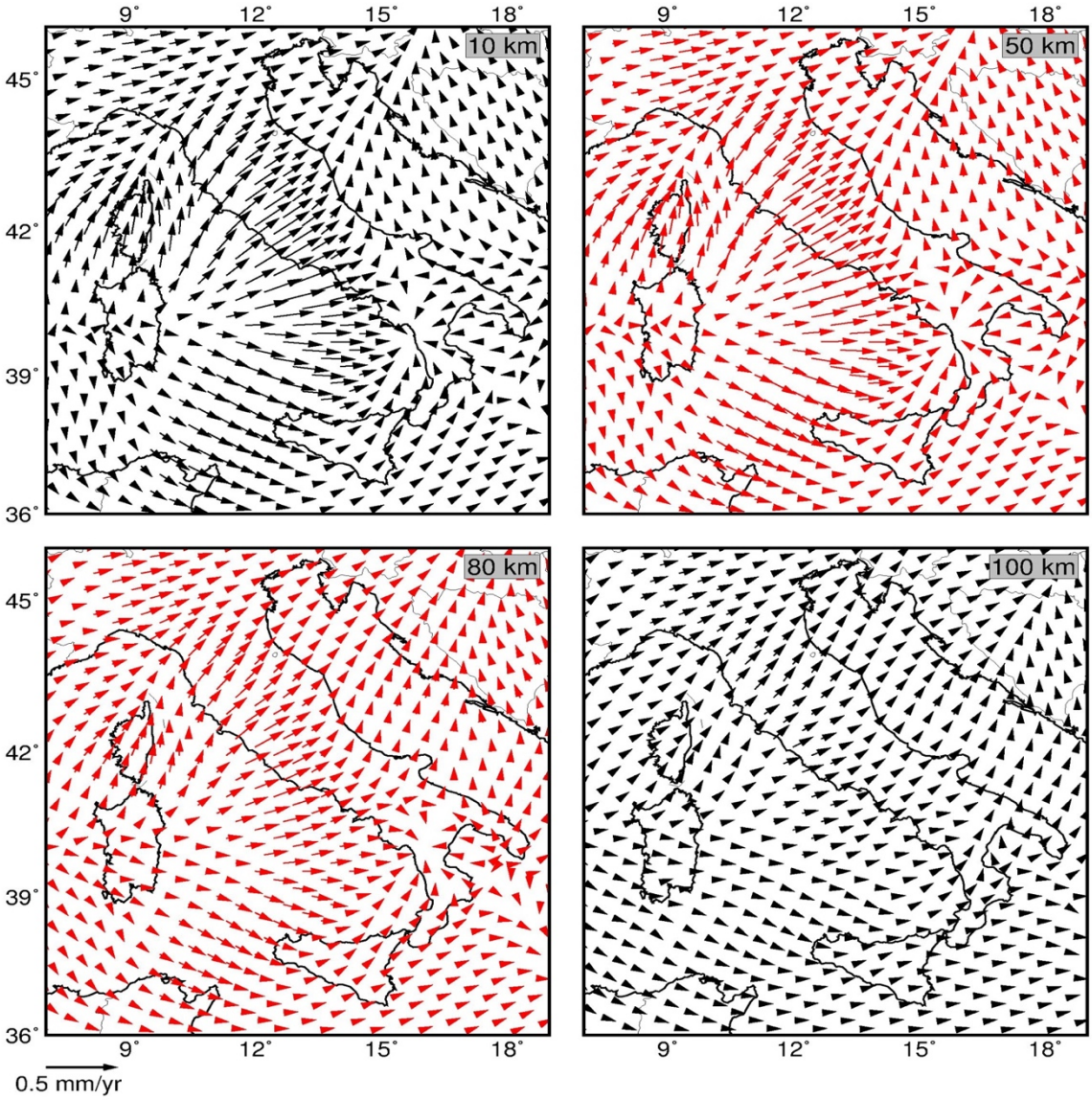

Figure 4.5 Predicted flow fields presented on horizontal slices at four different depths in the lithosphere. The lithosphere buoyancy distribution is given by model D1.

The flow field predicted from density model D1 shows a consistent pattern in both the crust and the uppermost mantle as the orientation of the flow field remains relatively constant at all the depth slices show in Figure 4.5. In contrast, the flow field predicted using density model D2 (Figure 4.6) changes orientation below 50 km depth in the central Tyrrhenian basin probably because of the differences in densities between the crust and the uppermost mantle. Although the flow orientation changes, we do not envisage lithospheric decoupling here.

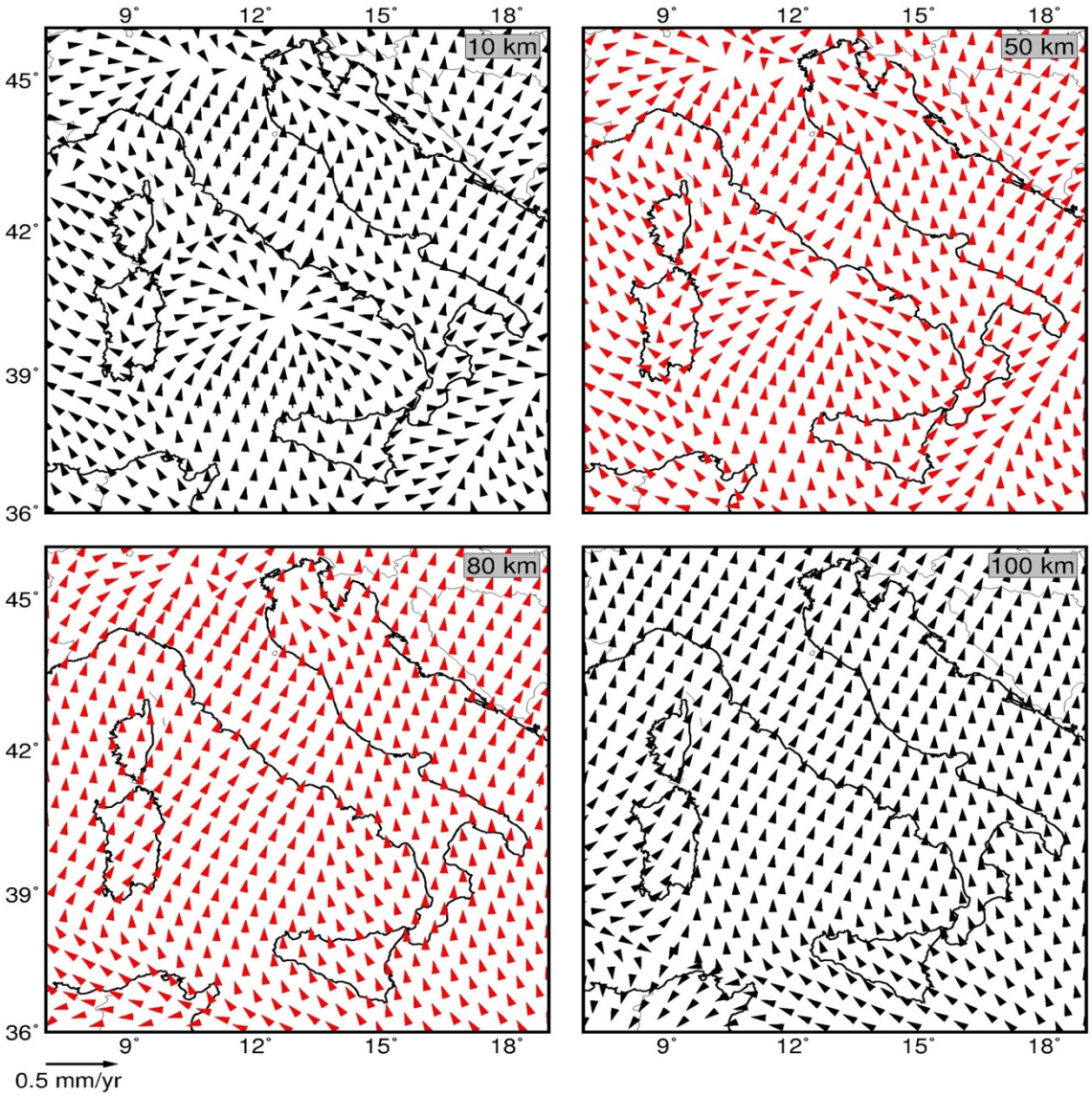

Figure 4.6 Predicted flow fields presented on horizontal slices at four different depths in the lithosphere. The lithosphere buoyancy distribution is given by model D2.

Along 2D profiles, the flow predicted by model D1 show upwelling of the mantle beneath the central Tyrrhenian basin, Sardinia and Tuscany. Downwelling of the mantle occur below the Apennines, Corsica, Sicily and the Aeolian Islands (**Error! Reference source not found.**a-d). The downwelling beneath Sicily and the Aeolian Islands is likely associated with the high-velocity slab subduction beneath the Calabrian Arc. Upwelling beneath the central Tyrrhenian basin may be associated with lithospheric extension observed in the Tyrrhenian area. Thus the observed upwelling and downwelling in **Error! Reference source not found.**a-d are very reasonable patterns of lithospheric flow and are in agreement with the structure of the Earth and the distribution of volcanic complex in the study area (Panza et al., 2004, 2007; Peccerillo, 2017b).

In contrast, the flow pattern predicted by the density model D2 show downwelling below the central Tyrrhenian basin and upwelling below Sicily and the Aeolian arc (**Error! Reference source not found.**e-h). The reversal of the flow field in the central Tyrrhenian basin corresponds to the presence of an anomalous high-density uppermost mantle beneath the southern Tyrrhenian basin (Figure 3.4).

The downwelling of the lithosphere beneath the central Tyrrhenian basin predicted by the density model D2 appears to contradict the general understanding of mantle uprooting below the Tyrrhenian basin. However, considering that recent seismic tomographic studies have shown a relatively high-velocity mantle beneath the central Tyrrhenian (e.g., Greve et al., 2014; Marone et al., 2004), this lithospheric flow pattern may correspond to the contemporary flow of the lithosphere in the southern Tyrrhenian basin. Although the southern Tyrrhenian basin opened as a result of backarc extension, Serpelloni et al., (2005) have shown that data from GPS stations located in the Tyrrhenian area show no significant elongation, suggesting that

backarc extension, which characterised the evolution of the Tyrrhenian region (Faccenna et al., 2001; Malinverno & Ryan, 1986) is no longer active.

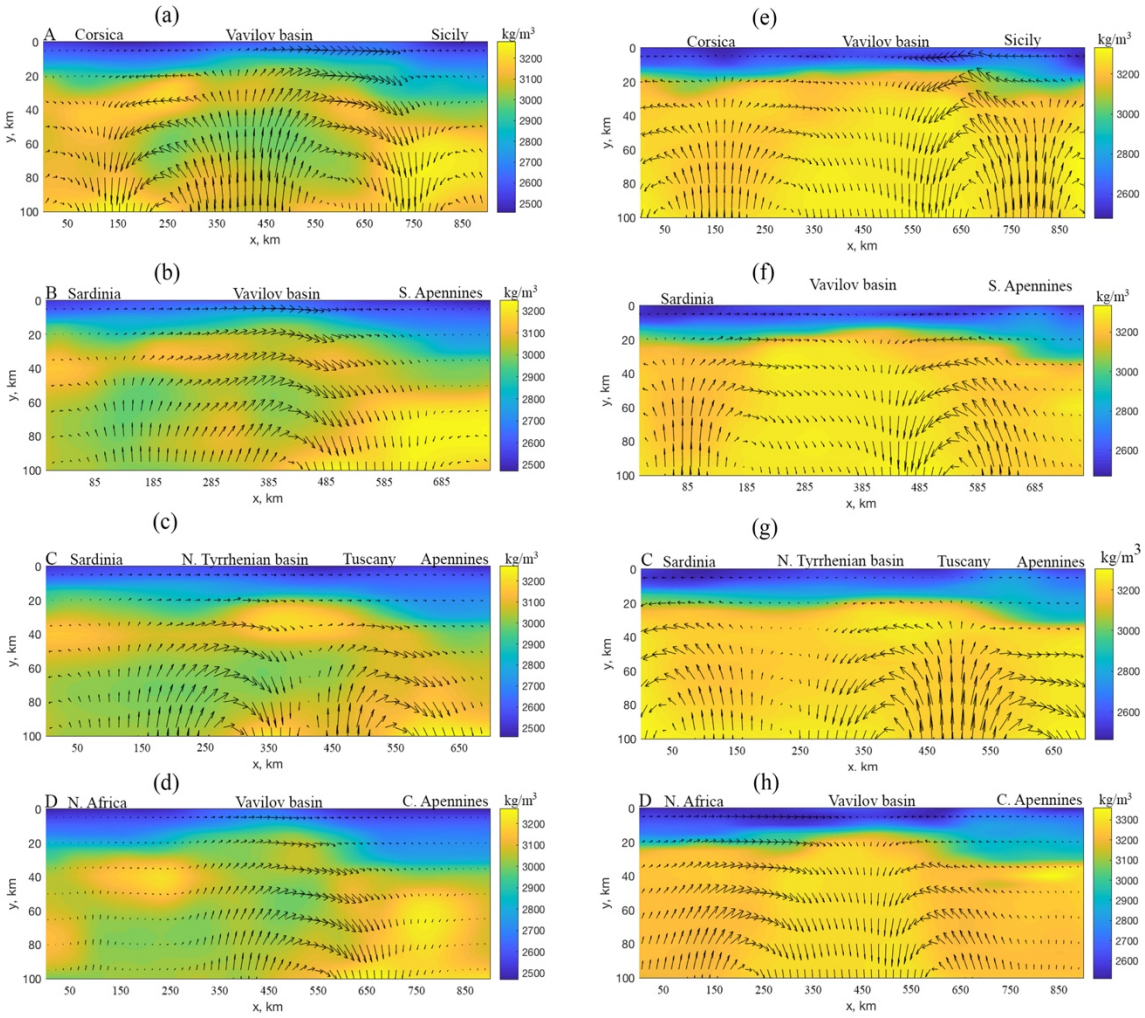

Figure 4.7 Predicted flow fields along 2D profiles form density model D1 (left panel) and D2 (right panel). The location of the cross-sections are shown in Figure 4.2. Note that the magnitudes of the vectors have been scaled up for visualization.

Overall, the flow field predicted based on the density model D1 show consistent results that agrees with the overall geodynamics evolution of the study area and so we select this model as the final result.

4.5 Conclusion

We modelled the flow field below the Tyrrhenian region using as input lithospheric viscosity and density models. Our 3D models using different density inferences highlights that the

lithosphere beneath the Tyrrhenian region moves predominantly northeast. On the 2D model, observed upwelling and downwelling agrees with the geodynamic evolution of the study area, suggesting that buoyancy forces, which result from heterogenous density distribution in the crust and uppermost mantle, can explain principal features of the present-day deformation, regional tectonics and magmatism within the Tyrrhenian area.

Conclusions

We have obtained a high-resolution shear-wave velocity structure of the crust and uppermost mantle beneath the Tyrrhenian basin. Our result suggests the presence of a shallow exhumed mantle basement below the Vavilov-Magnaghi basin contrarily to previously suggested oceanic crust. Our velocity model of the crust, however, agrees with previous studies suggesting a thin continental crust beneath the northern Tyrrhenian basin. In the uppermost mantle, the most prominent feature is the presence of a low-velocity zone that affects much of Tyrrhenian basin between 40 and 80 km and whose lateral extent mimics the paleogeographic evolution of the Calabrian arc in time. We infer that this low-velocity zone is due to mantle water content variation and decompressional melt and may well be the source of the complex and variable volcanism found in the Tyrrhenian area.

However, comparing our results to those of other backarc basins, we find notable similarities and differences. Using local events, Wiens et al., (2006) determined the average shear-wave velocity structure of four backarc basin by waveform modelling. The 1D velocity-depth models for all four basins show a low-velocity zone with a minimum shear-wave velocity at approximately 80 km with minimum values varying from 3.85 (Lau Basin) to 4.15 km/s (Mariana Trough). The authors attributed the variation in the seismic velocity structure between the four basins to variations in mantle potential temperature as the increase in minimum velocity from Lau to Fiji to Scotia to Marianas correlates well with increasing mantle temperatures inferred from petrology and basin depth. To explain the inter-basin velocity variations, Wiens et al., (2006) ruled out variations in water content because the petrologically inferred water contents increase, rather than decrease, with increasing minimum shear velocity. Thus, although both temperature and water content may contribute to the velocity structure

below the four backarc basins investigated by Wiens et al., (2006), variations in temperature dominate the differences between them.

In the case of the Tyrrhenian basin, the minimum S-wave velocity observed in the uppermost mantle is about 4.0 km/s and we associate this velocity decrease to a combined effect of water content, temperature and decompressional melt, but here, we favour water content variation as the dominant effect. Water in the Tyrrhenian mantle comes from the slab subducting beneath the Calabrian Arc, whose evolution in time is likely responsible for the observed low-velocity zone below the Tyrrhenian. Comparing minimum shear velocity values, the Tyrrhenian shear-wave velocities are most similar to those observed below the Marianas. From Wiens et al., (2006), the background temperature for the Mariana Trough is inferred to be close to normal MORB-source potential temperature whereas the other backarc basins (Scotia, Fiji, and Lau) were found to be relatively hot. Based on the similar shear-wave velocity observed in the Tyrrhenian and the Mariana, we infer that the mantle potential temperature below the Tyrrhenian basin is likely close to a normal MORB-source potential temperature and may not be the leading factor for the minimum shear-wave velocities observed in the Tyrrhenian.

Further, we derived the 3D density structure of the lithosphere beneath the Tyrrhenian region combining seismic velocity, surface heat flow, gravity and topography. Our final density model shows a pronounced ring-shape low-density uppermost mantle surrounding the southern Tyrrhenian basin which is underlain by a high-density uppermost mantle. The absence of a low-density anomaly beneath the southern Tyrrhenian basin does not agree with the hypothesis that the opening of the southern Tyrrhenian basin was as a result of an ascending low-density asthenospheric material.

Finally, we use lithospheric viscosity and density models to compute the contemporary lithospheric flow fields beneath the Tyrrhenian basin and surrounding areas. The orientation of

the flow fields found in this study agrees with the general northeast movement of the lithosphere in the Tyrrhenian region, suggesting that buoyancy forces, which result from heterogenous density distribution in the crust and uppermost mantle, can explain principal features of the present-day deformation, regional tectonics and magmatism within the Tyrrhenian area.

Our overall results of the lithospheric structure beneath the Tyrrhenian basin and surrounding margins can explain the heat flux, the regional geology and magmatism in the Tyrrhenian basin and provides new insights into the dynamic deformation beneath the backarc basin.

Bibliography

Aagaard, B. T., Knepley, M. G., & Williams, C. A. (2013). A domain decomposition approach to implementing fault slip in finite-element models of quasi-static and dynamic crustal deformation. *Journal of Geophysical Research: Solid Earth*, *118*(6), 3059–3079. https://doi.org/10.1002/jgrb.50217

Afonso, J. C., Fullea, J., Griffin, W. L., Yang, Y., Jones, A. G., D. Connolly, J. A., & O'Reilly, S. Y. (2013). 3-D multiobservable probabilistic inversion for the compositional and thermal structure of the lithosphere and upper mantle. I: a priori petrological information and geophysical observables. *Journal of Geophysical Research: Solid Earth*, *118*(5), 2586–2617. https://doi.org/10.1002/jgrb.50124

Aoudia, A., Ismail-Zadeh, A. T., & Romanelli, F. (2007). Buoyancy-driven deformation and contemporary tectonic stress in the lithosphere beneath Central Italy. *Terra Nova*, *19*(6), 490–495. https://doi.org/10.1111/j.1365-3121.2007.00776.x

Backus, G., & Gilbert, F. (1968). The Resolving Power of Gross Earth Data. *Geophysical Journal International*, *16*(2), 169–205. https://doi.org/10.1111/j.1365-246X.1968.tb00216.x

Bartole, R. (1995). The North Tyrrhenian-Northern Apennines post-collisional System : Constraints for a Geodynamic Model. *Terra Nova*, *7*(1), 7–30.

Barzaghi, R., Betti, B., Borghi, A., Sona, G., & Tornatore, V. (2002). The Italian quasi-geoid ITALGEO99. *Bollettino Di Geodesia e Scienze Affini*, *61*(1), 33–51.

Behn, M. D., & Kelemen, P. B. (2003). Relationship between seismic P-wave velocity and the composition of anhydrous igneous and meta-igneous rocks. *Geochemistry, Geophysics, Geosystems*, *4*(5), n/a-n/a. https://doi.org/10.1029/2002GC000393

Bell, K., Lavecchia, G., & Rosatelli, G. (2013). Cenozoic Italian magmatism – Isotope constraints for possible plume-related activity. *Journal of South American Earth Sciences*, *41*, 22–40. https://doi.org/10.1016/j.jsames.2012.10.005

Bell, Keith, Castorina, F., Lavecchia, G., Rosatelli, G., & Stoppa, F. (2004). Is there a mantle plume below Italy? *Eos, Transactions American Geophysical Union*, *85*(50), 541. https://doi.org/10.1029/2004EO500002

Bensen, G. D., Ritzwoller, M. H., Barmin, M. P., Levshin, A. L., Lin, F., Moschetti, M. P., … Yang, Y. (2007). Processing seismic ambient noise data to obtain reliable broad-band surface wave dispersion measurements. *Geophysical Journal International*, *169*(3), 1239–1260. https://doi.org/10.1111/j.1365-246X.2007.03374.x

Bensen, G. D., Ritzwoller, M. H., & Shapiro, N. M. (2008). Broadband ambient noise surface wave tomography across the United States. *Journal of Geophysical Research*, *113*(B5), B05306. https://doi.org/10.1029/2007JB005248

Billi, A., Barberi, G., Faccenna, C., Neri, G., Pepe, F., & Sulli, A. (2006). Tectonics and seismicity of the Tindari Fault System, southern Italy: Crustal deformations at the

transition between ongoing contractional and extensional domains located above the edge of a subducting slab. *Tectonics*, *25*(2), n/a-n/a. https://doi.org/10.1029/2004TC001763

Boccaletti, M., Nicolich, R., & Tortorici, L. (1990). New data and hypothesis on the development of the Tyrrhenian basin. *Palaeogeography, Palaeoclimatology, Palaeoecology*, *77*(1), 15–40. https://doi.org/10.1016/0031-0182(90)90096-P

Bodin, T., Sambridge, M., Rawlinson, N., & Arroucau, P. (2012). Transdimensional tomography with unknown data noise. *Geophysical Journal International*, *189*(3), 1536–1556. https://doi.org/10.1111/j.1365-246X.2012.05414.x

Brocher, T. M. (2005). Empirical Relations between Elastic Wavespeeds and Density in the Earth's Crust. *Bulletin of the Seismological Society of America*, *95*(6), 2081–2092. https://doi.org/10.1785/0120050077

Bruno, P. P., Di Fiore, V., & Ventura, G. (2000). Seismic study of the '41st Parallel' Fault System offshore the Campanian–Latial continental margin, Italy. *Tectonophysics*, *324*(1–2), 37–55. https://doi.org/10.1016/S0040-1951(00)00114-1

Burdick, L. J., & Langston, C. a. (1977). Modeling crustal structure through the use of converted phases in teleseismic body-wave forms. *Bulletin of the Seismological Society of America*, *67*(3), 677–691. Retrieved from http://www.bssaonline.org/content/67/3/677.abstract

Carafa, M. M. C., Kastelic, V., Bird, P., Maesano, F. E., & Valensise, G. (2018). A "Geodetic Gap" in the Calabrian Arc: Evidence for a Locked Subduction Megathrust? *Geophysical Research Letters*, *45*(4), 1794–1804. https://doi.org/10.1002/2017GL076554

Carminati, E., & Doglioni, C. (2005). EUROPE | Mediterranean Tectonics. *Encyclopedia of Geology*, 135–146. https://doi.org/10.1016/b0-12-369396-9/00135-0

Channell, J., Dargenio, B., & Horvath, F. (1979). Adria, the African promontory, in mesozoic Mediterranean palaeogeography. *Earth-Science Reviews*, *15*(3), 213–292. https://doi.org/10.1016/0012-8252(79)90083-7

Chiarabba, C., De Gori, P., & Mele, F. M. (2015). Recent seismicity of Italy: Active tectonics of the central Mediterranean region and seismicity rate changes after the Mw 6.3 L'Aquila earthquake. *Tectonophysics*, *638*(1), 82–93. https://doi.org/10.1016/j.tecto.2014.10.016

Chiarabba, C., De Gori, P., & Speranza, F. (2008). The southern Tyrrhenian subduction zone: Deep geometry, magmatism and Plio-Pleistocene evolution. *Earth and Planetary Science Letters*, *268*(3–4), 408–423. https://doi.org/10.1016/j.epsl.2008.01.036

Chiarabba, C., & Palano, M. (2017). Progressive migration of slab break-off along the southern Tyrrhenian plate boundary: Constraints for the present day kinematics. *Journal of Geodynamics*, *105*, 51–61. https://doi.org/10.1016/j.jog.2017.01.006

Christensen, N. I. (1996). Poisson's ratio and crustal seismology. *Journal of Geophysical Research: Solid Earth*, *101*(B2), 3139–3156. https://doi.org/10.1029/95JB03446

Christensen, N. I. (2004). Serpentinites, Peridotites, and Seismology. *International Geology Review*, *46*(9), 795–816. https://doi.org/10.2747/0020-6814.46.9.795

Christensen, N. I., & Mooney, W. D. (1995). Seismic velocity structure and composition of the continental crust: A global view. *Journal of Geophysical Research: Solid Earth*, *100*(B6), 9761–9788. https://doi.org/10.1029/95JB00259

Cocchi, L., Caratori Tontini, F., Muccini, F., Marani, M. P., Bortoluzzi, G., & Carmisciano, C. (2009). Chronology of the transition from a spreading ridge to an accretional seamount in the Marsili backarc basin (Tyrrhenian Sea). *Terra Nova*, *21*(5), 369–374. https://doi.org/10.1111/j.1365-3121.2009.00891.x

Cocchi, L., Masetti, G., Muccini, F., & Carmisciano, C. (2016). Geophysical mapping of Vercelli Seamount: Implications for Miocene evolution of the Tyrrhenian back arc basin. *Geoscience Frontiers*, *7*(5), 835–849. https://doi.org/10.1016/j.gsf.2015.06.006

Conti, A., Bigi, S., Cuffaro, M., Doglioni, C., Scrocca, D., Muccini, F., … Bortoluzzi, G. (2017). Transfer zones in an oblique back-arc basin setting: Insights from the Latium-Campania segmented margin (Tyrrhenian Sea). *Tectonics*, *36*(1), 78–107. https://doi.org/10.1002/2016TC004198

Contrucci, I., Mauffret, A., Brunet, C., Nercessian, A., Béthoux, N., & Ferrandini, J. (2005). Deep structure of the North Tyrrhenian Sea from multi-channel seismic profiles and on land wide angle reflection/refraction seismic recording (LISA cruise): Geodynamical implications. *Tectonophysics*, *406*(3–4), 141–163. https://doi.org/10.1016/j.tecto.2005.05.015

D'Agostino, N., Avallone, A., Cheloni, D., D'Anastasio, E., Mantenuto, S., & Selvaggi, G. (2008). Active tectonics of the Adriatic region from GPS and earthquake slip vectors. *Journal of Geophysical Research: Solid Earth*, *113*(12), 1–19. https://doi.org/10.1029/2008JB005860

Della Vedova, B., Pellis, G., Foucher, J. ., & Rehault, J.-P. (1984). Geothermal structure of the Tyrrhenian Sea. *Marine Geology*, *55*(3–4), 271–289. https://doi.org/10.1016/0025-3227(84)90072-0

Deng, Y., Levandowski, W., & Kusky, T. (2017). Lithospheric density structure beneath the Tarim basin and surroundings, northwestern China, from the joint inversion of gravity and topography. *Earth and Planetary Science Letters*, *460*, 244–254. https://doi.org/10.1016/j.epsl.2016.10.051

Dercourt, J., Zonenshain, L. P., Ricou, L.-E., Kazmin, V. G., Le Pichon, X., Knipper, A. L., … Biju-Duval, B. (1986). Geological evolution of the tethys belt from the atlantic to the pamirs since the LIAS. *Tectonophysics*, *123*(1–4), 241–315. https://doi.org/10.1016/0040-1951(86)90199-X

Deschamps, F., & Trampert, J. (2003). Mantle tomography and its relation to temperature and composition. *Physics of the Earth and Planetary Interiors*, *140*(4), 277–291. https://doi.org/10.1016/j.pepi.2003.09.004

Dettmer, J., & Dosso, S. E. (2012). Trans-dimensional matched-field geoacoustic inversion with hierarchical error models and interacting Markov chains. *The Journal of the Acoustical Society of America*, *132*(4), 2239–2250. https://doi.org/10.1121/1.4746016

Dettmer, J., Molnar, S., Steininger, G., Dosso, S. E., & Cassidy, J. F. (2012). Trans-

dimensional inversion of microtremor array dispersion data with hierarchical autoregressive error models. *Geophysical Journal International*, *188*(2), 719–734. https://doi.org/10.1111/j.1365-246X.2011.05302.x

Dewey, J. F. (1988). Extensional collapse of orogens. *Tectonics*, *7*(6), 1123–1139. https://doi.org/10.1029/TC007i006p01123

Dewey, J. F., Helman, M. L., Knott, S. D., Turco, E., & Hutton, D. H. W. (1989). Kinematics of the western Mediterranean. *Geological Society, London, Special Publications*, *45*(1), 265–283. https://doi.org/10.1144/GSL.SP.1989.045.01.15

Di Stefano, R., Bianchi, I., Ciaccio, M. G., Carrara, G., & Kissling, E. (2011). Three-dimensional Moho topography in Italy: New constraints from receiver functions and controlled source seismology. *Geochemistry, Geophysics, Geosystems*, *12*(9), 1–15. https://doi.org/10.1029/2011GC003649

Di Stefano, R., Chiarabba, C., Lucente, F., & Amato, A. (1999). Crustal and uppermost mantle structure in Italy from the inversion of P -wave arrival times : geodynamic implications. *Geophysical Journal International*, *139*, 483–498.

Di Stefano, R., Kissling, E., Chiarabba, C., Amato, A., & Giardini, D. (2009). Shallow subduction beneath Italy: Three-dimensional images of the Adriatic-European-Tyrrhenian lithosphere system based on high-quality P wave arrival times. *Journal of Geophysical Research: Solid Earth*, *114*(5), 1–17. https://doi.org/10.1029/2008JB005641

Duschenes, J., Sinha, M. C., & Louden, K. E. (1986). A seismic refraction experiment in the Tyrrhenian Sea. *Geophysical Journal of the Royal Astronomical Society*, *85*(1), 139–160. https://doi.org/10.1111/j.1365-246X.1986.tb05175.x

Faccenna, C., Becker, T. W., Auer, L., Billi, A., Boschi, L., Brun, J. P., … Serpelloni, E. (2014). Mantle dynamics in the Mediterranean. *Reviews of Geophysics*, *52*(3), 283–332. https://doi.org/10.1002/2013RG000444

Faccenna, C., Becker, T. W., Lucente, F. P., Jolivet, L., & Rossetti, F. (2001). History of subduction and back-arc extension in the Central Mediterranean. *Geophysical Journal International*, *145*(3), 809–820. https://doi.org/10.1046/j.0956-540x.2001.01435.x

Faccenna, C., Funiciello, F., Civetta, L., Antonio, M. D., Moroni, M., & Piromallo, C. (2007). Slab disruption, mantle circulation, and the opening of the Tyrrhenian basins. *Geological Society of America, Special Paper*, *418*(08), 153–169. https://doi.org/10.1130/2007.2418(08).

Faccenna, C., Mattei, M., Funiciello, R., & Jolivet, L. (1997). Styles of back-arc extension in the Central Mediterranean. *Terra Nova*, *9*(3), 126–130. https://doi.org/10.1046/j.1365-3121.1997.d01-12.x

Gailler, A., Klingelhoefer, F., Olivet, J. L., & Aslanian, D. (2009). Crustal structure of a young margin pair: New results across the Liguro-Provencal Basin from wide-angle seismic tomography. *Earth and Planetary Science Letters*, *286*(1–2), 333–345. https://doi.org/10.1016/j.epsl.2009.07.001

Gattacceca, J., Deino, A., Rizzo, R., Jones, D. S., Henry, B., Beaudoin, B., & Vadeboin, F.

(2007). Miocene rotation of Sardinia: New paleomagnetic and geochronological constraints and geodynamic implications. *Earth and Planetary Science Letters*, *258*(3–4), 359–377. https://doi.org/10.1016/j.epsl.2007.02.003

Giacomuzzi, G., Civalleri, M., De Gori, P., & Chiarabba, C. (2012). A 3D Vs model of the upper mantle beneath Italy: Insight on the geodynamics of central Mediterranean. *Earth and Planetary Science Letters*, *335–336*, 105–120. https://doi.org/10.1016/j.epsl.2012.05.004

Godey, S., Deschamps, F., Trampert, J., & Snieder, R. (2004). Thermal and compositional anomalies beneath the North American continent. *Journal of Geophysical Research: Solid Earth*, *109*(B1). https://doi.org/10.1029/2002JB002263

Govers, R., & Wortel, M. J. R. (2005). Lithosphere tearing at STEP faults: response to edges of subduction zones. *Earth and Planetary Science Letters*, *236*(1–2), 505–523. https://doi.org/10.1016/j.epsl.2005.03.022

Greve, S., Paulssen, H., Goes, S., & van Bergen, M. (2014). Shear-velocity structure of the Tyrrhenian Sea: Tectonics, volcanism and mantle (de)hydration of a back-arc basin. *Earth and Planetary Science Letters*, *400*, 45–53. https://doi.org/10.1016/j.epsl.2014.05.028

Guidarelli, M., & Aoudia, A. (2016). Ambient noise tomography of the Cameroon Volcanic Line and Northern Congo craton: New constraints on the structure of the lithosphere. *Geophysical Journal International*, *204*(3), 1756–1765. https://doi.org/10.1093/gji/ggv561

Hacker, B. R., & Abers, G. A. (2004). Subduction Factory 3: An Excel worksheet and macro for calculating the densities, seismic wave speeds, and H 2 O contents of minerals and rocks at pressure and temperature. *Geochemistry, Geophysics, Geosystems*, *5*(1), n/a-n/a. https://doi.org/10.1029/2003GC000614

Hammond, W. C., & Humphreys, E. D. (2000). Upper mantle seismic wave attenuation: Effects of realistic partial melt distribution. *Journal of Geophysical Research: Solid Earth*, *105*(B5), 10987–10999. https://doi.org/10.1029/2000JB900042

Handy, M. R., M. Schmid, S., Bousquet, R., Kissling, E., & Bernoulli, D. (2010). Reconciling plate-tectonic reconstructions of Alpine Tethys with the geological–geophysical record of spreading and subduction in the Alps. *Earth-Science Reviews*, *102*(3–4), 121–158. https://doi.org/10.1016/j.earscirev.2010.06.002

Hasterok, D., & Chapman, D. S. (2007). Continental thermal isostasy: 2. Application to North America. *Journal of Geophysical Research*, *112*(B6), B06415. https://doi.org/10.1029/2006JB004664

Herrmann, R. B. (2013). Computer Programs in Seismology: An Evolving Tool for Instruction and Research. *Seismological Research Letters*, *84*(6), 1081–1088. https://doi.org/10.1785/0220110096

Humphreys, E. D., & Dueker, K. G. (1994). Physical state of the western U.S. upper mantle. *Journal of Geophysical Research: Solid Earth*, *99*(B5), 9635–9650. https://doi.org/10.1029/93JB02640

Ismail-Zadeh, A., Aoudia, A., & Panza, G. F. (2010). Three-dimensional numerical modeling of contemporary mantle flow and tectonic stress beneath the Central Mediterranean. *Tectonophysics*, *482*(1–4), 226–236. https://doi.org/10.1016/j.tecto.2009.07.013

Jolivet, L., Daniel, J. M., Truffert, C., & Goffé, B. (1994). Exhumation of deep crustal metamorphic rocks and crustal extension in arc and back-arc regions. *Lithos*, *33*(1–3), 3–30. https://doi.org/10.1016/0024-4937(94)90051-5

Jolivet, L., & Faccenna, C. (2000). Mediterranean extension and the Africa-Eurasia collision. *Tectonics*, *19*(6), 1095–1106. https://doi.org/10.1029/2000TC900018

Kaban, M. K., Chen, B., Tesauro, M., Petrunin, A. G., El Khrepy, S., & Al-Arifi, N. (2018). Reconsidering Effective Elastic Thickness Estimates by Incorporating the Effect of Sediments: A Case Study for Europe. *Geophysical Research Letters*, *45*(18), 9523–9532. https://doi.org/10.1029/2018GL079732

Kastens, K., & Mascle, J. (1990). The Geological Evolution of the Tyrrhenian Sea: An Introduction to the Scientific Results of ODP Leg 107. In *Proceedings of the Ocean Drilling Program, 107 Scientific Results* (Vol. 107, pp. 3–26). Ocean Drilling Program. https://doi.org/10.2973/odp.proc.sr.107.187.1990

Kastens, Kim, Mascle, J., Auroux, C., Bonatti, E., Broglia, C., Channell, J., … Torii, M. (1988). ODP Leg 107 in the Tyrrhenian Sea: Insights into passive margin and back-arc basin evolution. *Bulletin of the Geological Society of America*, *100*(7), 1140–1156. https://doi.org/10.1130/0016-7606(1988)100<1140:OLITTS>2.3.CO;2

Lachenbruch, A. H., & Morgan, P. (1990). Continental extension, magmatism and elevation; formal relations and rules of thumb. *Tectonophysics*, *174*(1–2), 39–62. https://doi.org/10.1016/0040-1951(90)90383-J

Langston, C. A. (1979). Structure under Mount Rainier, Washington, inferreLangston, C. A. (1979), Structure under Mount Rainier, Washington, inferred from teleseismic body waves, J. Geophys. Res., 84(B9), 4749, doi:10.1029/JB084iB09p04749.d from teleseismic body waves. *Journal of Geophysical Research*, *84*(B9), 4749. https://doi.org/10.1029/JB084iB09p04749

Levandowski, W., Boyd, O. S., Briggs, R. W., & Gold, R. D. (2015). A random-walk algorithm for modeling lithospheric density and the role of body forces in the evolution of the Midcontinent Rift. *Geochemistry, Geophysics, Geosystems*, *16*(12), 4084–4107. https://doi.org/10.1002/2015GC005961

Levandowski, W., Jones, C. H., Reeg, H., Frassetto, A., Gilbert, H., Zandt, G., & Owens, T. J. (2013). Seismological estimates of means of isostatic support of the Sierra Nevada. *Geosphere*, *9*(6), 1552–1561. https://doi.org/10.1130/GES00905.1

Li, C., Zhang, G., Wang, X., Wang, Z., & Fang, J. (2014). Three-dimensional lithospheric density distribution of China and surrounding regions. *Geoscience Frontiers*, *5*(1), 95–102. https://doi.org/10.1016/j.gsf.2013.03.004

Li, H., Bernardi, F., & Michelini, A. (2010). Surface wave dispersion measurements from ambient seismic noise analysis in Italy. *Geophysical Journal International*, *180*(3), 1242–

1252. https://doi.org/10.1111/j.1365-246X.2009.04476.x

Lippitsch, R. (2003). Upper mantle structure beneath the Alpine orogen from high-resolution teleseismic tomography. *Journal of Geophysical Research*, *108*(B8), 2376. https://doi.org/10.1029/2002JB002016

Locardi, E., & Nicolich, R. (1988). Geodinamica del Tirreno e dell'Appennino centro-meridionale: la nuova carta della Moho. *Mem. Soc. Geol. It*, *41*, 121–140.

Lucente, F. P., Chiarabba, C., Cimini, G. B., & Giardini, D. (1999). Tomographic constraints on the geodynamic evolution of the Italian region. *Journal of Geophysical Research*, *104*(9), 20307–20327. https://doi.org/10.1029/1999JB900147

Ludwig, W. J., Nafe, J. E., & Drake, C. L. (1970). Seismic refraction. In A. E. Maxwell (Ed.), *New Concepts of Sea Floor Evolution* (pp. 563–584). New York.

Lustrino, M., Duggen, S., & Rosenberg, C. L. (2011). The Central-Western Mediterranean: Anomalous igneous activity in an anomalous collisional tectonic setting. *Earth-Science Reviews*, *104*(1–3), 1–40. https://doi.org/10.1016/j.earscirev.2010.08.002

Lynner, C., & Porritt, R. W. (2017). Crustal structure across the eastern North American margin from ambient noise tomography. *Geophysical Research Letters*, *44*(13), 6651–6657. https://doi.org/10.1002/2017GL073500

Malinverno, A., & Ryan, W. B. F. (1986). Extension in the Tyrrhenian Sea and shortening in the Apennines as result of arc migration driven by sinking of the lithosphere. *Tectonics*, *5*(2), 227–245. https://doi.org/10.1029/TC005i002p00227

Manu-Marfo, D., Aoudia, A., Pachhai, S., & Kherchouche, R. (2019). 3D shear wave velocity model of the crust and uppermost mantle beneath the Tyrrhenian basin and margins. *Scientific Reports*, *9*(1), 3609. https://doi.org/10.1038/s41598-019-40510-z

Marani, M. P., & Trua, T. (2002). Thermal constriction and slab tearing at the origin of a superinflated spreading ridge: Marsili volcano (Tyrrhenian Sea). *Journal of Geophysical Research: Solid Earth*, *107*(B9), EPM 3-1-EPM 3-15. https://doi.org/10.1029/2001JB000285

Marone, F., van der Lee, S., & Giardini, D. (2004). Three-dimensional upper-mantle S - velocity model for the Eurasia-Africa plate boundary region. *Geophysical Journal International*, *158*(1), 109–130. https://doi.org/10.1111/j.1365-246X.2004.02305.x

McGarr, A. (1988). On the State of Lithospheric Stress in the Absence of Applied Tectonic Forces. *Journal of Geophysical Research: Solid Earth*, *93*(B11), 13609–13617. https://doi.org/10.1029/JB093iB11p13609

McKenzie, D. P. (1970). Plate Tectonics of the Mediterranean Region. *Nature*, *226*(5242), 239–243. https://doi.org/10.1038/226239a0

Mele, G., Rovelli, A., Seber, D., Hearn, T. M., & Barazangi, M. (1998). Compressional velocity structure and anisotropy in the uppermost mantle beneath Italy and surrounding regions. *Journal of Geophysical Research*, *103*(B6), 12529. https://doi.org/10.1029/98JB00596

Milia, A., Torrente, M. M., & Tesauro, M. (2017). From stretching to mantle exhumation in a triangular backarc basin (Vavilov basin, Tyrrhenian Sea, Western Mediterranean). *Tectonophysics*, *710–711*, 108–126. https://doi.org/10.1016/j.tecto.2016.10.017

Moeller, S., Grevemeyer, I., Ranero, C. R., Berndt, C., Klaeschen, D., Sallares, V., … de Franco, R. (2014). Crustal thinning in the northern Tyrrhenian Rift: Insights from multichannel and wide-angle seismic data across the basin. *Journal of Geophysical Research: Solid Earth*, *119*(3), 1655–1677. https://doi.org/10.1002/2013JB010431

Moeller, S., Grevemeyer, I., Ranero, C. R., Berndt, C., Klaeschen, D., Sallares, V., … De Franco, R. (2013). Early-stage rifting of the northern Tyrrhenian Sea Basin: Results from a combined wide-angle and multichannel seismic study. *Geochemistry, Geophysics, Geosystems*, *14*(8), 3032–3052. https://doi.org/10.1002/ggge.20180

Mooney, W. D., & Kaban, M. K. (2010). The North American upper mantle: Density, composition, and evolution. *Journal of Geophysical Research*, *115*(B12), B12424. https://doi.org/10.1029/2010JB000866

Neri, G., Orecchio, B., Totaro, C., Falcone, G., & Presti, D. (2009). Subduction Beneath Southern Italy Close the Ending: Results from Seismic Tomography. *Seismological Research Letters*, *80*(1), 63–70. https://doi.org/10.1785/gssrl.80.1.63

Nicolosi, I., Speranza, F., & Chiappini, M. (2006). Ultrafast oceanic spreading of the Marsili Basin, southern Tyrrhenian Sea: Evidence from magnetic anomaly analysis. *Geology*, *34*(9), 717–720. https://doi.org/10.1130/G22555.1

Nijholt, N., Govers, R., & Wortel, R. (2018). On the forces that drive and resist deformation of the south-central Mediterranean: a mechanical model study. *Geophysical Journal International*, (May), 876–894. https://doi.org/10.1093/gji/ggy144

Nocquet, J.-M. (2012). Present-day kinematics of the Mediterranean: A comprehensive overview of GPS results. *Tectonophysics*, *579*, 220–242. https://doi.org/10.1016/j.tecto.2012.03.037

Pachhai, S., Dettmer, J., & Tkalčić, H. (2015). Ultra-low velocity zones beneath the Philippine and Tasman Seas revealed by a trans-dimensional Bayesian waveform inversion. *Geophysical Journal International*, *203*(2), 1302–1318. https://doi.org/10.1093/gji/ggv368

Pachhai, S., Tkalčić, H., & Dettmer, J. (2014). Bayesian inference for ultralow velocity zones in the Earth's lowermost mantle: Complex ULVZ beneath the east of the Philippines. *Journal of Geophysical Research: Solid Earth*, *119*(11), 8346–8365. https://doi.org/10.1002/2014JB011067

Palano, M., Schiavone, D., Loddo, M., Neri, M., Presti, D., Quarto, R., … Neri, G. (2015). Active upper crust deformation pattern along the southern edge of the Tyrrhenian subduction zone (NE Sicily): Insights from a multidisciplinary approach. *Tectonophysics*, *657*, 205–218. https://doi.org/10.1016/j.tecto.2015.07.005

Panza, G. F., Peccerillo, A., Aoudia, A., & Farina, B. (2007). Geophysical and petrological modelling of the structure and composition of the crust and upper mantle in complex geodynamic settings: The Tyrrhenian Sea and surroundings. *Earth-Science Reviews*,

80(1–2), 1–46. https://doi.org/10.1016/j.earscirev.2006.08.004

Panza, G. F., Pontevivo, A., Sarao', A., Aoudia, A., & Peccerillo, A. (2004). Structure of the lithosphere-asthenosphere and volcanism in the Tyrrhenian Sea and surroundings. *Memorie Descrittive Carta Geologica d'Italia*, *XLIV*, 29–55.

Peccerillo, A. (2017a). *Cenozoic volcanism in the Tyrrhenian Sea region*. Springer.

Peccerillo, A. (2017b). Southern Tyrrhenian Sea. In *Cenozoic Volcanism in the Tyrrhenian Sea Region* (pp. 339–362). https://doi.org/10.1007/978-3-319-42491-0_12

Piana Agostinetti, N., & Amato, A. (2009). Moho depth and V p / V s ratio in peninsular Italy from teleseismic receiver functions. *Journal of Geophysical Research*, *114*(B6), B06303. https://doi.org/10.1029/2008JB005899

Piromallo, C., & Morelli, A. (2003). P wave tomography of the mantle under the Alpine-Mediterranean area. *Journal of Geophysical Research: Solid Earth*, *108*(B2), 1–23. https://doi.org/10.1029/2002JB001757

Polonia, A., Torelli, L., Artoni, A., Carlini, M., Faccenna, C., Ferranti, L., … Wortel, R. (2016). The Ionian and Alfeo-Etna fault zones: New segments of an evolving plate boundary in the central Mediterranean Sea? *Tectonophysics*, *675*, 69–90. https://doi.org/10.1016/j.tecto.2016.03.016

Pondrelli, S. (2004). Convergence vs. retreat in Southern Tyrrhenian Sea: Insights from kinematics. *Geophysical Research Letters*, *31*(6), L06611. https://doi.org/10.1029/2003GL019223

Prada, M., Ranero, C. R., Sallares, V., Zitellini, N., & Grevemeyer, I. (2016). Mantle exhumation and sequence of magmatic events in the Magnaghi-Vavilov Basin (Central Tyrrhenian, Italy): New constraints from geological and geophysical observations. *Tectonophysics*, *689*(January), 133–142. https://doi.org/10.1016/j.tecto.2016.01.041

Prada, M., Sallares, V., Ranero, C. R., Vendrell, M. G., Grevemeyer, I., Zitellini, N., & de Franco, R. (2015). The complex 3-D transition from continental crust to backarc magmatism and exhumed mantle in the Central Tyrrhenian basin. *Geophysical Journal International*, *203*(1), 63–78. https://doi.org/10.1093/gji/ggv271

Prada, M., Sallares, V., Ranero, C. R., Vendrell, M. G., Grevemeyer, I., Zitellini, N., & De Franco, R. (2014). Seismic structure of the Central Tyrrhenian basin: Geophysical constraints on the nature of the main crustal domains. *Journal of Geophysical Research: Solid Earth*, *119*(1), 52–70. https://doi.org/10.1002/2013JB010527

Rehault, J. P., Boillot, G., & Mauffret, A. (1985). The western Mediterranean basin. *Geological Evolution of the Mediterranean Basin*, 101–129.

Rota, F. A., & Fichera, R. (1987). Magnetic interpretation related to geo-magnetic provinces: the Italian case history. *Tectonophysics*, *138*(2–4). https://doi.org/10.1016/0040-1951(87)90038-2

Sartori, R. (2003). The Tyrrhenian back-arc basin and subduction of the Ionian lithosphere. *Episodes*, *26*(3), 217–221.

Sartori, R., Torelli, L., Zitellini, N., Carrara, G., Magaldi, M., & Mussoni, P. (2004). Crustal features along a W-E Tyrrhenian transect from Sardinia to Campania margins (Central Mediterranean). *Tectonophysics*, *383*(3–4), 171–192. https://doi.org/10.1016/j.tecto.2004.02.008

Savelli, C. (2002). Time–space distribution of magmatic activity in the western Mediterranean and peripheral orogens during the past 30 Ma (a stimulus to geodynamic considerations). *Journal of Geodynamics*, *34*(1), 99–126. https://doi.org/10.1016/S0264-3707(02)00026-1

Savelli, C. (2015). Fast Episodes of West-Mediterranean-Tyrrhenian Oceanic Opening and Revisited Relations with Tectonic Setting. *Scientific Reports*, *5*(1), 14271. https://doi.org/10.1038/srep14271

Scarfì, L., Barberi, G., Barreca, G., Cannavò, F., Koulakov, I., & Patanè, D. (2018). Slab narrowing in the Central Mediterranean: the Calabro-Ionian subduction zone as imaged by high resolution seismic tomography. *Scientific Reports*, *8*(1), 5178. https://doi.org/10.1038/s41598-018-23543-8

Schettino, A., & Turco, E. (2011). Tectonic history of the western Tethys since the Late Triassic. *Geological Society of America Bulletin*, *123*(1–2), 89–105. https://doi.org/10.1130/B30064.1

Schutt, D. L., & Lesher, C. E. (2010). Compositional trends among Kaapvaal Craton garnet peridotite xenoliths and their effects on seismic velocity and density. *Earth and Planetary Science Letters*, *300*(3–4), 367–373. https://doi.org/10.1016/j.epsl.2010.10.018

Selvaggi, G., & Chiarabba, C. (1995). Seismicity and P-wave velocity image of the Southern Tyrrhenian subduction zone. *Geophysical Journal International*, *121*(3), 818–826. https://doi.org/10.1111/j.1365-246X.1995.tb06441.x

Serpelloni, E., Anzidei, M., Baldi, P., Casula, G., & Galvani, A. (2005). Crustal velocity and strain-rate fields in Italy and surrounding regions: new results from the analysis of permanent and non-permanent GPS networks. *Geophysical Journal International*, *161*(3), 861–880. https://doi.org/10.1111/j.1365-246X.2005.02618.x

Shapiro, N. M., & Campillo, M. (2004). Emergence of broadband Rayleigh waves from correlations of the ambient seismic noise. *Geophysical Research Letters*, *31*(April), 8–11. https://doi.org/10.1029/2004GL019491

Shapiro, N. M., Campillo, M., Stehly, L., & Ritzwoller, M. H. (2005). High-Resolution Surface-Wave Tomography from Ambient Seismic Noise. *Science*, *307*(5715), 1615–1618. https://doi.org/10.1126/science.1108339

Sheehan, A. F., & Solomon, S. C. (1991). Joint inversion of shear wave travel time residuals and geoid and depth anomalies for long-wavelength variations in upper mantle temperature and composition along the Mid-Atlantic Ridge. *Journal of Geophysical Research: Solid Earth*, *96*(B12), 19981–20009. https://doi.org/10.1029/91JB01988

Shen, Y., & Forsyth, D. W. (1995). Geochemical constraints on initial and final depths of melting beneath mid-ocean ridges. *Journal of Geophysical Research: Solid Earth*, *100*(B2), 2211–2237. https://doi.org/10.1029/94JB02768

Spada, M., Bianchi, I., Kissling, E., Agostinetti, N. P., & Wiemer, S. (2013). Combining controlled-source seismology and receiver function information to derive 3-D moho topography for italy. *Geophysical Journal International*, *194*(2), 1050–1068. https://doi.org/10.1093/gji/ggt148

Spadini, G., & Wezel, F. -C. (1994). Structural evolution of the '41st parallel zone'': Tyrrhenian Sea.' *Terra Nova*, *6*(6), 552–562. https://doi.org/10.1111/j.1365-3121.1994.tb00522.x

Speranza, F., Minelli, L., Pignatelli, A., & Chiappini, M. (2012). The Ionian Sea: The oldest in situ ocean fragment of the world? *Journal of Geophysical Research: Solid Earth*, *117*(B12), n/a-n/a. https://doi.org/10.1029/2012JB009475

Stehly, L., Fry, B., Campillo, M., Shapiro, N. M., Guilbert, J., Boschi, L., & Giardini, D. (2009). Tomography of the Alpine region from observations of seismic ambient noise. *Geophysical Journal International*, *178*(1), 338–350. https://doi.org/10.1111/j.1365-246X.2009.04132.x

Stipčević, J., Tkalčić, H., Herak, M., Markušić, S., & Herak, D. (2011). Crustal and uppermost mantle structure beneath the External Dinarides, Croatia, determined from teleseismic receiver functions. *Geophysical Journal International*, *185*(3), 1103–1119. https://doi.org/10.1111/j.1365-246X.2011.05004.x

Trua, T., Marani, M. P., & Gamberi, F. (2018). Magma Plumbing System at a Young Back-Arc Spreading Center: The Marsili Volcano, Southern Tyrrhenian Sea. *Geochemistry, Geophysics, Geosystems*, *19*(1), 43–59. https://doi.org/10.1002/2017GC007151

Ventura, G., Milano, G., Passaro, S., & Sprovieri, M. (2013). The Marsili Ridge (Southern Tyrrhenian Sea, Italy): An island-arc volcanic complex emplaced on a 'relict' back-arc basin. *Earth-Science Reviews*, *116*(1), 85–94. https://doi.org/10.1016/j.earscirev.2012.11.005

Verbeke, J., Boschi, L., Stehly, L., Kissling, E., & Michelini, A. (2012). High-resolution Rayleigh-wave velocity maps of central Europe from a dense ambient-noise data set. *Geophysical Journal International*, *188*(3), 1173–1187. https://doi.org/10.1111/j.1365-246X.2011.05308.x

Vollmer, R. (1976). Rb-Sr and U-Th-Pb systematics of alkaline rocks: the alkaline rocks from Italy. *Geochimica et Cosmochimica Acta*, *40*(3), 283–295. https://doi.org/10.1016/0016-7037(76)90205-2

Watts, A. B. (2001). *Isostasy and Flexure of the Lithosphere*. Cambridge University Press.

Wiens, D. A., Kelley, K. A., & Plank, T. (2006). Mantle temperature variations beneath back-arc spreading centers inferred from seismology, petrology, and bathymetry. *Earth and Planetary Science Letters*, *248*(1–2), 30–42. https://doi.org/10.1016/j.epsl.2006.04.011

Wortel, M. J. R., & Spakman, W. (2000). Subduction and Slab Detachment in the Mediterranean-Carpathian Region. *Science*, *290*(5498), 1910–1917. https://doi.org/10.1126/science.290.5498.1910

Yang, Y., Li, A., & Ritzwoller, M. H. (2008). Crustal and uppermost mantle structure in

southern Africa revealed from ambient noise and teleseismic tomography. *Geophysical Journal International*, *174*(1), 235–248. https://doi.org/10.1111/j.1365-246X.2008.03779.x

Yang, Y., & Ritzwoller, M. H. (2008). Characteristics of ambient seismic noise as a source for surface wave tomography. *Geochemistry, Geophysics, Geosystems*, *9*(2). https://doi.org/10.1029/2007GC001814

Yang, Y., Ritzwoller, M. H., Levshin, A. L., & Shapiro, N. M. (2007). Ambient noise Rayleigh wave tomography across Europe. *Geophysical Journal International*, *168*(1), 259–274. https://doi.org/10.1111/j.1365-246X.2006.03203.x

Yanovskaya, T. B. (1997). Resolution estimation in the problems of seismic ray tomography. *Izvestiya Physics of the Solid Earth*, *33*(9), 762–765.

Yanovskaya, T. B., & Ditmar, P. G. (1990). Smoothness criteria in surface wave tomography. *Geophysical Journal International*, *102*(1), 63–72. https://doi.org/10.1111/j.1365-246X.1990.tb00530.x

Yanovskaya, T. B., Kizima, E. S., & Antonova, L. M. (1998). Structure of the crust in the Black Sea and adjoining regions from surface wave data. *Journal of Seismology*, *2*(4), 303–316. https://doi.org/10.1023/A:1009716017960

Zito, G., Mongelli, F., de Lorenzo, S., & Doglioni, C. (2003). Heat flow and geodynamics in the Tyrrhenian Sea. *Terra Nova*, *15*(6), 425–432. https://doi.org/10.1046/j.1365-3121.2003.00507.x

Zulfakriza, Z., Saygin, E., Cummins, P. R., Widiyantoro, S., Nugraha, A. D., Lühr, B. G., & Bodin, T. (2014). Upper crustal structure of central Java, Indonesia, from transdimensional seismic ambient noise tomography. *Geophysical Journal International*, *197*(1), 630–635. https://doi.org/10.1093/gji/ggu016

Acknowledgements

This PhD was supported by the ICTP-Generali research programme. First of all, I would like to thank my supervisor Prof. Abdelkrim Aoudia for being a tremendous mentor for me. I appreciate your guidance, kind support, and many useful and inspiring discussions we have had. I wish to acknowledge Dr Surya Pachhai and Dr Farhan Javed for scientific discussions and the advice that they gave me. I also want to thank Radia Kherchouche for her valuable help when I first started my research at ICTP. My time at ICTP has been fruitful thanks to the support of the ICTP staff with their help whenever I struggle with Italian bureaucracy. I would like to thank my friends in the ESP solid earth geophysics group at ICTP: Blaz Vicic, Donna Bou-Rabee, Amir Sadeghi Bagherabadi, Momeni Seyyedmaalek and Thapa Hari Ram. I wish

to also thank my friend Adu Offei-Danso for his support and company. Finally, I am grateful to my lovely parents who always support me from far away with their prayers and encouragements.